Synthesizing Nonlinear Transient Gravity Waves in Random Seas

Dipl.-Ing. Ulrich Steinhagen

Approved by the
Faculty of Transport and Mechanical Systems
(Fakultät für Verkehrs- und Maschinensysteme)
in partial fulfillment of the requirements for the degree of
Doktor der Ingenieurwissenschaften (Dr.-Ing.)

Doctoral Committee:
Prof. Dr. rer. nat. Andreas Dillmann (Chairman)
Prof. Dr.-Ing. Günther F. Clauss (Thesis Supervisor)
Prof. Dr.-Ing. Frank Thiele (Thesis Supervisor)

May 11, 2001

Technische Universität Berlin
D 83

To Simone Archut

Preface

I would like to express my sincere gratitude to Prof. Dr.-Ing. Günther Clauss for his encouragement, guidance and inspiration throughout the duration of this research. I am also greatly indebted to Prof. Dr.-Ing. Frank Thiele, Dr.-Ing. Linchun Huang and Dr.-Ing. Torsten Schlurmann whose suggestion and criticism have been very beneficial in the preparation of this dissertation. Many thanks to Prof. Dr. rer. nat. Andreas Dillmann who chaired the doctoral committee.

I owe deep gratitude to my parents Ingeborg and Manfred Steinhagen as well as Simone Archut who helped me during the course of this study. Without their love and patient support, I could never have come this far.

I am also grateful to the faculty, staff and colleagues of the Institute of Landborne and Marine Transportation at Berlin University of Technology for their helpful discussion and willing assistance.

Zusammenfassung (Summary)

Die Ozeane bedecken mehr als zwei Drittel der Erdoberfläche und bestimmen maßgeblich die Umweltbedingungen für den Entwurf, die Installation und den Betrieb maritimer Systeme. Die Strukturbelastungen werden allgemein vom Seegang dominiert, wobei auch den Wirkungen von Wind, Strömung, Eis und Erdbeben in Abhängigkeit des Einsatzgebietes eine große Bedeutung zukommen kann. Die genaue Kenntnis der Hydrodynamik von Schwerewellen sowie deren komplexe Wechselwirkung mit maritimen Systemen stellt eine wesentliche Voraussetzung für den sicheren und wirtschaftlichen Betrieb dar. Zunehmend interessieren Extremsituationen, bei denen sich außergewöhnlich hohe Wellen im stochastischen Wellenfeld entwickeln.

In der vorliegenden Dissertation wird ein neues Verfahren zur computergestützten Synthese nichtlinearer transienter Schwerewellen im stochastischen Seegang vorgestellt. Das Ziel der Arbeit besteht darin, ein vielseitig einsetzbares Analyse- und Entwicklungswerkzeug bereitzustellen, um detaillierte experimentelle und numerische Untersuchungen von extremen Wellenereignissen zu ermöglichen. Ausgehend von der potentialtheoretischen Beschreibung des zweidimensionalen nichtlinearen Strömungsproblems werden hohe deterministische Einzelwellen und Wellengruppen gezielt im stochastischen Wellenfeld synthetisiert. Hierzu werden in einem zweistufigen Prozeß moderne Optimierungsalgorithmen der Nichtlinearen Programmierung angewendet.

Zur Bestimmung einer ersten Näherungslösung werden bei der potentialtheoretischen Beschreibung der Strömung die Oberflächenrandbedingungen linearisiert. Dies erlaubt die analytische Darstellung des Wellenzugs durch Superposition unabhängiger, harmonischer Elementarwellen. Insbesondere kann die Berechnung der zeitlichen und räumlichen Ausbreitung durch Verwendung der schnellen Fourier-Transformation effizient im Frequenzbereich erfolgen. Für ein vorgegebenes Fourier-Spektrum werden die gewünschten Eigenschaften des linearen Wellenzugs durch Anwendung der Sequentiellen Quadratischen Programmierung erzeugt, die ein zufälliges Phasenspektrum entsprechend modifiziert.

Zur Simulation der nichtlinearen Wellenausbreitung im numerischen Wellenkanal wird ein Rechenprogramm entwickelt, dem die gemischte Euler-Lagrange-Formulierung des Anfangs-Randwertproblems zugrunde liegt. Zur Lösung der Laplace-Gleichung für Neumann- und Dirichlet-Randbedingungen wird die Methode der finiten Elemente eingesetzt. Die Integration in der Zeit erfolgt mit der klassischen Runge-Kutta-Methode vierter Ordnung. Störende Reflexionen am Kanalende werden durch ein effizientes numerisches Absorptionsverfahren vermieden. Die Berechnungsergebnisse werden systematisch verifiziert und anhand von experimentellen Meßdaten validiert.

Eine deutliche qualitative Verbesserung der ersten Näherungslösung wird durch die Anwendung eines modifizierten Simplex-Algorithmus unter Berücksichtigung der nichtlinearen Wellenausbreitung im numerischen Wellenkanal erreicht. Hierbei wird gezielt der Ausschnitt der Wellenblattbewegung verändert, der für die Entwicklung der zu synthetisierenden Extremwellen im stochastischen Wellenfeld verantwortlich ist. Zur Reduzierung des hohen Rechenaufwandes wird die diskrete Wavelet-Transformierte der Wellenblattbewegung bestimmt, die die Selektion einer geringen Anzahl von freien Variablen ermöglicht.

Das neu entwickelte Verfahren zur Synthese nichtlinearer transienter Schwerewellen im stochastischen Seegang wird exemplarisch anhand einer Einzelwelle sowie einer Wellengruppe dargestellt. In beiden Fällen belegen die Ergebnisse die exzellente Übereinstimmung der generierten Wellenzüge mit den Zielvorgaben und damit die Wirksamkeit des Verfahrens.

Abstract

The oceans cover more than two thirds of the earth's surface and present a unique set of environmental conditions which govern the design, installation, and operation of marine systems. In general, structural loads are dominated by the wave field. Depending on the operating site, the effects of wind, currents, earthquakes or ice may be of great importance as well. The profound knowledge of the hydrodynamics of gravity waves and their complex interaction with marine systems is a necessary prerequisite for safe and efficient system operation. Attention is increasingly being paid to extreme environmental conditions with unexpected large waves developing in the random wave field.

In this dissertation, a new procedure is presented for computer-aided synthesizing of nonlinear transient gravity waves in random seas. The aim of the study is to provide a multi-purpose analysis and development tool for performing detailed experimental and numerical investigations of extreme wave events. Large deterministic single waves and wave groups are synthesized into random seas with the two-dimensional nonlinear free surface flow problem described by potential theory. This is achieved by a two-stage procedure applying modern optimization algorithms used in nonlinear programming.

To obtain a first approximation of the solution, the free surface boundary conditions of the potential flow problem are linearized. This allows a description of the wave train as the superposition of independent harmonic component waves. In particular, the temporal and spatial evolution can be calculated efficiently in the frequency domain by introducing the fast Fourier transformation. For a given Fourier spectrum, the desired characteristics of the linear wave train are generated by applying sequential quadratic programming which modifies an initially random phase spectrum.

A computer program is developed to simulate the nonlinear wave evolution in the numerical wave tank. The simulation procedure is based on the mixed Eulerian-Lagrangian formulation of the nonlinear initial boundary value problem. The Laplace equation is solved for Neumann and Dirichlet

boundary conditions by the finite element method. The solution is developed in time domain with the classical fourth-order Runge-Kutta formula. Reflections at the end of the wave tank are avoided by an efficient absorption technique. Numerical results are verified systematically and validated by laboratory data.

A significant improvement of the first approximation is achieved by applying a modified simplex method considering the nonlinear wave evolution in the numerical wave tank. A particular part of the wave board motion, which is responsible for the evolution of the extreme waves to be synthesized in the stochastic wave field, is changed. To decrease the high computer costs, the discrete wavelet transform of the wave board motion is determined, enabling the selection of only a few free variables of the associated fitting problem.

The new procedure for synthesizing nonlinear transient waves in random seas is presented exemplarily for a single wave and a wave group. In both cases, the results confirm the excellent agreement of the generated wave trains with the target parameters proving the effectiveness of the procedure.

Contents

List of Figures

List of Tables

Chapter 1

Introduction

1.1 Background

The oceans cover more than two thirds of the earth's surface and present a unique set of environmental conditions which dominates the design, installation, and operation of marine structures.

An offshore system is subjected to several loads due to waves, wind, currents, earthquakes or ice. Wave-induced forces are most important for most offshore environments currently being exploited and may constitute the primary cause of downtime and reduced operating efficiency. In certain continental shelf areas, seismic excitation and/or ice loading could be critical, but hydrodynamic loading continues to be important for fatigue life assessment in both the structure and the soil. Hence, it is necessary to obtain reliable information on the wave environment at the site of interest. A vital consideration is the day-to-day condition of the sea state which governs the installation and operation phase. Particularly important is the determination of extreme wave conditions which establish the characteristcs of individual design waves or design sea states. Underestimation of sea severity may lead to the failure of the structure, whereas overestimation results in unnecessary costs.

One of the main difficulties in selecting design wave conditions is the short-term, as well as long-term, variability of the sea state. Waves may be generated from different directions for any given storm and are affected by refraction, diffraction, reflection and shoaling in shallow water. The selection process is therefore very complicated and site specific. Ideally, decisions should be based on long-term data acquisition at the location of interest, preferably over a period of 15 to 20 years. However, these data are usually not available, and theoretical probability methods must be applied to derive appropriate design wave conditions.

Ships need to withstand loads and motions in extreme wave environments, since weather routing does not safeguard them from encountering such conditions. Leaving aside human errors in the navigation and operation of ships, three basic hazards arise from rough weather: breaking-through due to inadequate hull strength, flooding and foundering through poor watertight integrity, and capsizing due to insufficient roll stability. A survival design approach suggested by Faulkner and Buckley (1997) strongly depends on reliable predictions of environmental loads in case of extreme events.

Fig. 1.1 shows a long-crested and very steep wave just before breaking in the Bay of Biscay, France (Nickerson, 1993). Another huge wave is shown in Fig. 1.2, which is a remarkable photo taken by the captain of the British Wye during a winter storm in the Western Atlantic Ocean south of Newfoundland (Nickerson, 1993). Such waves impose severe impact loads on marine structures and may cause ships to capsize if encountered in a following sea.

The physical and numerical modeling of nonlinear transient waves in random seas play a vital role in determining extreme environmental loads and associated structure responses. The development of sophisticated methods for generating nonlinear target wave regimes with predetermined characteristics is a significant contribution to the analysis of many complex and highly nonlinear engineering problems, such as TLP-ringing and springing, slamming impacts, green water, and dynamic stability of ships.

1.2 Literature Review

Davis and Zarnick (1964) originally proposed transient waves for model tests. The dispersion relationship is used to focus component waves at a nominated location resulting in a high crest elevation. This technique was further developed by Takezawa and Takekawa (1976), as well as by Takezawa and Hirayama (1976), to investigate ship motions in transient water waves. Linear Gaussian wave packets, which can be predicted analytically, were introduced by Clauss and Bergmann (1986) and further verified by Chakrabarti and Libby (1988). The restriction to a Gaussian distribution of wave amplitudes has been abandoned by introducing the fast Fourier transformation technique which allows to select arbitrarily the shape of the wave spectrum (Clauss and Kühnlein, 1995). This linear description enables the prediction of the wave train at any instant and location in the wave tank and has proved to be an efficient technique for many marine applications. Clauss and Kühnlein (1997) present an empirical technique for generating converging nonlinear transient wave packets. Seakeeping model tests based on tailor-made transient wave packets are described by Kühnlein (1997).

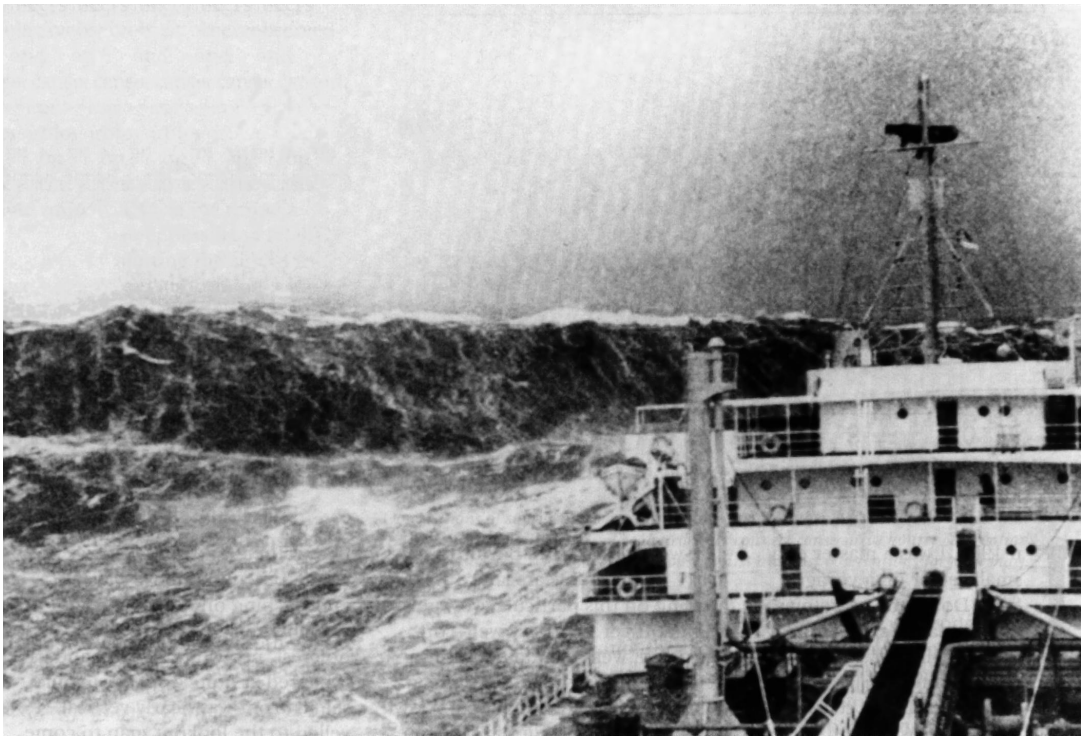

Figure 1.1: Huge wave observed in the Bay of Biscay (Nickerson, 1993).

Extreme transient waves are rare but possible events in the stochastic wave environment, which needs to be considered for realistic simulations. The generation of appropriate design waves is highly complicated due to the nonlinearity of the free surface. Stansberg (1990) empirically investigates extreme waves in laboratory-generated irregular wave trains. Wave superposition based on linear wave theory is used to simulate randomly occurring large waves which are picked out for experimental study. An essentially linear, broad-banded wave theory for predicting the kinematics of large ocean waves in uni-directional seas is presented by Tromans et al. (1991). The so-called *NewWave* design wave is generated by linear superposition of all wave components in a sea state defined by a given wave spectrum in such a way that the most probable maximum crest is obtained. This approach is modified by Taylor (1992) for deep water waves to include second order nonlinear free surface effects such as amplitude modulation and horizontal transport of the short waves by the long waves. Baldock and Swan (1994) present a description of a two-dimensional irregular sea state in which a large transient wave is generated by focusing component waves. The numerical method is based upon a Fourier series expansion in space and time, which is validated by laboratory data. Taylor et al. (1995) describe a theory to constrain a

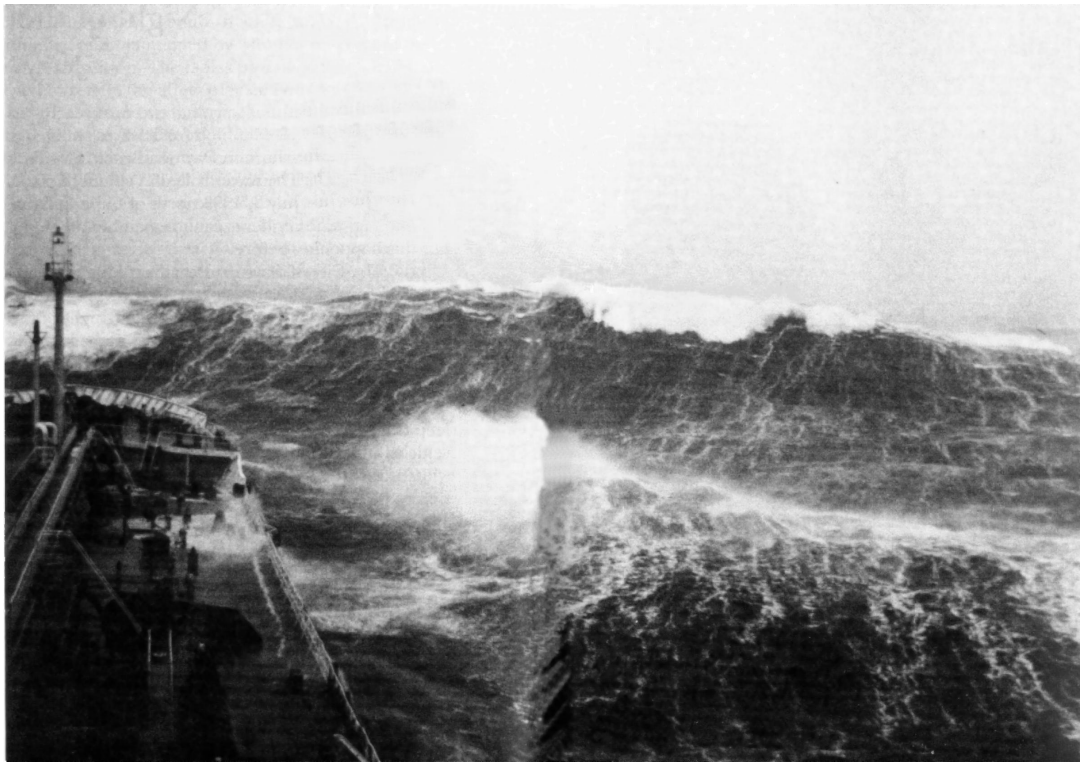

Figure 1.2: Huge wave observed in the Western Atlantic Ocean south of Newfoundland (Nickerson, 1993).

random time series for generating a large crest elevation of a given size at a prescribed time. The technique is a linear process where the extreme surface elevation is indistinguishable from a purely random occurrence of that particular crest. Hua and Ekman (1999) present a numerical procedure based on a boundary element method to simulate irregular steep waves. The wave height and particle velocities at the wave crest are investigated for three severe wave conditions and compared with linear and second order wave theories. They conclude that second order wave theory is not appropriate for predicting extreme wave crests as well as the horizontal particle velocity around these crests. Laboratory experiments were conducted by Kriebel and Alsina (2000) to embed a large transient wave within a random sea. The generation procedure assumes that the free surface can be represented as a Fourier series where all components of the transient wave are in phase. The energy distribution of extreme wave and random sea is controlled by splitting the wave spectrum into two parts. A method for generating a strongly asymmetric wave in an irregular wave train is presented by Zou and Kim (2000). A wave elevation time series with random phase is produced by a

linear procedure. The largest crest elevation among the zero-downcrossing waves is distorted by a method similar to Funke and Mansard (1982), from which the complex amplitude spectrum is obtained. Clauss and Steinhagen (2000) use a sequential quadratic programming method to optimize transient design waves in random seas. For a given design variance spectrum, the desired characteristics of the target wave train regarding wave height and crest structure are generated by optimizing an initially random phase spectrum. The solution is based on linear wave theory and compared to the simulation of the nonlinear wave evolution with the finite element method, which is validated by laboratory data by Clauss and Steinhagen (1999).

Kim et al. (1999) present a comprehensive review of recent progress in numerical wave tank research and development. It focuses on ideal fluids and includes typical formulations, numerical implementations, methods of wave generation, wave damping and absorbing, wave-wave interaction, diffraction, radiation and floating body motion. A comment is given on the simulation of viscous flow based on the Reynolds averaged Navier-Stokes equations (RANSE).

Wolfram et al. (1994) examine the time series of three severe storms recorded at the Total Oil Marine North Alwyn platform in the northern North Sea. The Fourier analysis of these series shows that the wave components do not a have uniformly distributed random phase, which may be attributable to bound waves. Further results from data collected during six of the worst storms recorded at the Alwyn platform are presented by Linfoot et al. (2000). They concentrate on individual wave characteristics such as the joint probability of wave height and period, and the joint probability of wave height and steepness, for which the suitability of various models has been examined. The profiles and characteristics of the three largest waves in each storm are presented and discussed. Haver and Andersen (2000) discuss the possible existence of freak waves. They present some pieces of evidence which seem to support the idea of a separate freak wave population which deviates strongly from a Gaussian process.

Isaacson and Foschi (2000) deal with the selection of design wave conditions. They highlight the difference between the largest expected individual wave height in a sea state with a specified return period and the maximum individual wave height with the same return period, which is found to be considerably larger. They describe, for different situations, the calculation of associated long-term distributions.

1.3 Objectives

The primary objectives of this study are as follows:

i) To develop a procedure to synthesize linear transient waves and wave groups with predetermined characteristics in random seas for given sea state parameters.

ii) To investigate the evolution of linear transient waves and wave groups in random seas.

iii) To develop a computer program to simulate the propagation of two-dimensional nonlinear wave trains in the numerical wave tank.

iv) To verify the computer program and validate numerical results by laboratory data.

v) To find an efficient representation of the wave board motion for identifying relevant signal information.

vi) To develop a procedure to synthesize nonlinear transient waves and wave groups with predetermined characteristics in random seas for given sea state parameters.

vii) To investigate the evolution of nonlinear transient waves and wave groups in random seas.

1.4 Organization

In Chapter 2, the nonlinear initial boundary value problem describing two-dimensional gravity waves propagating in a numerical wave tank is formulated in space-fixed cartesian coordinates. The Airy wave theory is introduced and the analytical solution of the linearized free surface flow problem is derived. The assumption of a linear wave model constitutes the basis for linking the physics of free surface gravity waves with the variance spectrum. The determination of confidence limits on a spectral estimate, as part of the spectral or time series analysis in frequency domain, is described. Common spectral parameters and empirical spectra shapes are presented.

In Chapter 3, the numerical simulation of two-dimensional nonlinear gravity waves is described. The general procedure of the mixed Eulerian-Lagrangian method is introduced and applied to solve the Laplace equation as a nonlinear initial boundary value problem in time domain. The finite

element method is derived and the mesh generation presented. The classical fourth-order Runge-Kutta formula to develop the solution in time domain is illustrated. A local filtering technique is described to suppress numerical instabilities and artificially high frequency oscillations. The performance of the numerical wave absorption scheme is investigated. Numerical results are verified systematically and validated by laboratory data.

In Chapter 4, wavelet analysis is introduced. Based on the multiresolution formulation to decompose signals in low and high frequency components in order to extract information on different resolution scales, the discrete wavelet transform is developed, which enables the implementation of efficient decomposition algorithms. This technique is applied to the time-dependent wave board motion to identify the scales which are most important for the wave generation. The strong compression characteristics of the transform are utilized to reduce considerably the number of free variables in the process of fitting the nonlinear wave train to predetermined target parameters.

In Chapter 5, the general procedure to synthesize linear and nonlinear transient waves and wave groups in random seas is outlined. Firstly, a linear approximation of the desired wave train is computed by optimizing the wavelet representation of the wave board motion for equality and inequality constraints which correspond to the desired wave characteristics. The free variables are the values of an initially random phase spectrum leaving the energy distribution in terms of the variance spectrum unchanged in the optimization. This initial linear guess is further improved by fitting the nonlinear wave evolution simulated in a numerical wave tank to the target characteristics. The free variables are now particular wavelet coefficients which correspond to a certain resolution scale and time range of the wave board motion responsible for the evolution of the target wave sequence. The relevant minimization techniques are the sequential quadratic programming method and the subplex method, which are described in detail.

In Chapter 6, the synthesis of nonlinear transient gravity waves in random seas is illustrated by two examples. The first one addresses a single design wave and the second one a tailored group of three successive waves embedded in a random seaway. Appropriate objective functions and constraints for the two-step generation procedure are derived from global and local target wave characteristics. Results are presented for the linear and nonlinear wave evolution in time, space and frequency domain. The wave height, crest and period structure are investigated by a zero-downcrossing analysis. The various wave board motions and the associated wavelet transforms are compared.

In Chapter 7, the results are summarized and conclusions drawn. Further extensions of this study are suggested.

Chapter 2

Free Surface Gravity Waves

2.1 Introduction

Ocean waves are primarily generated by the interaction of wind and the water surface. Wind energy is transmitted into wave energy through friction between air and water, and local pressure fields associated with the wind blowing over the wave surface. Water waves can also be caused by other phenomena, such as high currents, landslides, explosions and earthquakes. A wave is a traveling disturbance of the sea surface. Its velocity depends on the wave period, or wave length, wave height and water depth, and differs significantly from the velocity of the water particles which move in nearly closed orbital loops with little net forward motion. The wave periods can cover an extremely broad range, such as several months for planetary waves, half a day for tides, several hours for storm surges, dozens of minutes for tsunamis, a few seconds for swell and fractions of a second for capillary waves. The low viscosity of water plays a minor role in many situations of practical interest and is usually neglected.

The wave field of the open ocean is irregular, both in space and time. However, the sea state may maintain a characteristic appearance over a fairly wide area and often for a period of half an hour or more. Hence, for most engineering problems, surface waves are regarded as a random, or stochastic, process under short-term stationary conditions. The long-term or wave climate characteristics of the sea state highlight the variability of the sea state at a particular location over periods ranging from weeks to decades. Variations on these time scales are caused by climate irregularity. The principal elements of the wave climate are wave height and wave period parameters, as well as wave direction. The height parameter is chosen to be the significant wave height, defined as the average of the highest one third of waves. The

period parameter is usually the peak period corresponding to the spectral peak frequency.

Wave theories for modeling free surface waves are generally complicated because kinematic and dynamic free surface boundary conditions are nonlinear. Further difficulty is associated with the application of these conditions, since the location of the free surface is not known in advance but part of the solution sought. Some theories seek rational and nonlinear approximations whose validity may not be universal. The simulation of nonlinear extreme wave regimes requires sophisticated numerical methods based, for example, on the finite element method or boundary element method.

Section 2.2 describes the nonlinear wave theory based on the assumptions of potential flow. The analytical solution of the linearized free surface flow problem is derived in the subsequent Section 2.3. The last section of this chapter, Section 2.4, deals with spectral or time series analysis in the frequency domain. Common spectral parameters and empirical spectra shapes are presented.

2.2 Nonlinear Wave Theory

The numerical wave tank for simulating two-dimensional gravity waves in time domain is illustrated in Fig. 2.1. The analysis of the nonlinear free surface flow problem is based on the well-known potential flow theory (Truckenbrodt, 1992). The entire flow field is described by a scalar function called velocity potential $\phi(x, z, t)$, which satisfies the Laplace equation:

$$\nabla^2 \phi \;=\; 0 \tag{2.1}$$

for Neumann and Dirichlet boundary conditions on a closed solution domain. This elliptic partial differential equation states mass conservation where ∇ is the gradient operator vector. Potential flow theory requires the fluid to be inviscid and incompressible, and the flow to be irrotational:

$$\nu \;=\; 0, \quad \frac{D\rho}{Dt} \;=\; 0, \quad \nabla \times \nabla\phi \;=\; 0 \tag{2.2}$$

where ν is the kinematic viscosity and ρ the mass density. The atmospheric pressure p_a above the free surface $\zeta(x, t)$ is assumed to be constant, and surface tension is neglected.

2.2.1 Boundary Conditions

Mass conservation requires that there be no flow through the boundary Γ of the fluid domain Ω. Neumann boundary conditions are defined by the partial

derivative $\partial\phi/\partial n$ in the normal direction n pointing out of the fluid domain. Dirichlet boundary conditions are given in terms of the velocity potential ϕ. On fixed walls Γ_W at the bottom and the end of the numerical wave tank,

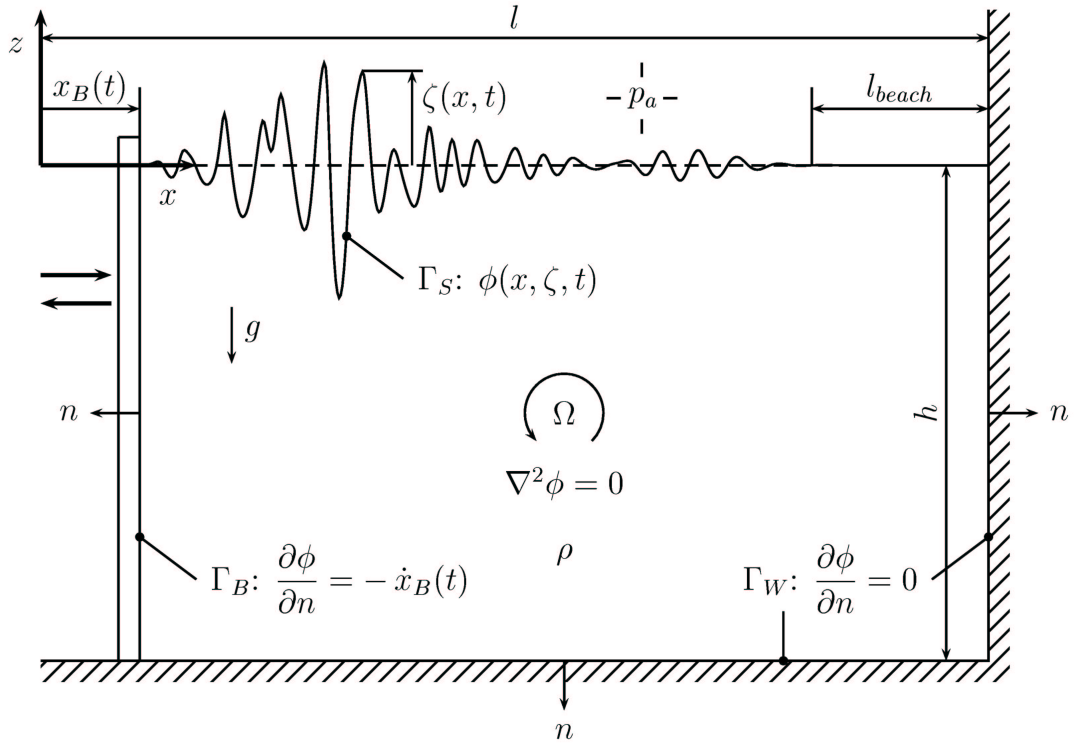

Figure 2.1: Numerical wave tank.

the Neumann boundary conditions are:

$$\begin{aligned} \frac{\partial\phi}{\partial z} &= 0 \qquad \text{at} \quad z = -h \\ \frac{\partial\phi}{\partial x} &= 0 \qquad \text{at} \quad x = l. \end{aligned} \tag{2.3}$$

The horizontal motion of the wave board Γ_B is described by $x_B(t)$ and the associated Neumann boundary condition is given by its normal velocity $\dot{x}_B(t)$:

$$\frac{\partial\phi}{\partial x} = \dot{x}_B(t) \qquad \text{at} \quad x = x_B(t). \tag{2.4}$$

The kinematic and dynamic free surface boundary conditions are both nonlinear. Further difficulty is associated with the application of these boundary conditions, since the location of the free surface is not initially known but is

part of the solution sought. No flow through the free surface Γ_S is forced by the kinematic free surface boundary condition:

$$\frac{\partial \phi}{\partial z} \;=\; \frac{\partial \zeta}{\partial t} + \frac{\partial \phi}{\partial x}\,\frac{\partial \zeta}{\partial x} \;=\; 0 \qquad \text{at} \quad z = \zeta(x,t). \tag{2.5}$$

Momentum is conserved by the Euler equation, which is the starting point for deriving the dynamic free surface boundary condition:

$$\frac{D\boldsymbol{v}}{Dt} \;=\; \frac{\partial \boldsymbol{v}}{\partial t} + \Big(\boldsymbol{v}\,\nabla^T\Big)\boldsymbol{v} \;=\; -\frac{1}{\rho}\nabla p + \boldsymbol{f} \tag{2.6}$$

where $\boldsymbol{f} = (0, -g)$ represents the conservative body force per unit mass and g the gravitational acceleration. With the assumptions of potential flow theory $\boldsymbol{v} = \nabla\phi$ and $\nabla \times \nabla\phi = 0$ the Euler equation can also be written as:

$$\nabla \left(\frac{\partial \phi}{\partial t} \;+\; \frac{1}{2}\,\nabla\phi \cdot \nabla\phi + g\,z + \frac{p}{\rho} \right) \;=\; 0. \tag{2.7}$$

Integrating this with respect to the space variables x and z gives the Bernoulli equation:

$$\frac{\partial \phi}{\partial t} \;+\; \frac{1}{2}\,\nabla\phi \cdot \nabla\phi + g\,z + \frac{p}{\rho} \;=\; B(t). \tag{2.8}$$

Assuming the atmospheric pressure p_a to be constant at the free surface and choosing $B(t) = p_a/\rho$, which is permissible for long wave tanks, defines the dynamic free surface boundary condition as:

$$\frac{\partial \phi}{\partial t} \;+\; \frac{1}{2}\,\nabla\phi \cdot \nabla\phi + g\,\zeta \;=\; 0 \qquad \text{at} \quad z = \zeta(x,t). \tag{2.9}$$

Introducing the substantial derivative of the velocity potential:

$$\frac{D\phi}{Dt} \;=\; \frac{\partial \phi}{\partial t} + \nabla\phi \cdot \nabla\phi \tag{2.10}$$

enables us to establish the Lagrangian form of the free surface boundary conditions:

$$\frac{Dx}{Dt} \;=\; \frac{\partial \phi}{\partial x}, \qquad \frac{Dz}{Dt} \;=\; \frac{\partial \phi}{\partial z}, \tag{2.11}$$

$$\frac{D\phi}{Dt} \;=\; \frac{1}{2}\,\nabla\phi \cdot \nabla\phi - g\,\zeta. \tag{2.12}$$

These conditions need to be modified for long time simulations in order to avoid reflections at the end of the numerical wave tank. In this work, a method described by Cointe et al. (1990) is applied, where damping terms are added to the kinematic and dynamic free surface boundary conditions:

$$\frac{Dx}{Dt} = \frac{\partial \phi}{\partial x} - \mu(x_e)(x - x_e), \tag{2.13}$$

$$\frac{Dz}{Dt} = \frac{\partial \phi}{\partial z} - \mu(x_e)(z - z_e), \tag{2.14}$$

$$\frac{D\phi}{Dt} = \frac{1}{2}\nabla\phi \cdot \nabla\phi - g\,\zeta - \mu(x_e)(\phi - \phi_e). \tag{2.15}$$

The damping coefficient $\mu(x)$ is defined as:

$$\mu(x) = \begin{cases} \omega_{beach}\left(\dfrac{x - (l - l_{beach})}{l_{beach}}\right)^2, & \text{for} \quad l - l_{beach} \leq x \leq l \\ 0, & \text{for} \quad x < l - l_{beach} \end{cases} \tag{2.16}$$

where ω_{beach} controls the strength and l_{beach} the length of the numerical beach. The reference values ϕ_e, x_e and z_e are obtained from the initial particle locations and their associated velocity potential at the beginning of the numerical simulation, i.e. $\phi_e = 0$ and $z_e = 0$. The efficiency of this absorbing technique is presented in Section 3.6.2.

2.2.2 Integral Parameters

The progressive wave field is described by the field variables and a number of useful integral parameters which relate to the conservation laws for mass, momentum and energy. The definitions in Table 2.1 apply for the two-dimensional wave field in the solution domain of the wave tank illustrated in Fig. 2.1. The time-dependent parameters are given in terms of the specific values per unit length of crest. The potential energy is measured with respect to the Still Water Level ($z = 0$) as the horizontal datum.

2.3 Linear Wave Theory

Linear wave theory, or Airy wave theory, plays a central role in offshore and coastal hydrodynamics. The relative simplicity provides immediate access to the wave kinematics throughout the flow field. The mathematical linearity of the theory facilitates its application in solving many ocean engineering

Potential energy	$E_{pot}(t)$	$=$	$\int_0^{\zeta(x,t)} \int_{x_B(t)}^{l} \rho\, g\, z\, dx\, dz$
Kinetic energy	$E_{kin}(t)$	$=$	$\int_{-h}^{\zeta(x,t)} \int_{x_B(t)}^{l} \frac{1}{2}\, \rho\, (\nabla\phi)^2\, dx\, dz$
Energy flux	$\dot{E}(x,t)$	$=$	$\int_{-h}^{\zeta(x,t)} \rho\, \frac{\partial\phi}{\partial x}\, \frac{\partial\phi}{\partial t}\, dz$
Mass flux	$\dot{m}(x,t)$	$=$	$\int_{-h}^{\zeta(x,t)} \rho\, \frac{\partial\phi}{\partial x}\, dz$

Table 2.1: Integral parameters of the two-dimensional wave field.

problems. It enables the superposition of component waves and thus the analysis of diffraction, refraction and real sea states in the frequency domain. It should be stressed that linear wave theory successfully predicts general features of the wave environment but fails to describe some of the details, especially for steeper waves in deep water and for almost all waves in shallow water. These details are significant in many applications and require a nonlinear theory for a more complete prediction.

The mathematical formulation is presented for two-dimensional periodic surface gravity waves with a single period T in water of constant depth h without current. The uniform wave train propagates horizontally in direction x with a constant wave length L and a constant wave height H. The coordinate z is measured vertically upward from the Still Water Level, which is also the reference datum for the surface elevation $\zeta(x,t)$. The formulation is based on the assumptions of potential flow theory. The field equation is the Laplace Eq. (2.1) requiring a closed solution domain with boundary conditions all round the boundary.

2.3.1 Boundary Conditions

The bottom boundary condition requires that there be no flow through the horizontal bed, which is expressed in terms of $\phi(x,z,t)$:

$$\frac{D\phi}{Dz} = 0 \qquad \text{at} \quad z = -h. \tag{2.17}$$

The quadratic, and hence nonlinear, terms in the kinematic and dynamic free surface boundary conditions, namely $\partial\phi/\partial x \cdot \partial\zeta/\partial x$ in Eq. (2.5) and $1/2\ \nabla\phi \cdot$

$\nabla\phi$ in Eq. (2.9), are removed to achieve linearized boundary conditions. Since nonlinearity is also associated with the application of these boundary conditions at the initially unknown free surface $\zeta(x,t)$, further simplification is achieved by applying these conditions at Still Water Level:

$$\frac{\partial\phi}{\partial z} \;=\; \frac{\partial\zeta}{\partial t}, \qquad \frac{\partial\phi}{\partial t} + g\,\zeta \;=\; 0 \qquad \text{at} \quad z = 0. \tag{2.18}$$

The formulation of the linearized gravity wave problem is completed by defining periodic lateral boundary conditions which are conveniently located at adjacent crests or troughs:

$$\phi(x,z,t) \;=\; \phi(x+L,z,t) \;=\; \phi(x,z,t+T). \tag{2.19}$$

2.3.2 Linear Solution

An analytical solution to the linearized gravity wave problem without current is first presented by G.B. Airy in 1845 (reissued as Airy, 1849). The solution is determined through the classical method of separating variables and can easily be confirmed by direct back-substitution into the field equation and the boundary conditions:

$$\phi(x,z,t) \;=\; \frac{\zeta_a\, g}{\omega}\,\frac{\cosh k(h+z)}{\cosh kh}\,\sin(kx-\omega t) \tag{2.20}$$

where the wave amplitude is half the wave height $\zeta_a = H/2$. The wave number $k = 2\pi/L$ and the wave frequency $\omega = 2\pi/T$ are related by:

$$\omega^2 \;=\; gk\,\tanh kh \tag{2.21}$$

which is called the *dispersion relationship*. The phase speed or wave celerity C of a progressive wave depends particularly on k and h or ω and h:

$$C \;=\; \frac{L}{T} \;=\; \frac{\omega}{k} \;=\; \frac{g}{\omega}\,\tanh kh \;=\; \left(\frac{g}{k}\,\tanh kh\right)^{1/2}. \tag{2.22}$$

All field variables can easily be derived from the linear solution together with the kinematic and dynamic free surface boundary conditions. The most important are summarized in Table 2.2.

2.4 Spectral Analysis

Båth (1974) presents an excellent text on spectral or time series analysis in the frequency domain. A continuous real-valued wave record $\zeta(t)$ may be

Surface elevation	ζ	$=$	$\zeta_a \cos(kx - \omega t)$
Horizontal velocity	u	$=$	$\zeta_a \omega \dfrac{\cosh k(h+z)}{\sinh kh} \cos(kx - \omega t)$
Vertical velocity	w	$=$	$\zeta_a \omega \dfrac{\sinh k(h+z)}{\sinh kh} \sin(kx - \omega t)$
Horizontal acceleration	$\dfrac{\partial u}{\partial t}$	$=$	$\zeta_a \omega^2 \dfrac{\cosh k(h+z)}{\sinh kh} \sin(kx - \omega t)$
Vertical acceleration	$\dfrac{\partial w}{\partial t}$	$=$	$-\zeta_a \omega^2 \dfrac{\sinh k(h+z)}{\sinh kh} \cos(kx - \omega t)$
Dynamic pressure	p_d	$=$	$\rho g \zeta_a \dfrac{\cosh k(h+z)}{\cosh kh} \cos(kx - \omega t)$
Pressure	p	$=$	$p_d - \rho g z$

Table 2.2: Predictive equations for linear progressive waves.

represented in the frequency domain by its complex Fourier transform $F(\omega)$:

$$F(\omega) = \int_{-\infty}^{+\infty} \zeta(t)\, e^{-i\omega t}\, dt \tag{2.23}$$

where t denotes the time and $\omega = 2\pi f$ the angular frequency. Applying the inverse Fourier transformation restores the original record $\zeta(t)$:

$$\zeta(t) = \frac{1}{2\pi} \int_{-\infty}^{+\infty} F(\omega)\, e^{i\omega t}\, d\omega. \tag{2.24}$$

In polar notation, the complex Fourier transform can be expressed by its amplitude and phase spectrum:

$$F(\omega) = |F(\omega)|\, e^{i\, arg F(\omega)} \tag{2.25}$$

where $i = \sqrt{-1}$ is the imaginary unit. In practice, it is necessary to adopt a discrete and finite form of the Fourier transform pair described by Eqs. (2.23)

and (2.24):

$$F(r\Delta\omega) = \Delta t \sum_{k=0}^{N-1} \zeta(k\Delta t)\, e^{-i2\pi rk/N} \qquad (2.26)$$

$$r = 0, 1, 2, \ldots, N/2$$

$$\zeta(k\Delta t) = \frac{\Delta\omega}{2\pi} \sum_{r=0}^{N/2} F(r\Delta\omega)\, e^{i2\pi rk/N} \qquad (2.27)$$

$$k = 0, 1, 2, \ldots, (N-1)$$

where the values $\zeta(k\Delta t)$ represent the available data points of the discrete finite wave record with Δt denoting the sampling rate and $\Delta\omega = 2\pi/(N\Delta t)$ the frequency resolution. The summation in Eqs. (2.26) and (2.27) can be efficiently completed by the fast Fourier transform (FFT) and its inverse algorithm (IFFT) (Brigham, 1974; Conte and De Boor, 1980). Note that the record is sampled through a window $w(t)$ in time of duration $N\Delta t$ at discrete points on a Dirac comb $c(t)$. Hence the net Fourier transform is (Båth, 1974):

$$F(\omega)_{net} = \int_{-\infty}^{+\infty} \zeta(t)\, w(t)\, c(t)\, e^{-i\omega t}\, dt \qquad (2.28)$$

$$= \frac{F(\omega) * W(\omega) * C(\omega)}{4\,\pi^2} \qquad (2.29)$$

where $W(\omega)$ and $C(\omega)$ are the Fourier transforms of the window function and the Dirac comb. The asterisk operator denotes convolution which corresponds to a moving weighted average in the frequency domain. In this study, the window function is chosen to be simply a rectangular box, which implies some side band leakage to adjacent frequencies.

The Fourier transform $F(\omega)$ and the variance spectrum $E(\omega)$ are related through Parseval's theorem, which states for the single-sided discrete variance spectrum:

$$E(r\Delta\omega) = \frac{1}{\pi\, N\, \Delta t}\, |F(r\Delta\omega)|^2. \qquad (2.30)$$

Jenkins and Watts (1968) showed that the confidence limits on a spectral estimate $\widehat{E}(\omega)$ of the actual spectral ordinate $E(\omega)$ are:

$$\Pr\left\{ \left[\frac{\mathrm{n}}{\chi^2_{\mathrm{n},1-\mathrm{u}/2}} \right] \widehat{E}(\omega) \;\leq\; E(\omega) \;<\; \left[\frac{\mathrm{n}}{\chi^2_{\mathrm{n},\mathrm{u}/2}} \right] \widehat{E}(\omega) \right\} = 1 - \mathrm{u}. \qquad (2.31)$$

The dimensionless terms in the brackets define the lower and upper confidence limits as a function of the chi-square χ^2 distribution for n degrees of freedom at confidence level u. Since the raw spectral estimate determined directly from the FFT has $\mathrm{n} = 2$ degrees of freedom, a moving average over $2N_n$ adjacent points in the frequency domain yields $\mathrm{n} = 2\,(2N_n + 1)$ degrees of freedom. In this work, the statistical variability at the 95% confidence level is significantly reduced by selecting $N_n = 5$; compare Table 2.3.

n	$\chi^2_{\mathrm{n,1-u/2}}$	$\chi^2_{\mathrm{n,u/2}}$	$n/\chi^2_{\mathrm{n,1-u/2}}$	$n/\chi^2_{\mathrm{n,u/2}}$
2	7.38	0.0506	0.27	39.5
22	36.8	11.0	0.60	2.0
100	129.6	74.2	0.77	1.35

Table 2.3: Confidence limits at the 95% level ($\mathrm{u} = 0.05$).

It is important to note that the physical interpretation of wave spectra becomes difficult in the case of distinct nonlinear free surface effects. Amplitude and phase information derived from the complex Fourier transform $F(\omega)$ are then not clearly associated with independent monochromatic waves. Further uncertainty in the analysis of wave spectra is related to the necessary truncation of the discrete finite wave record, side band leakage and smoothing, which may artificially distort the spectra shapes.

Read and Sobey (1987) point out that the phase spectrum is routinely ignored on the assumption that the Gaussian random wave model is a sufficiently complete description of a field record. They develop procedures for unwrapping and detrending the phase spectrum to provide insight into the potential identification of ordered structures, possibly wave groups, in the phase spectrum.

2.4.1 Spectral Parameters

Spectral moments are commonly used to characterize variance spectra. The nth spectral moment about zero frequency is defined as:

$$m_n \;=\; \int_0^\infty \omega^n \, E(\omega)\, d\omega \tag{2.32}$$

where m_0 is the variance σ^2 of the sea state. The nth spectral moment about the mean frequency $\bar{\omega}$ is similarly stated as:

$$\mu_n \;=\; \int_0^\infty (\omega - \bar{\omega})^n \, E(\omega)\, d\omega \tag{2.33}$$

and it can be easily shown that there are explicit relationships among the moments:

$$\mu_0 = m_0 = \sigma^2, \quad \mu_1 = 0 \quad \text{and} \quad \mu_2 = m_2 - \frac{m_1^2}{m_0}. \tag{2.34}$$

A number of theories require estimates of the m_4 moment. Sobey (1999) points out that this parameter is not reliable, since the erratic high frequency spectral tail is greatly magnified by the ω^4 factor. In discrete estimation, further difficulty is associated with significant contributions beyond the Nyquist frequency $f_{NY} = 1/(2\Delta t)$, which is the upper limit of frequency resolution. Higher moments are even less reliable. Common *characteristic frequencies* are the mean frequency:

$$\bar{\omega} = \frac{m_1}{m_0} \quad \text{or} \quad \bar{f} = \frac{1}{2\pi}\frac{m_1}{m_0} \tag{2.35}$$

the root-mean-square frequency:

$$\omega_z = \left(\frac{m_2}{m_0}\right)^{1/2} \quad \text{or} \quad f_z = \frac{1}{2\pi}\left(\frac{m_2}{m_0}\right)^{1/2} \tag{2.36}$$

which is is also known as the mean zero-crossing frequency, and the peak frequency:

$$\omega_p = \frac{\int_0^\infty \omega\, E^P(\omega)\, d\omega}{\int_0^\infty E^P(\omega)\, d\omega} \tag{2.37}$$

where P is usually between 5 and 8 to weigh the result strongly toward the visual peak of the spectrum (Sobey and Young, 1986; Mansard and Funke, 1988). For common wave spectra, $\omega_p < \bar{\omega} < \omega_z$. Another useful parameter is the *spectral width* defined by Longuet-Higgins (1975):

$$\nu = \sqrt{\frac{\mu_2}{\bar{\omega}^2\, m_0}} = \sqrt{\frac{m_0\, m_2}{m_1^2} - 1} \tag{2.38}$$

where ν is of order 0.5 for sea conditions and 0.15 for swell.

2.4.2 Empirical Sea Spectra

Universal spectral shapes of growing wind seas play a vital role in coastal and ocean engineering. In deep water, the *Pierson-Moskowitz* spectrum is defined as:

$$\frac{\omega_p^4\, E(q)}{g^2} = \alpha\, q^{-5}\, e^{-1.25 q^{-4}} \tag{2.39}$$

where $q = \omega/\omega_p = f/f_p$ represents the normalized frequency with respect to the peak frequency $f_p = 1/T_p$, g is the acceleration due to gravity and $E(q) = \omega_p\, E(\omega)$. The Phillips coefficient α is a function of the wind shear velocity at the air-water interface and the atmospheric pressure (Phillips, 1977). The *Jonswap* form, introduced by Hasselmann et al. (1973), more accurately describes the spectrum shape in the North Sea:

$$\frac{\omega_p^4\, E(q)}{g^2} \;=\; \alpha\; q^{-5}\; e^{-1.25q^{-4}}\; \gamma^{e^{-\frac{r^2}{2}}}. \tag{2.40}$$

The Jonswap peak enhancement factor γ is 3.3 for the mean spectrum form, 7 for the sharp form and 1 for the Pierson-Moskowitz spectrum. The spectral width parameter σ_* is set to 0.07 for $q \leq 1$ and 0.09 for $q > 1$ with $r = (q-1)/\sigma_*$. The finite depth variant of the Jonswap spectrum is called the *TMA* form (Bouws et al., 1985):

$$\frac{\omega_p^4\, E(q)}{g^2} \;=\; \alpha\; q^{-5}\; \frac{\tanh^2(kh)}{1 + 2kh/\sinh(2kh)}\; e^{-1.25q^{-4}}\; \gamma^{e^{-\frac{r^2}{2}}} \tag{2.41}$$

where h is the water depth. The frequency-dependent wave number k is calculated from the linear dispersion relationship $\omega^2 = gk\,\tanh(kh)$. Since the zeroth spectral moment:

$$m_0 \;= \int_0^\infty E(\omega)\, d\omega \;= \int_0^\infty E(q)\, dq \;=\; \alpha \int_0^\infty \frac{E(q)}{\alpha}\, dq \tag{2.42}$$

and the significant wave height are related by $H_s = 4\sqrt{m_o}$, the Phillips coefficient α may be determined from a given variance spectrum by:

$$\alpha \;=\; \frac{H_s^2}{16 \displaystyle\int_0^\infty \frac{E(q)}{\alpha}\, dq}. \tag{2.43}$$

Chapter 3

Numerical Simulation of Nonlinear Waves

3.1 Introduction

The simulation of two-dimensional nonlinear waves in the numerical wave tank shown in Fig. 2.1 is based on potential flow theory, which is described in detail in Section 2.2. The mixed Eulerian-Lagrangian method introduced by Longuet-Higgins and Cokelet (1976) is applied to solve the Laplace equation as a nonlinear initial boundary value problem in the time domain. The general procedure is illustrated in Fig. 3.1. The computer program has been developed by the author in Fortran 90 and starts by reading the time dependent wave board motion and certain input parameters defining mesh size, time step, termination time and desired output. At each time step the velocity potential is calculated for the current boundary conditions in the entire fluid domain with the finite element method presented by Wu and Eatock Taylor (1994, 1995). From this solution the velocities at the free surface are determined by second-order differences. The new surface elevation, the associated velocity potential and the position of the wave board are updated. To develop the solution in the time domain, the classical fourth-order Runge-Kutta formula is applied. At each time step a new boundary-fitted mesh is created. The procedure is repeated until the desired termination time is reached, or the waves become unstable and break.

The finite element method and the mesh generation are described in the next two sections. The explicit fourth-order Runge-Kutta formula is presented in Section 3.4. A local filtering technique suppressing artificial high frequency oscillations is introduced in Section 3.5. As part of the numerical verification, the influence of the spatial and temporal resolution is investigated in Section 3.6.1, and the performance of the numerical wave absorption in 3.6.2. Finally, numerical results are validated by experimental data in Section 3.6.3.

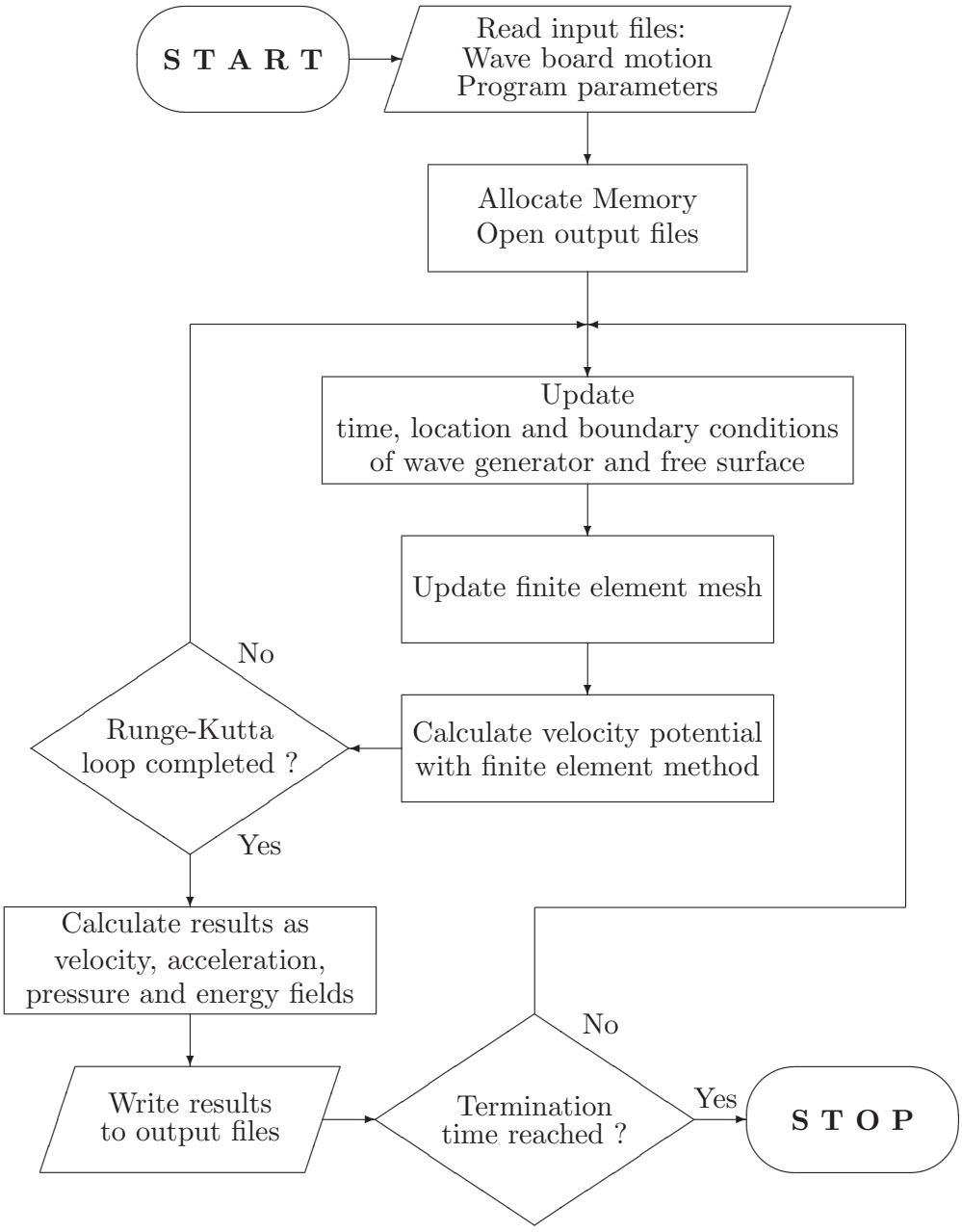

Figure 3.1: Flowchart of the computer program to simulate the propagation of two-dimensional nonlinear wave trains in the numerical wave tank.

3.2 Finite Element Method

The finite element method used in this work is presented by Wu and Eatock Taylor (1994, 1995). At each time step the Laplace equation is solved for Neumann and Dirichlet boundary conditions on a closed solution domain defining the numerical wave tank (Fig. 2.1). The fluid domain Ω is divided into triangular finite elements with a total of m nodes. The velocity potential ϕ is described in terms of nodal values of the potential ϕ_j and linear shape functions $N_j(x, z)$:

$$\phi(x, z) \;=\; \sum_{j=1}^{m} \phi_j N_j(x, z). \tag{3.1}$$

According to the Galerkin method, the weighing functions are chosen to be the shape functions themselves, making the residual orthogonal to the space of the shape functions:

$$\int_{\Omega} \nabla^2\phi \, N_i \, d\Omega \;=\; 0. \tag{3.2}$$

Since:

$$\nabla\Big(\nabla\phi \, N_i\Big) \;=\; \nabla^2\phi \, N_i \;+\; \nabla\phi \, \nabla N_i \tag{3.3}$$

it follows that:

$$\int_{\Omega} \Big(\nabla\Big(\nabla\phi \, N_i\Big) \;-\; \nabla\phi \, \nabla N_i\Big) \, d\Omega \;=\; 0. \tag{3.4}$$

Application of the Gauss theorem yields:

$$\int_{\Gamma} N_i \, \frac{\partial\phi}{\partial n} \, d\Gamma - \int_{\Omega} \nabla N_i \, \sum_{j=1}^{m} \phi_j \nabla N_j \, d\Omega \;=\; 0 \tag{3.5}$$

where Γ is the boundary and n the normal direction pointing out of the fluid domain Ω. The substitution of the boundary conditions defined in Fig. 2.1 and Table 3.1 together with Eq. (3.1) into Eq. (3.5) results in:

$$\begin{aligned}\left[\int_{\Omega} \nabla N_i \, \sum_{j=1}^{m} \phi_j \nabla N_j \, d\Omega\right]_{j \notin \Gamma_S} \;&=\; -\int_{\Gamma_B} N_i \, \dot{x}_B(t) \, d\Gamma \\ -\left[\int_{\Omega} \nabla N_i \, \sum_{j=1}^{m} \phi_j \nabla N_j \, d\Omega\right]_{j \in \Gamma_S} &\qquad (i \notin \Gamma_S).\end{aligned} \tag{3.6}$$

Free surface	Γ_S :	$\phi(x,z,t)$	at	$z = \zeta(x,t)$
Wave board	Γ_B :	$\dfrac{\partial\phi}{\partial n} = -\dot{x}_B(t)$	at	$x = x_B(t)$
Wall	Γ_W :	$\dfrac{\partial\phi}{\partial n} = 0$	at	$x = l$ and $z = -h$

Table 3.1: Dirichlet and Neumann boundary conditions of the finite element method.

The horizontal velocity $\dot{x}_B(t)$ is easily determined from the wave board motion $x_B(t)$. The boundary integral along the free surface:

$$\int_{\Gamma_S} N_i \, \frac{\partial\phi}{\partial n} \, d\Gamma \;=\; 0 \qquad (i \notin \Gamma_S) \tag{3.7}$$

is omitted in Eq. (3.6) because the shape functions N_i are zero for nodes $i \notin \Gamma_S$. Eq. (3.6) can be written in matrix form:

$$\boldsymbol{A}\,\boldsymbol{\phi} \;=\; \boldsymbol{B} \tag{3.8}$$

with coefficients:

$$\boldsymbol{A}(i,j) \;=\; \int_{\Omega} \nabla N_i \, \nabla N_i \, d\Omega \qquad (i,j \notin \Gamma_S), \tag{3.9}$$

$$\boldsymbol{B}(i) \;=\; -\int_{\Gamma_B} N_i \, \dot{x}_B(t) \, d\Gamma - \int_{\Omega} \nabla N_i \, \sum_{j=1}^{m} \phi_j \nabla N_j \, d\Omega \qquad (i \notin \Gamma_S,\; j \in \Gamma_S). \tag{3.10}$$

Since the derivatives of the linear shape functions with respect to x and z are constant, the matrix $\boldsymbol{A}$ is calculated conveniently from the areas of the triangles. The bandwidth of the symmetric, positive definite matrix $\boldsymbol{A}$ is reduced to a minimum by appropriate numbering of the nodes. Thus, only the upper band has to be stored, which reduces the required memory significantly. Eq. (3.8) is solved by Cholesky decomposition.

3.3 Mesh Generation

The mesh generation is kept simple to reduce the computational burden and is based on an analytical expression. The entire domain of the numerical wave

tank is divided in the x-direction by $NX+1$ vertical lines whose positions x_i depend on the nodes at the free surface ζ_i which are treated as particles in the mixed Eulerian-Lagrangian method. The locations of these nodes change with time and are calculated by Eqs. (2.11). In the z-direction the $NZ+1$ nodes are exponentially distributed:

$$z_{i,j} \;=\; -\,(h+\zeta_i)\;\frac{1-\exp\Big(\alpha_z\,(h+\zeta_i)\,(NZ+1-j)/NZ\Big)}{1-\exp\Big(\alpha_z\,(h+\zeta_i)\Big)}\;+\;\zeta_i$$

$$(i=1,2,\ldots,NX+1;\; j=1,2,\ldots,NZ+1) \tag{3.11}$$

where h represents the water depth. The parameter α_z determines the narrowness of the mesh near the free surface and is set to 2.0. The total number of nodes is $(NX+1)\,(NZ+1)$ and the number of triangular elements is $2\cdot NX\cdot NZ$. Fig. 3.2 shows a typical mesh.

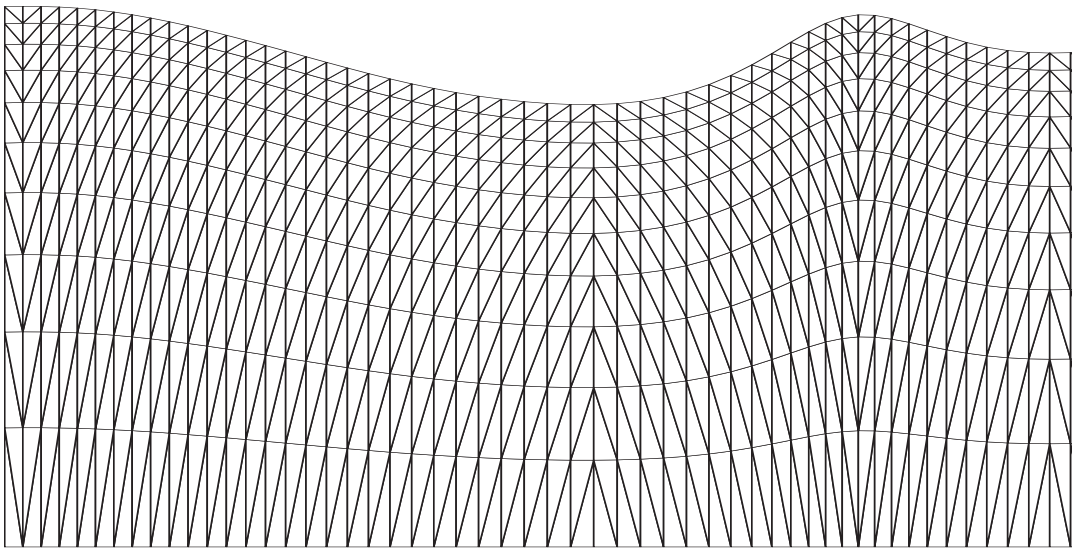

Figure 3.2: Finite element mesh.

At the beginning of the numerical simulation, the free surface nodes are uniformly distributed in the x-direction with a surface elevation of zero. Since the x-coordinate of the first node at the free surface is set to the position of the wave board, the horizontal gap to the second node increases in time due to the Lagrangian motion characteristic. If the gap between any two nodes is greater than twice the initial horizontal grid spacing, an additional node will be inserted automatically by linear interpolation of coordinates and potential values of the adjacent nodes.

To determine the particle velocities, the *physical plane* with independent variables x and z will be transformed to the *computational plane* with variables ξ and η. The mapping for the boundary-fitted coordinate system is given by:

$$\xi = x, \tag{3.12}$$

$$\eta = \frac{h+z}{h+\zeta(x)}. \tag{3.13}$$

Applying the chain rule of differential calculus:

$$\frac{\partial}{\partial x} = \frac{\partial}{\partial \xi}\frac{\partial \xi}{\partial x} + \frac{\partial}{\partial \eta}\frac{\partial \eta}{\partial x} \tag{3.14}$$

$$\frac{\partial}{\partial z} = \frac{\partial}{\partial \xi}\frac{\partial \xi}{\partial z} + \frac{\partial}{\partial \eta}\frac{\partial \eta}{\partial z} \tag{3.15}$$

yields the derivatives:

$$\frac{\partial}{\partial x} = \frac{\partial}{\partial \xi} - \frac{\partial}{\partial \eta}\frac{h+z}{\big(h+\zeta(x)\big)^2}\frac{\partial \zeta(x)}{\partial x}, \tag{3.16}$$

$$\frac{\partial}{\partial z} = \frac{\partial}{\partial \eta}\frac{1}{h+\zeta(x)}. \tag{3.17}$$

The velocities are calculated in the computational plane as second-order differences of the potential ϕ with respect to ξ and η and then transformed by Eqs. (3.16) and (3.17).

3.4 Runge-Kutta Formula

The numerical solution is developed in time domain by applying the classical fourth-order Runge-Kutta formula to the nodes at the free surface and the associated velocity potential. The current state at time step k is described by the matrix:

$$\boldsymbol{S}_k = (\boldsymbol{x}_k,\, \boldsymbol{z}_k,\, \boldsymbol{\phi}_k)^T \tag{3.18}$$

with the vector entries defining the elevation and potential along the nodes of the free surface:

$$\begin{aligned} \boldsymbol{x}_k &= (x_1,\, x_2,\, \ldots,\, x_{NX+1})_k^T \\ \boldsymbol{z}_k &= (z_1,\, z_2,\, \ldots,\, z_{NX+1})_k^T \\ \boldsymbol{\phi}_k &= (\phi_1,\, \phi_2,\, \ldots,\, \phi_{NX+1})_k^T. \end{aligned} \tag{3.19}$$

The time-derivative of the matrix:

$$\frac{D\boldsymbol{S}_k}{Dt} = \left(\frac{D\boldsymbol{x}_k}{Dt}, \frac{D\boldsymbol{z}_k}{Dt}, \frac{D\boldsymbol{\phi}_k}{Dt} \right)^T = \boldsymbol{F}(t_k, \boldsymbol{S}_k) \tag{3.20}$$

corresponds to the nonlinear free surface boundary conditions stated in Eqs. (2.11) to (2.15) of Section 2.2.1 and is calculated from the known field of the velocity potential at time step k. The explicit Runge-Kutta scheme requires four evaluations of the right-hand side per time step Δt:

$$\begin{aligned}
\boldsymbol{S}_1 &= \Delta t\, \boldsymbol{F}(t_k, \boldsymbol{S}_k) \\
\boldsymbol{S}_2 &= \Delta t\, \boldsymbol{F}(t_k + \Delta t/2, \boldsymbol{S}_k + \boldsymbol{S}_1/2) \\
\boldsymbol{S}_3 &= \Delta t\, \boldsymbol{F}(t_k + \Delta t/2, \boldsymbol{S}_k + \boldsymbol{S}_2/2) \\
\boldsymbol{S}_4 &= \Delta t\, \boldsymbol{F}(t_k + \Delta t, \boldsymbol{S}_k + \boldsymbol{S}_3) \\
\boldsymbol{S}_{k+1} &= \boldsymbol{S}_k + \frac{\boldsymbol{S}_1}{6} + \frac{\boldsymbol{S}_2}{3} + \frac{\boldsymbol{S}_3}{3} + \frac{\boldsymbol{S}_4}{6}
\end{aligned} \tag{3.21}$$

in order to determine the new surface elevation with the associated velocity potential at time step $k+1$. These conditions together with the updated location and velocity of the wave board define the new boundary conditions for computing the velocity potential in the entire flow field with the finite element method. A detailed investigation of various methods for solving ordinary differential equations is presented by Schwarz (1993).

3.5 Local Filtering

Numerical instabilities and artificial high frequency oscillations are common phenomena in numerical integration. Filtering techniques are well established to cope with these problems in numerically simulating free surface flows. *Global* multi-point filtering techniques perform smoothing on all grid nodes at a given time (Longuet-Higgins and Cokelet, 1976). This is in general a shortcoming since smoothing might not be necessary for all grid points. In addition, numerical dissipation is introduced and the dispersion relationship violated.

In this study, a *local* three-point filtering technique introduced by Sheng et al. (1978) is applied to the free surface elevation and associated velocity potential:

$$\zeta_i = \frac{1}{n} \left(\zeta_{i+1} + (n-2)\, \zeta_i + \zeta_{i-1} \right) \tag{3.22}$$

$$\phi_i = \frac{1}{n} \left(\phi_{i+1} + (n-2)\, \phi_i + \phi_{i-1} \right) \tag{3.23}$$

with the weighting factor $n \geq 4$ controlling the filtering efficiency. The smoothing operation will only be performed at grid node i either if:

$$\text{condition 1:} \quad \begin{cases} |\zeta_{i+1} - \zeta_i| + |\zeta_i - \zeta_{i-1}| \geq \dfrac{n}{n-2} |\zeta_{i+1} - \zeta_{i-1}| \\ \text{and} \\ (\zeta_{i+2} - 2\,\zeta_{i+1} + \zeta_i)\,(\zeta_{i+1} - 2\,\zeta_i + \zeta_{i-1}) < 0 \end{cases} \tag{3.24}$$

or if:

$$\text{condition 2:} \quad \begin{cases} |\zeta_{i+1} - \zeta_i| + |\zeta_i - \zeta_{i-1}| \geq \dfrac{n}{n-2} |\zeta_{i+1} - \zeta_{i-1}| \\ \text{and} \\ (\zeta_{i-2} - 2\,\zeta_{i-1} + \zeta_i)\,(\zeta_{i+1} - 2\,\zeta_i + \zeta_{i-1}) < 0 \end{cases} \tag{3.25}$$

is satisfied. The first part of the conditions checks for jumps of the free surface between nodes $i-1$ and $i+1$, and the second part for sign changes in the curvature at the adjacent nodes. In the present work another condition is introduced in terms of the Courant number which is defined in Eq. (3.27):

$$\text{condition 3:} \quad Cn \geq 0.2 \tag{3.26}$$

since only steep waves close to breaking need to be smoothed. The weighting factor is set to $n = 10$.

3.6 Numerical Verification

3.6.1 Spatial and Temporal Resolution

A Neumann stability analysis for the fourth-order Runge-Kutta scheme with linearized free surface boundary conditions yields the stability condition in terms of the Courant number:

$$Cn = \frac{\pi\, g}{8} \frac{\Delta t^2}{\Delta x} \leq 1 \quad \Longrightarrow \quad \Delta t^2 \leq \frac{8\,\Delta x}{\pi\, g} \tag{3.27}$$

where Δt is the time step and Δx the local grid spacing (Dommermuth and Yue, 1987). This result suggests that, for a fixed time step, numerical instabilities of the nonlinear simulation may be encountered in the case of very small grid spacings which are related to the concentration of Lagrangian points on the free surface. This critical particle concentration is typical for breaking waves, which are beyond the scope of this study.

The influence of the spatial and temporal resolution on the numerical solution is illustrated for a regular wave with height $H = 0.86\,m$, length

$L = 14.26\,m$ and period $T = 3\,s$, propagating in a $l = 250\,m$ long wave tank with water depth of $h = 5\,m$.

For a constant time step $\Delta t = T/30$, Fig. 3.3 shows the convergence of the solution with decreasing grid spacing Δx. The number of grid nodes in the horizontal direction is determined by $NX+1 \approx l/\Delta x+1$, and the number in the vertical direction by $NZ+1 \approx h/\Delta x+3$. Note that the initially uniform horizontal distribution of the nodes adapts to the motion of the Lagrangian points at the free surface, and that the nodes are exponentially distributed in the vertical direction. As can be seen from the figure, a reasonable spatial resolution is 30 nodes per wave length, which corresponds to $NX = 520$ and $NZ = 12$. For this particular spatial discretization, the convergence of the solution with decreasing time step Δt is presented in Fig. 3.4. The time step of $\Delta t = T/15$ is found to be acceptable; however, $\Delta t = T/30$ resolves the energy flux more accurately.

In case of irregular waves, the temporal and spatial resolution is chosen to correlate with characteristic measures of the variance spectrum in terms of the mean period $\bar{T}$ and its associated wave length $\bar{L}$ which is determined by the dispersion relationship. Both measures are discretized with approximately 30 points in the numerical simulation.

3.6.2 Numerical Wave Absorption

The numerical absorption method stated in Eqs. (2.13) - (2.16) of Section 2.2.1 has proven to efficiently absorb nonlinear regular waves (Cointe et al., 1990; Tanizawa, 1996). The performance of this technique in case of irregular waves has been studied systematically and is presented exemplarily for a transient wave packet. Free surface elevations, total energy and energy flux are investigated. The length and strength of the numerical beach are defined in terms of the mean wave length and mean frequency as characteristic measures of the variance spectrum:

$$l_{beach} \;=\; 2\,\bar{L} \quad \text{and} \quad \omega_{beach} = \bar{\omega}\,/\,2. \tag{3.28}$$

The spectral and numerical parameters used in the simulation of the transient wave packet are compiled in Table 3.2. The point of focus is $x/l = 0.50$ and $t/T_p = 21.35$ with maximum wave height $H_{max}/h = 0.28$. As shown in Fig. 3.5, the total energy of the wave packet is significantly reduced by the application of this absorption technique. Less than 1 % of the energy remains at $t/T_p = 37.5$ in the wave tank. Fig. 3.6 shows the energy flux which provides information about the direction of the energy transport at a fixed location. A positive sign indicates wave propagation toward the numerical

beach and a negative one toward the wave generator. No energy is visibly passing the location $x/l = 0.6$ in the case of wave absorption. Snap shots of the surface elevation presented in the same figure reveal that a long wave of low amplitude is still present in the wave tank at $t/T_p = 37.5$.

Variance	m_0	=	$0.006\,m^2$
Significant wave height	$H_s = 4\sqrt{m_0}$	=	$0.31\,m$
Peak period	T_p	=	$4.80\,s$
Mean period	$\bar{T}$	=	$4.15\,s$
Mean frequency	$\bar{\omega}$	=	$1.51\,rad/s$
Mean wave length	$\bar{L}$	=	$21.96\,m$
Tank length	l	=	$250.00\,m$
Water depth	h	=	$4.00\,m$
Spatial resolution	$\Delta x = \bar{L}/30$	=	$0.73\,m$
Temporal resolution	$\Delta t = \bar{T}/30$	=	$0.14\,s$
Number of horizontal grid nodes	$NX + 1 \approx l/\Delta x + 1$	=	344
Number of vertical grid nodes	$NZ + 1 \approx h/\Delta x + 3$	=	9
Length of numerical beach	$l_{beach} = 2\,\bar{L}$	=	$43.92\,m$
Strength of numerical beach	$\omega_{beach} = \bar{\omega}/2$	=	$0.76\,rad/s$

Table 3.2: Parameters for verification of numerical wave absorption.

3.6.3 Experimental Validation

The numerical results are validated by experimental investigations conducted at the Large Wave Tank (GWK) Hannover ($324\,m \times 5\,m \times 7\,m$) with a piston-type wave generator. For different test signals, the wave elevations were measured by stationary wave gauges at fixed positions.

Results are presented for an irregular wave train characterized by the spectral parameters given in Table 3.3. The mean period $\bar{T}$ and the related mean wave length $\bar{L}$ are used to determine the temporal and spatial resolution for the numerical simulation of the nonlinear wave evolution. Length and strength of the numerical beach are also defined in terms of these spectral characteristics.

Figs. 3.7 and 3.8 show the excellent agreement of numerical results and experimental measurements. High frequency oscillations may be filtered due to limited spatial and temporal resolution. The evolution of the wave field is very complex due to nonlinear free surface effects such as amplitude modulation and horizontal transport of the short waves by the long waves. The crest profile of the largest waves is sharpened and the trough profile is flattened

Variance	m_0	=	$0.038\,m^2$
Significant wave height	$H_s = 4\sqrt{m_0}$	=	$0.78\,m$
Peak period	T_p	=	$4.62\,s$
Mean period	$\bar{T}$	=	$3.76\,s$
Mean frequency	$\bar{\omega}$	=	$1.67\,rad/s$
Mean wave length	$\bar{L}$	=	$19.17\,m$
Tank length	l	=	$300.00\,m$
Water depth	h	=	$4.00\,m$
Spatial resolution	$\Delta x = \bar{L}/30$	=	$0.65\,m$
Temporal resolution	$\Delta t = \bar{T}/30$	=	$0.13\,s$
Number of horizontal grid nodes	$NX + 1 \approx l/\Delta x + 1$	=	471
Number of vertical grid nodes	$NZ + 1 \approx h/\Delta x + 3$	=	9
Length of numerical beach	$l_{beach} = 2\,\bar{L}$	=	$38.34\,m$
Strength of numerical beach	$\omega_{beach} = \bar{\omega}/2$	=	$0.84\,rad/s$

Table 3.3: Parameters for experimental validation of irregular wave train.

compared to the linear wave profile. Note that the propagation speed for the wave profile and the energy is different in deep and intermediate water depth.

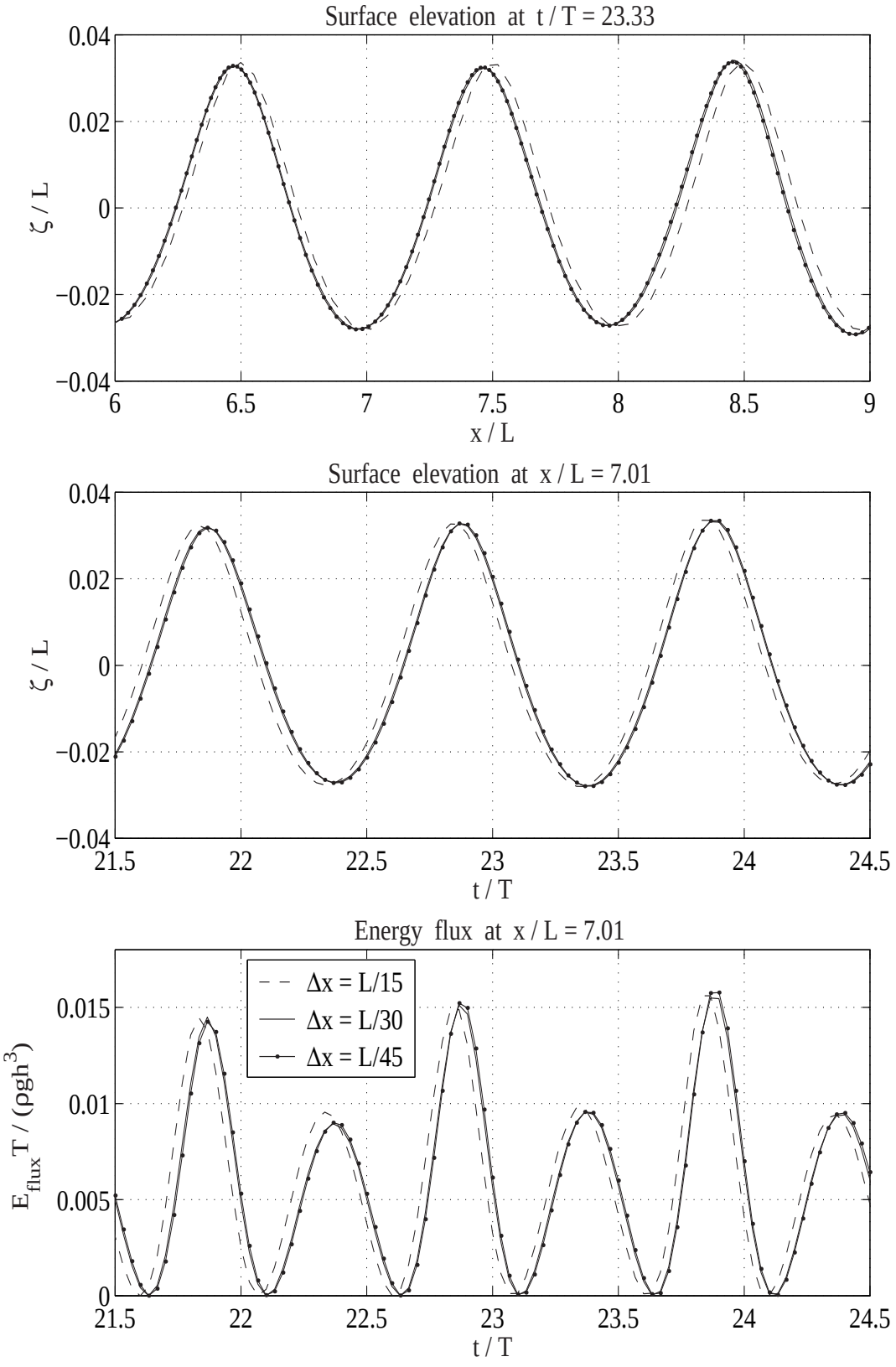

Figure 3.3: Convergence of the solution with decreasing grid spacing Δx ($NX \approx l/\Delta x$, $NZ \approx h/\Delta x + 2$, $\Delta t = T/30$).

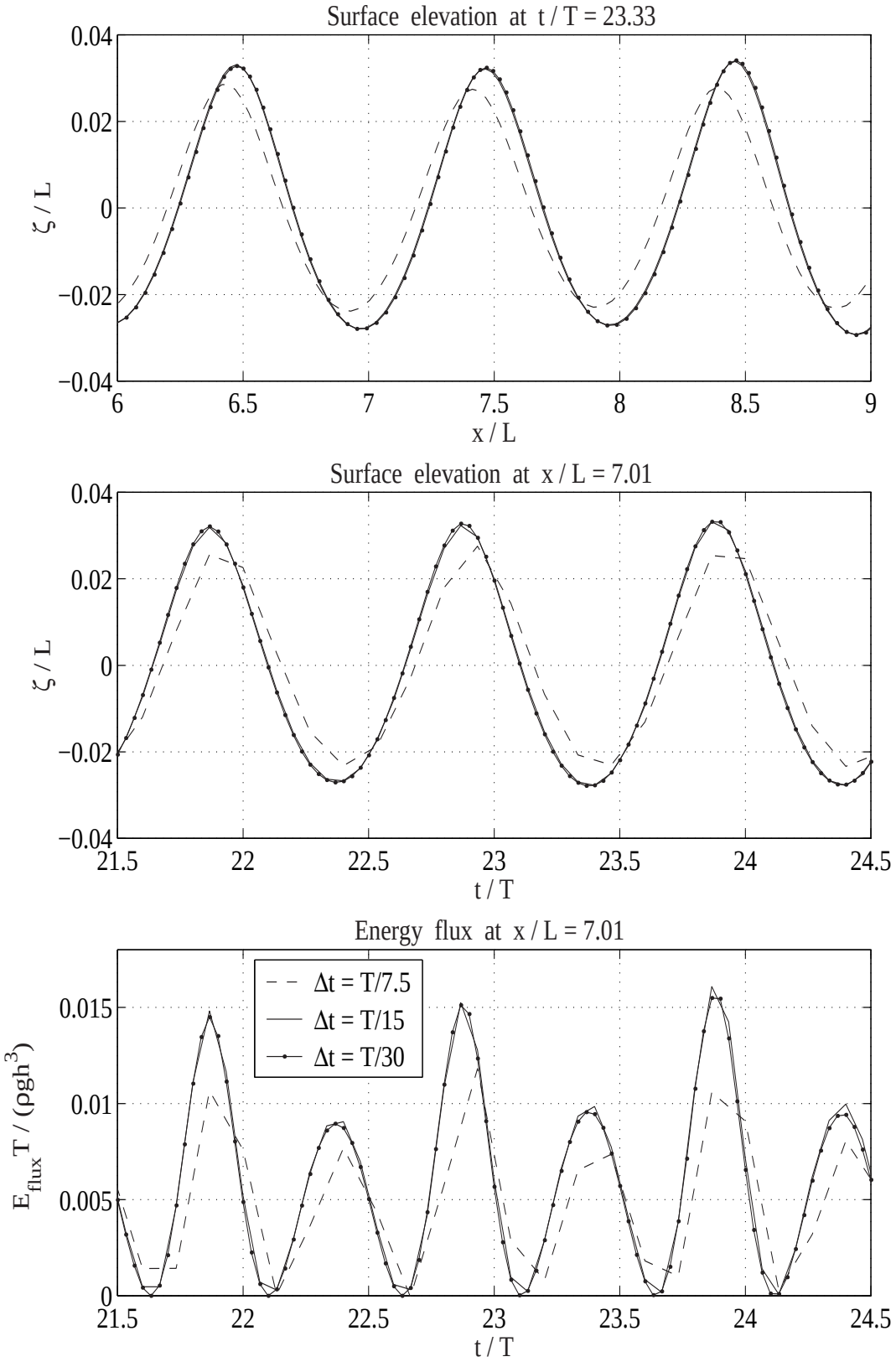

Figure 3.4: Convergence of the solution with decreasing time step Δt ($NX \approx l/\Delta x$, $NZ \approx h/\Delta x + 2$, $\Delta x = L/30$).

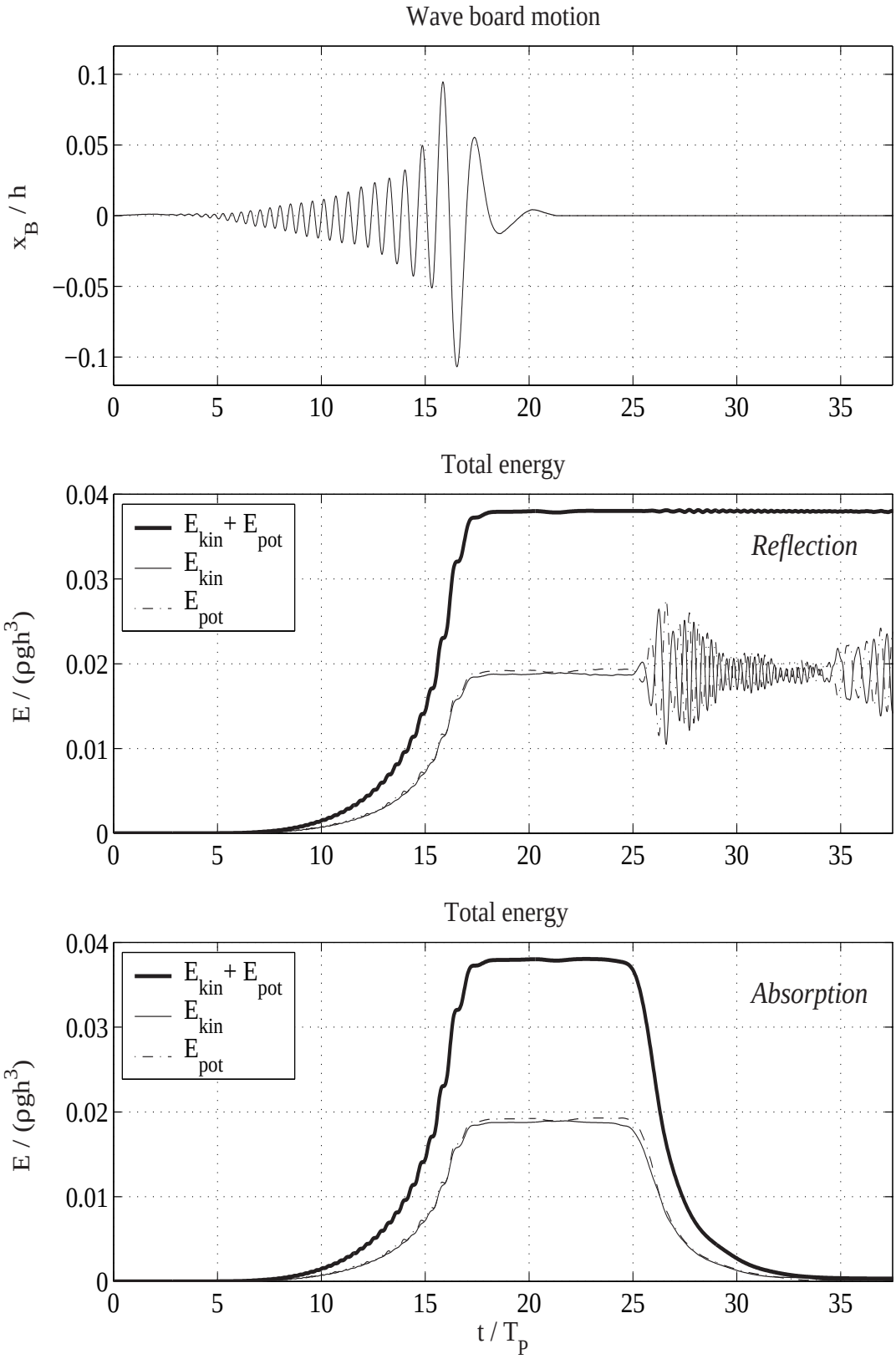

Figure 3.5: (I) Verification of numerical wave absorption.

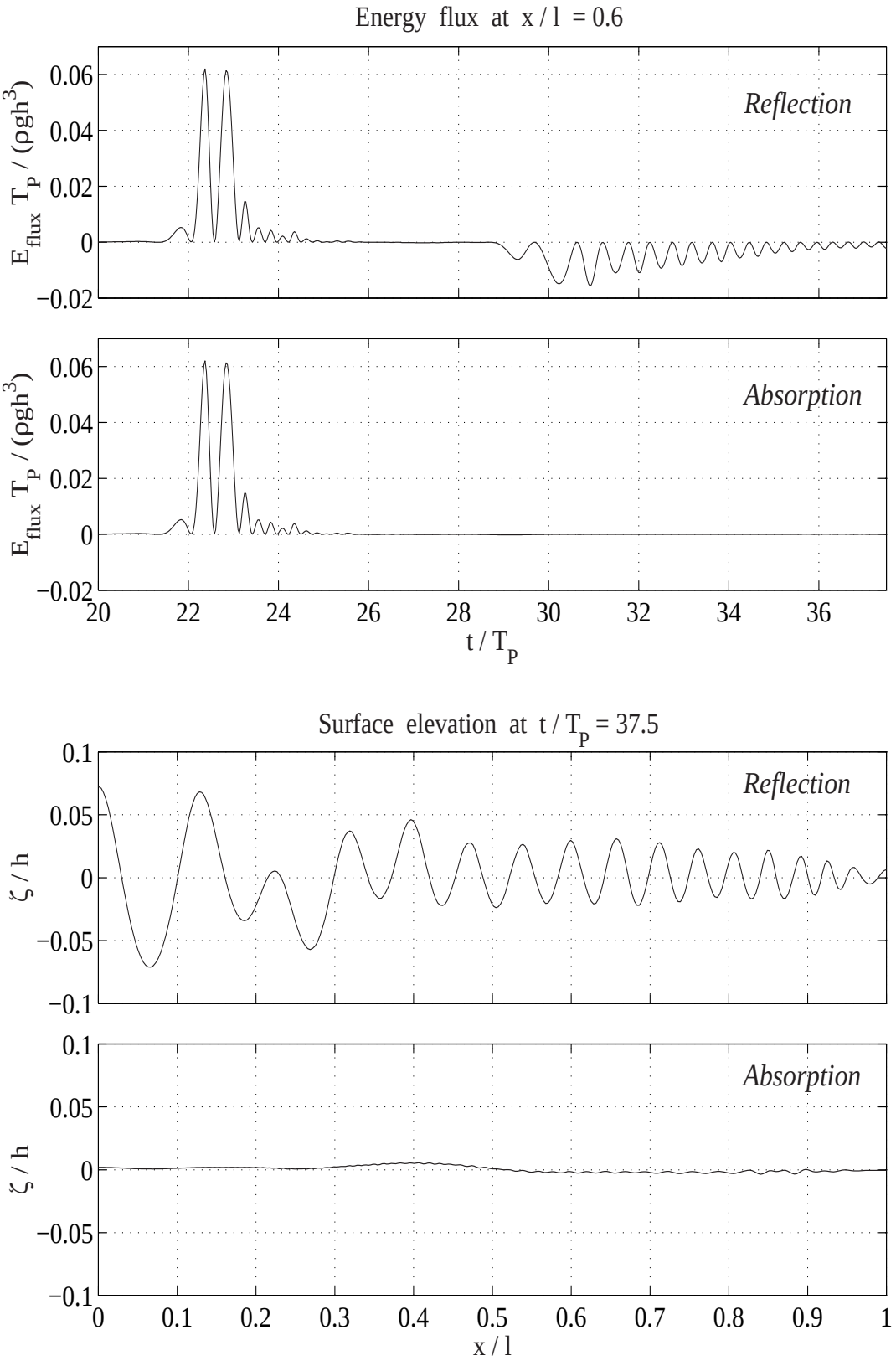

Figure 3.6: (II) Verification of numerical wave absorption.

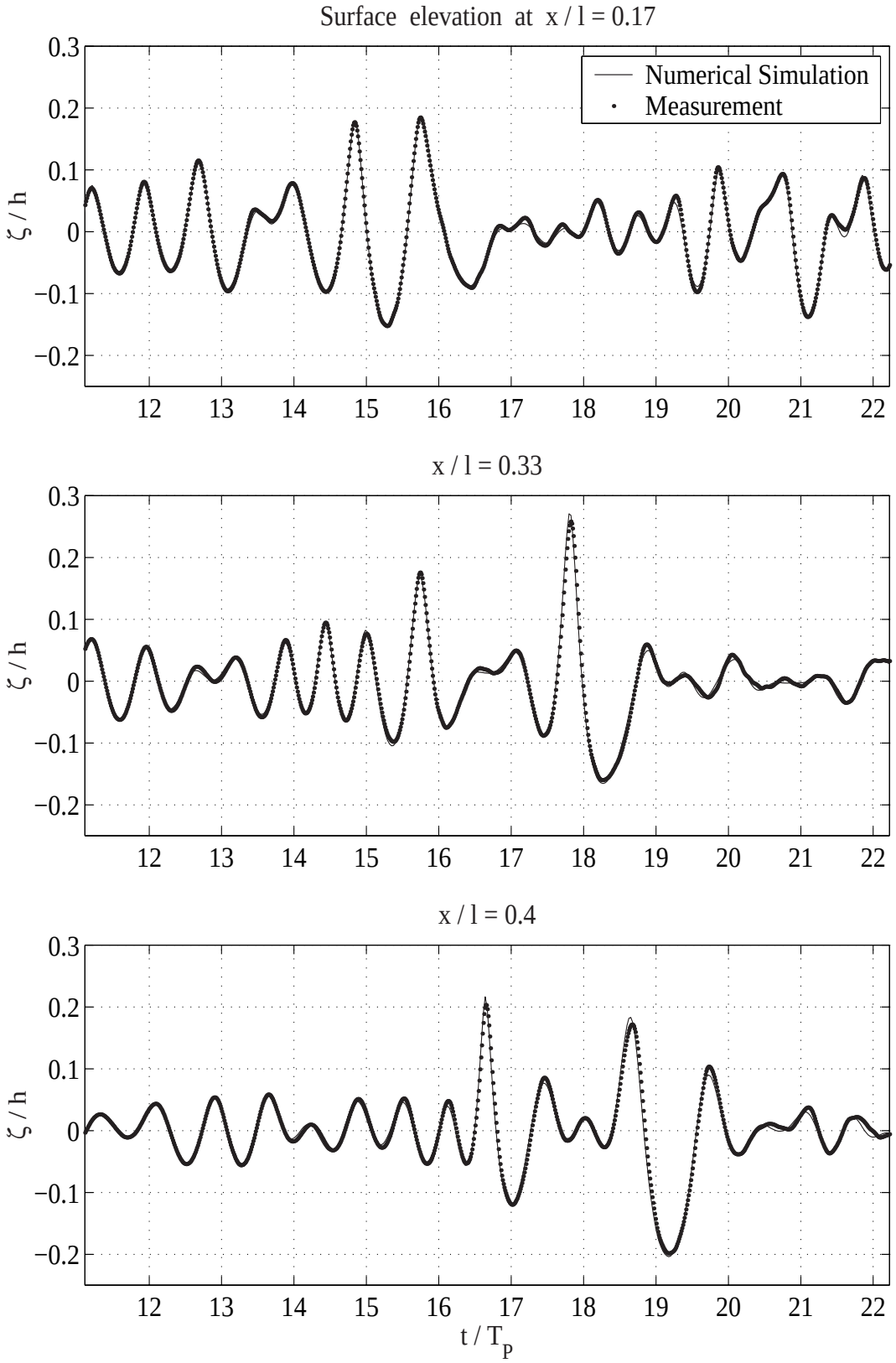

Figure 3.7: (I) Validation of numerical results by laboratory measurements.

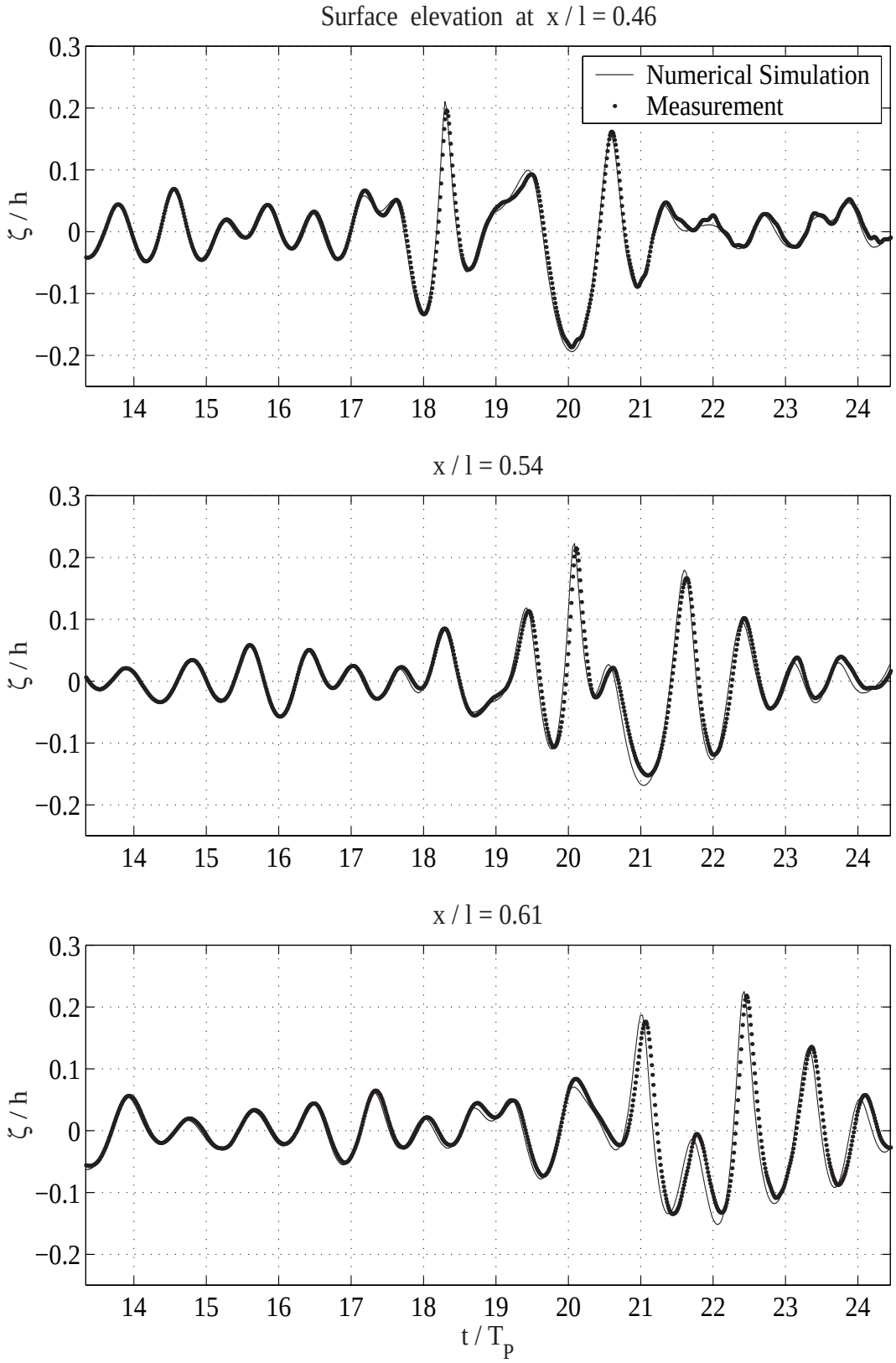

Figure 3.8: (II) Validation of numerical results by laboratory measurements.

Chapter 4

Wavelet Analysis

4.1 Introduction

Wavelet analysis is a new mathematical tool which is now broadly applied in many different disciplines, including signal processing, data and image compression, solutions of partial differential equations, modeling of multiscale phenomena, and statistics. It provides a systematic way to represent and analyze multiscale structures prevalent in nature and engineering.

Wavelet theory originates from the theory of signals. Goupillaud et al. (1984) present a new transformation method for investigating signals in the frequency domain. This wavelet transform has been developed to cope with the shortcomings of the Fourier transform and its short-time variant. Modern wavelet research is aimed at creating a set of basis, or more general, expansion functions to efficiently localize the characteristics of a function or signal in both time and frequency or scale simultaneously. The concept of multiresolution is developed by Mallat (1989a, 1989b) and Meyer (1992), where the signal decomposed in terms of resolution of detail has proved to be a powerful and flexible tool in digital signal processing. Wavelet analysis is covered in many excellent texts, including Chui (1992), Burrus et al. (1998), Resnikoff and Wells (1998) and Louis et al. (1998).

A square integrable function $\psi(t) \in L^2(\mathbb{R})$ with its Fourier transform $\Psi(\omega)$ satisfying the admission condition:

$$0 \; < \; c_\psi := \; 2\,\pi \int\limits_{\mathbb{R}} \frac{|\Psi(\omega)|^2}{|\omega|}\, d\omega \; < \; \infty \tag{4.1}$$

is called a wavelet. It implies that the Fourier transform vanishes at zero

frequency and that the time-average of the wavelet $\psi(t)$ is zero:

$$0 \;=\; \Psi(0) \;=\; \frac{1}{\sqrt{2\pi}} \int\limits_{\mathbb{R}} \psi(t)\, dt. \tag{4.2}$$

For this reason the function $\psi(t)$ describes an oscillation with a band-pass-like spectrum and is named *wavelet*. The continuous wavelet transform (CWT) maps the one-dimensional function $f(t)$ into a two-dimensional representation $L_\psi(a, b)$ in the time-frequency or time-scale plane:

$$L_\psi(a,b) \;=\; \frac{1}{\sqrt{c_\psi}} \frac{1}{\sqrt{|a|}} \int\limits_{\mathbb{R}} f(t)\, \psi\Big(\frac{t-b}{a}\Big)\, dt \tag{4.3}$$

with $a \in \mathbb{R}\backslash\{0\}, b \in \mathbb{R}$. The parameter b translates the wavelet to focus on local information of f around $t = b$, and parameter a controls the sphere of influence of the wavelet. The inverse wavelet transform is given by:

$$f(t) \;=\; \int\limits_{\mathbb{R}} \int\limits_{\mathbb{R}} \frac{1}{\sqrt{c_\psi}} \frac{1}{\sqrt{|a|}}\, L_\psi(a,b)\, \psi\Big(\frac{t-b}{a}\Big)\, \frac{da\, db}{a^2}. \tag{4.4}$$

Additional conditions are imposed on the wavelet functions to make the wavelet transform decrease quickly with decreasing frequency. A wavelet of order $N \in \mathbb{N}$ has $N - 1$ vanishing moments:

$$\int\limits_{\mathbb{R}} t^k\, \psi(t)\, dt \;=\; 0, \qquad 0 \le k \le N-1 \tag{4.5}$$

where the N^{th} moment is finite and non zero:

$$\int\limits_{\mathbb{R}} t^N\, \psi(t)\, dt \;\neq\; 0. \tag{4.6}$$

It can be shown that the wavelet transform based on a wavelet of order N approximates function derivatives of the same order $f^{(N)}(t)$.

Note that the location of the signal $f(t)$ in the time-frequency plane is to some extent uncertain; this is expressed by the Heisenberg uncertainty relation:

$$\int\limits_{\mathbb{R}} (t-t_0)^2\, |f(t)|^2\, dt \int\limits_{\mathbb{R}} (\omega-\omega_0)^2\, |F(\omega)|^2\, d\omega \;\ge\; \frac{1}{4} \tag{4.7}$$

with $t_0, \omega_0 \in \mathbb{R}$ and $F(\omega)$ denoting the Fourier transform of $f(t)$.

The concept of multiresolution analysis and the discrete wavelet transform play a vital role in this study and are described in detail in the next two sections.

4.2 Multiresolution Analysis

The multiresolution formulation is designed to decompose signals in low and high frequency components to extract information on different resolution scales. The basic concept of multiresolution analysis (MRA) was developed by Mallat (1989a, 1989b) and Meyer (1992).

A *scaling function* $\varphi(t) \in \mathrm{L}^2(\mathbb{R})$ is introduced, which spans the subspace $V_0 \subset L^2(\mathbb{R})$ by its integer translates:

$$V_0 \;=\; \overline{\operatorname{span}\{\varphi(t-k) \,|\, k \in \mathbb{Z}\}}. \tag{4.8}$$

The over-bar denotes closure. The basic requirement of multiresolution analysis is a nesting of the spanned spaces $V_m \subset L^2(\mathbb{R})$ as:

$$\{0\} \subset \cdots \subset V_2 \subset V_1 \subset V_0 \subset V_{-1} \subset V_{-2} \subset \cdots \subset L^2(\mathbb{R})$$

with:

$$\overline{\bigcup_{m\,\in\,\mathbb{Z}} V_m} \quad = \quad L^2(\mathbb{R}), \tag{4.9}$$

$$\bigcap_{m\,\in\,\mathbb{Z}} V_m \quad = \quad \{0\}, \tag{4.10}$$

$$f(t) \in V_m \quad \Longleftrightarrow \quad f(2^m\,t) \in V_0. \tag{4.11}$$

The size of the subspace spanned can be increased by changing the time scale of the scaling function. A two-dimensional function set is generated from the basic scaling function by scaling and translation:

$$\left\{\varphi_{m,k}(t) \;=\; 2^{-m/2}\,\varphi(2^{-m}\,t-k) \mid m,k \in \mathbb{Z}\right\} \tag{4.12}$$

with the subspace V_m being defined as:

$$V_m \;=\; \overline{\operatorname{span}\{\varphi_{m,k} \,|\, k \in \mathbb{Z}\}}. \tag{4.13}$$

Fundamental to the theory of the scaling functions is the recursive dilation equation:

$$\varphi(t) \;=\; \sqrt{2}\,\sum_{k\,\in\,\mathbb{Z}} h_k\,\varphi(2\,t-k) \tag{4.14}$$

allowing the generation of orthogonal wavelet basis systems and the implementation of fast algorithms. It can be shown that the wavelet $\psi \in V_{-1}$ can be expressed in terms of the scaling function $\varphi \in V_0$:

$$\psi(t) \;=\; \sqrt{2}\,\sum_{k\,\in\,\mathbb{Z}} g_k\,\varphi(2\,t-k) \tag{4.15}$$

$$g_k \;=\; (-1)^k\,h_{1-k} \tag{4.16}$$

where h_k are the scaling function coefficients.

4.3 Discrete Wavelet Transform

The discrete wavelet transform (DWT) is based on the concept of multiresolution analysis, which enables the implementation of efficient decomposition algorithms. A function $f(t) \in V_0$ can be expressed in terms of integer translates of the scaling function $\varphi(t)$ by:

$$f(t) = \sum_{k \in \mathbb{Z}} c_k^0 \, \varphi(t-k) \tag{4.17}$$

$$c^0 = \{c_k^0 \,|\, k \in \mathbb{Z}\} \tag{4.18}$$

where c^0 are real expansion coefficients. The important features of function $f(t)$ can be better described by using a set of wavelet functions $\psi_{m,k}(t)$:

$$\left\{\psi_{m,k}(t) = 2^{-m/2}\, \psi(2^{-m}\, t - k) \mid m, k \in \mathbb{Z}\right\} \tag{4.19}$$

which span the differences between the spaces spanned by the set of scaling functions $\varphi_{m,k}(t)$ defined in Eq. (4.12). This family of wavelet functions defines an orthonormal basis of $L^2(\mathbb{R})$.

The coefficients of the discrete wavelet transform L_ψ are calculated from the scalar products of the function f and the wavelets $\psi_{m,k}$:

$$\sqrt{c_\psi}\, L_\psi(2^m, 2^m k) = \langle f, \psi_{m,k} \rangle, \quad m \in \mathbb{N}_0, k \in \mathbb{Z} \tag{4.20}$$

which can also be written in terms of the scaling functions using Eqs. (4.14) and (4.15) as:

$$c_k^m = \langle f, \varphi_{m,k} \rangle = \sum_{n \in \mathbb{Z}} h_n \, \langle f, \varphi_{m-1,2k+n} \rangle = \sum_{l \in \mathbb{Z}} h_{l-2k}\, c_l^{m-1} \tag{4.21}$$

$$d_k^m = \langle f, \psi_{m,k} \rangle = \sum_{n \in \mathbb{Z}} g_n \, \langle f, \varphi_{m-1,2k+n} \rangle = \sum_{l \in \mathbb{Z}} g_{l-2k}\, c_l^{m-1} \tag{4.22}$$

with $l = 2k+n$. Starting with c_0, the scaling and wavelet coefficients c^m and d^m are recursively obtained by convolving the expansion coefficients at scale $m-1$ with the time-reversed lowpass and highpass filter coefficients h_{l-2k} and g_{l-2k} and then down-sampling by a factor of two. The symbol $*_2$ is used to indicate this procedure. By introducing the reduction operators $\mathcal{H}$ and $\mathcal{G}$:

$$\mathcal{H}c = c *_2 h_* = \left\{(\mathcal{H}c)_k = \sum_{l \in \mathbb{Z}} h_{l-2k}\, c_l\right\} \tag{4.23}$$

$$\mathcal{G}c = c *_2 g_* = \left\{(\mathcal{G}c)_k = \sum_{l \in \mathbb{Z}} g_{l-2k}\, c_l\right\} \tag{4.24}$$

the scheme of calculating a M-scale discrete wavelet transform can be illustrated as follows (Louis et al., 1998):

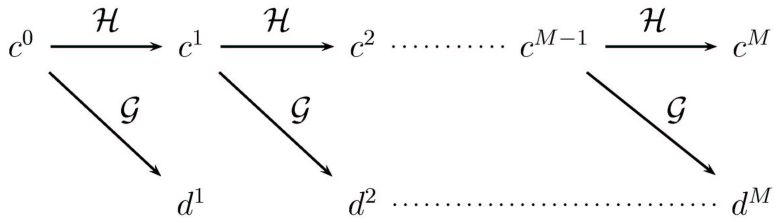

with $c^m = \mathcal{H}c^{m-1}$ and $d^m = \mathcal{G}c^{m-1}$ for $m = 1, 2, \ldots, M$, each being half the length of c^{m-1}. The original expansion coefficients c^0 are reconstructed by the inverse algorithm:

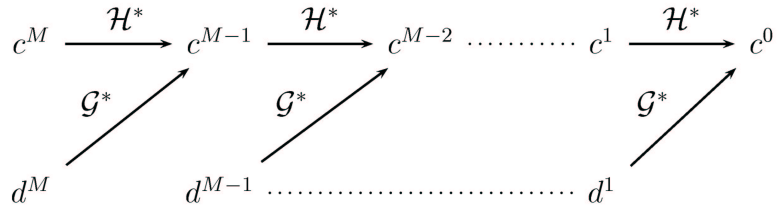

with $c^{m-1} = \mathcal{H}^* c^m + \mathcal{G}^* d^m$ and the inverse operators $\mathcal{H}^*$ and $\mathcal{G}^*$:

$$\mathcal{H}^* c \;=\; \Big\{ (\mathcal{H}^* c)_k \;=\; \sum_{l \in \mathbb{Z}} h_{k-2l}\, c_l \Big\}, \tag{4.25}$$

$$\mathcal{G}^* c \;=\; \Big\{ (\mathcal{G}^* c)_k \;=\; \sum_{l \in \mathbb{Z}} g_{k-2l}\, c_l \Big\}. \tag{4.26}$$

In this work, least-asymmetric wavelets called *symlets* are used, which are developed by Daubechies (1988, 1993) . The lowpass and highpass analysis and synthesis filters with 16 coefficients and the associated scaling and wavelet function are presented in Fig. 4.1. Note the band-pass structure of the wavelet Fourier spectrum. Time scaling of the wavelet function corresponds to stretching and shifting of the Fourier spectrum:

$$\psi(at) \iff \frac{1}{|a|}\, \Psi\Big(\frac{\omega}{a}\Big) \tag{4.27}$$

with $a \in \mathbb{R}\backslash\{0\}$. Hence the finite spectrum of the signal to be analyzed will be covered by a sum of stretched wavelet spectra that are touching each other, together with the spectrum of scaling function at the largest scale coding the remaining low frequency characteristics. Fig. 4.2 illustrates the decomposition procedure of the 3-scale discrete wavelet transform using *symlets* shown in Fig. 4.1. It can be observed that most information of the signal is captured in the third level approximation coefficients c^3 and detail coefficients d^3. This sparse representation is a typical feature of the discrete wavelet transform and is largely utilized in data compression.

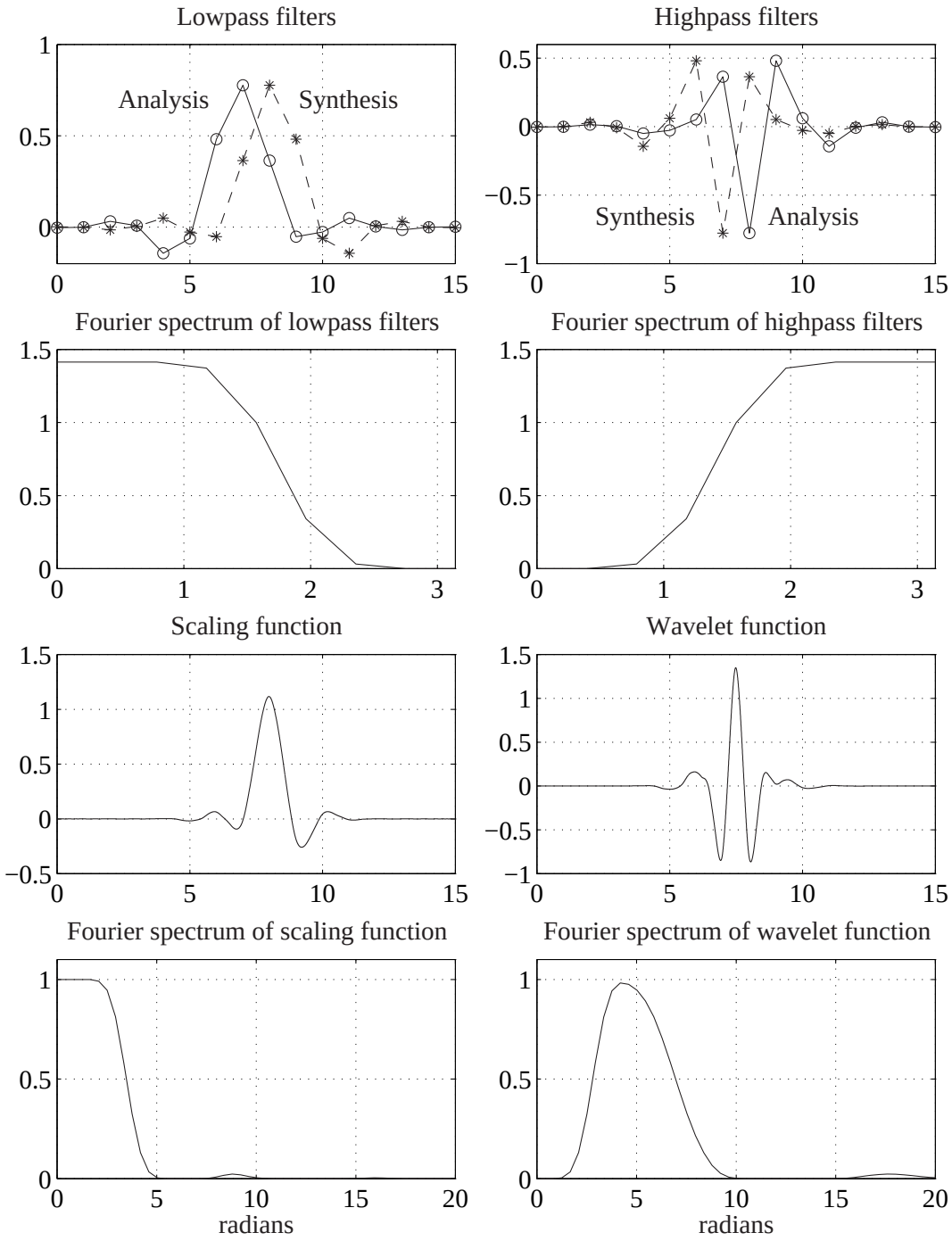

Figure 4.1: *Symlets* analysis and synthesis lowpass and highpass filters with associated scaling and wavelet function.

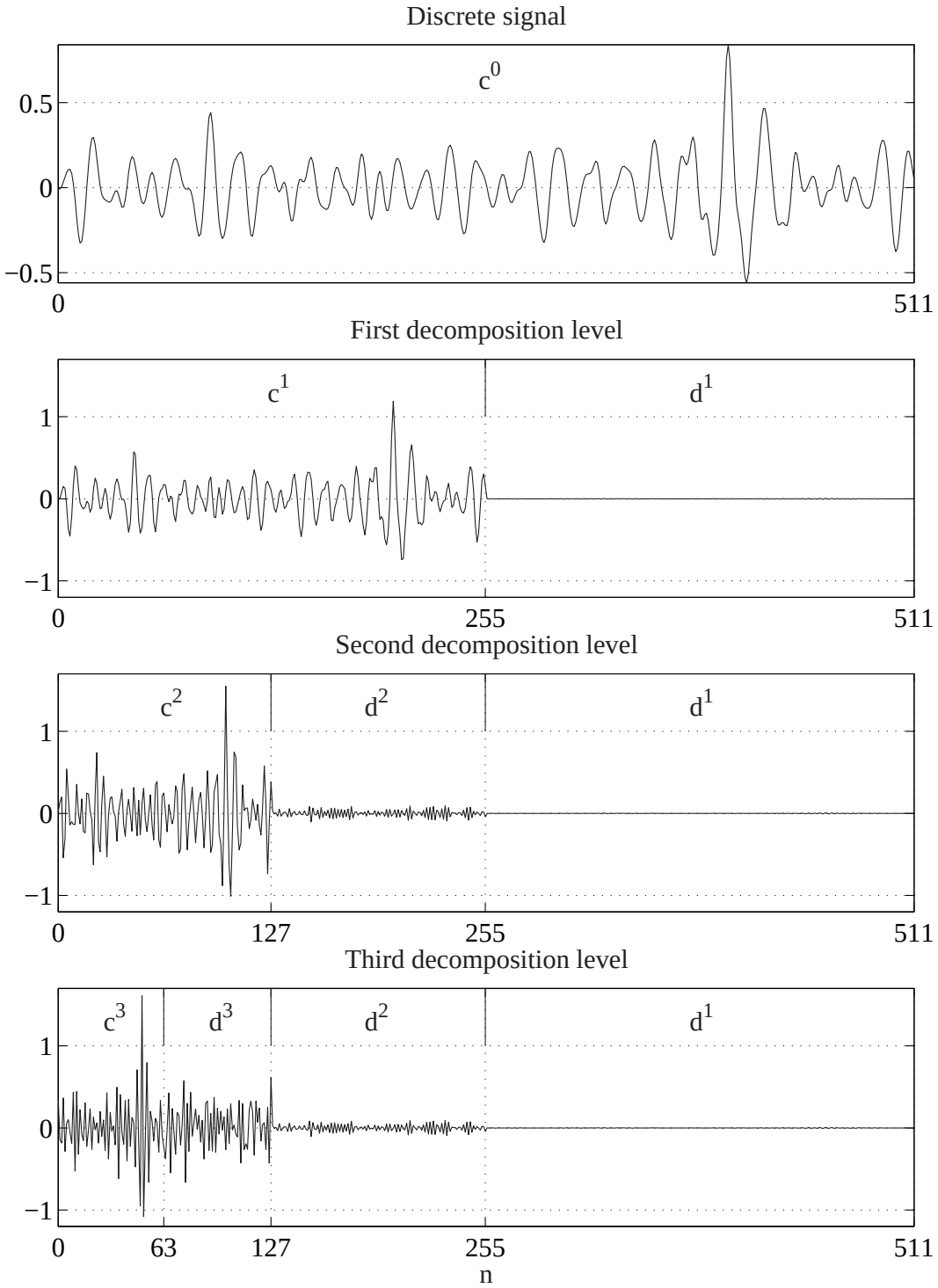

Figure 4.2: Decomposition levels of the 3-scale discrete wavelet transfom using *symlets*.

Chapter 5

Synthesizing Transient Waves in Random Seas

5.1 Introduction

The general procedure for synthesizing transient waves and wave groups in a random sea is outlined in Fig. 5.1. At first, the target wave train needs to be defined by global parameters as the water depth and variance spectrum in terms of significant wave height and peak period. In addition, local characteristics of the wave pattern and extreme waves are of great interest. They are defined in terms of wave and crest height as well as period of individual waves of a particular wave sequence.

A first approximation of the desired wave train is based on linear wave theory and determined by an optimization technique. In linear wave theory the wave train can be regarded as the superposition of independent harmonic waves with particular amplitude, frequency and phase. For a given design variance spectrum the phase spectrum is responsible for all local wave characteristics. For this reason, an initially random phase spectrum is modified by the sequential quadratic programming (SQP) method to generate the desired wave train. The associated optimization problem is stated, in a general form, as:

$$\underset{\boldsymbol{\beta} \in \Re^n}{\text{minimize}} \;\; f(\boldsymbol{\beta}) \;=\; \sum_{k=1}^{K/2} \left(d_k^1\right)^2 + \sum_{k=1}^{K/4} \left(d_k^2\right)^2 + \;\ldots\; + \sum_{k=1}^{K/2^M} \left(d_k^M\right)^2 \;=$$

$$\sum_{k=1}^{K/2} \langle x_B(t), \psi(t)_{1,k} \rangle^2 + \sum_{k=1}^{K/4} \langle x_B(t), \psi(t)_{2,k} \rangle^2 + \;\ldots\; + \sum_{k=1}^{K/2^M} \langle x_B(t), \psi(t)_{M,k} \rangle^2 \tag{5.1}$$

$$
\begin{aligned}
\text{subject to} \qquad g_j &= \Upsilon_j - \Upsilon_{j,\,target} \;=\; 0, \quad j = 1, \ldots, m_e \\
g_{m_e+1} &= \max\Big\{|x_B(t)|\Big\} - x_{max} \;\leq\; 0, \\
g_{m_e+2} &= \max\Big\{|\dot{x}_B(t)|\Big\} - u_{max} \;\leq\; 0, \\
g_{m_e+3} &= \max\Big\{|\ddot{x}_B(t)|\Big\} - a_{max} \;\leq\; 0, \\
g_{m_e+3+j} &= -\pi - \beta_j \;\leq\; 0, \quad j = 1, \ldots, n \\
g_{m_e+3+n+j} &= -\pi + \beta_j \;\leq\; 0, \quad j = 1, \ldots, n
\end{aligned}
\tag{5.2}
$$

where $\boldsymbol{\beta}$ is the vector of the free variables, which are the initially random phase values. K is the number of data points describing the wave board motion $x_B(t)$, and M is the decomposition level of the discrete wavelet transform. Minimizing the objective function $f(\boldsymbol{\beta})$ improves the representation of the wave board motion $x_B(t)$ in terms of wavelet coefficients, which are reduced in the higher frequency range. This compression is useful in the subsequent fitting procedure of the nonlinear wave train with the subplex method developed by Rowan (1990). The calculation of the discrete wavelet transform is described in detail in Chapter 4.3. All local target wave characteristics $\Upsilon_{j,\,target}$ are expressed as equality constraints which actually force the SQP method to converge to the desired solution. The maximum stroke x_{max}, velocity u_{max} and acceleration a_{max} of the wave board motion define inequality constraints to be taken into consideration.

The motion of the wave board is determined from the solution and used to derive boundary conditions for the subsequent numerical simulation of the nonlinear wave evolution in time domain with the finite element method. If necessary, the degree of conformity of the nonlinear wave train with the target characteristics is further improved by applying another minimization technique to the nonlinear fee surface flow problem. The SQP method cannot be used in this case, since possible wave breaking is associated with infeasible parameter sets resulting in noisy objective functions where the gradient is difficult to be calculated. Hence the subplex method for unconstrained minimization is selected, since it requires only function evaluations, not derivatives. The objective function and the constraints are restated as:

$$
\underset{\boldsymbol{c}\,\in\,\Re^m}{\text{minimize}} \;\; f(\boldsymbol{c}) \;=\; \sum_{j}^{m_e} \left(\frac{\Upsilon_j - \Upsilon_{j,\,target}}{\Upsilon_{j,\,target}} \right)^2 + \left(\frac{\sigma\big(x_B(t)\big) - \sigma\big(x_B(t)_{initial}\big)}{\sigma\big(x_B(t)_{initial}\big)} \right)^2
\tag{5.3}
$$

$$\begin{aligned} \text{subject to} \quad g_1 &= \max\Big\{|x_B(t)|\Big\} - x_{max} \;\leq\; 0, \\ g_2 &= \max\Big\{|\dot{x}_B(t)|\Big\} - u_{max} \;\leq\; 0, \\ g_3 &= \max\Big\{|\ddot{x}_B(t)|\Big\} - a_{max} \;\leq\; 0, \end{aligned} \tag{5.4}$$

where $\boldsymbol{c}$ is the vector of the free variables, which are a small number of selected approximation coefficients of the discrete wavelet transform. The standard deviation of the wave board motion $\sigma\big(x_B(t)\big)$ has been included to control the total energy input into the wave tank.

Fig. 5.2 shows the general procedure for fitting nonlinear wave trains to target characteristics using the Subplex method and discrete wavelet transform. The target wave characteristics are usually the same as those defined in the preceding SQP optimization, which produced a qualified initial guess of the wave board motion. The discrete wavelet transform of this wave board motion is calculated, and the free variables in terms of wavelet coefficients are selected. This particular set of wavelet coefficients corresponds to a certain resolution scale and time range, which is responsible for the evolution of the target wave sequence in the random sea. It allows us to considerably reduce the number of free variables in the fitting problem and the associated computational costs. In each iteration, the wave board motion is determined by calculating the inverse discrete wavelet transform, and then checked for its permissibility. Either a new set of wavelet coefficients is determined or the nonlinear free surface evolution is numerically simulated in time domain with the finite element method. The value of the objective function and the constraints are determined, and a new set of wavelet coefficients is calculated by the subplex method until the desired termination criteria are reached. In case of wave breaking, a high value is assigned to the objective function indicating an infeasible parameter set.

General introductions to nonlinear programming for solving constrained optimization problems are widely available (Fletcher, 1980; Bazaraa et al., 1993; Nash and Sofer, 1996). The sequential quadratic programming method and the subplex method are described in Sections 5.2 and 5.3. Due to the multi-modal nature of the minimization problems, both methods may only converge to local minima which depend on the initial conditions. This is, in general, not a disadvantage, since the random structure of the wave train is a desired feature. Further details of the entire procedure are illustrated in the next chapter for a single wave and wave group synthesized in a random sea.

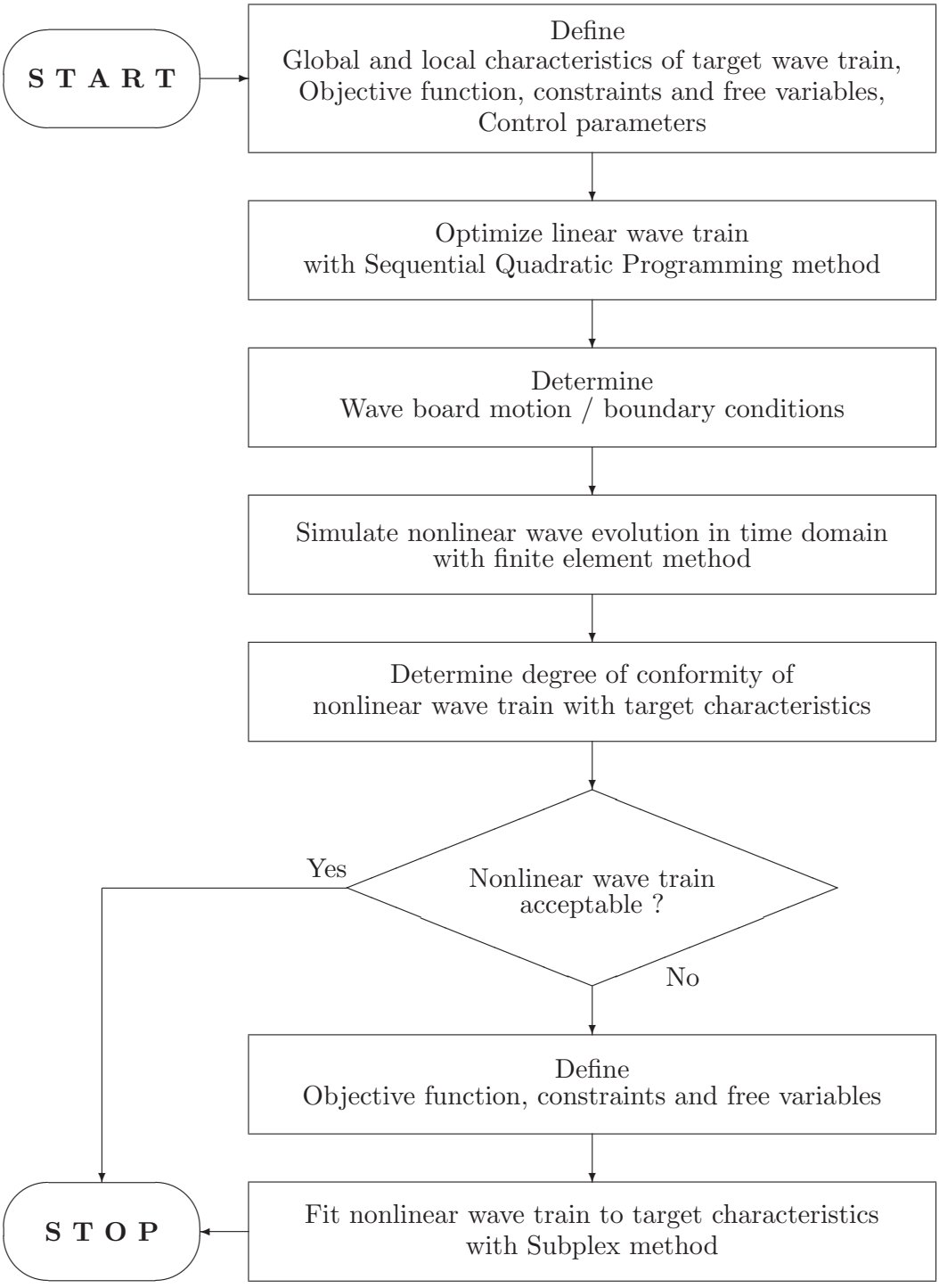

Figure 5.1: General procedure for synthesizing transient waves and wave groups in random seas.

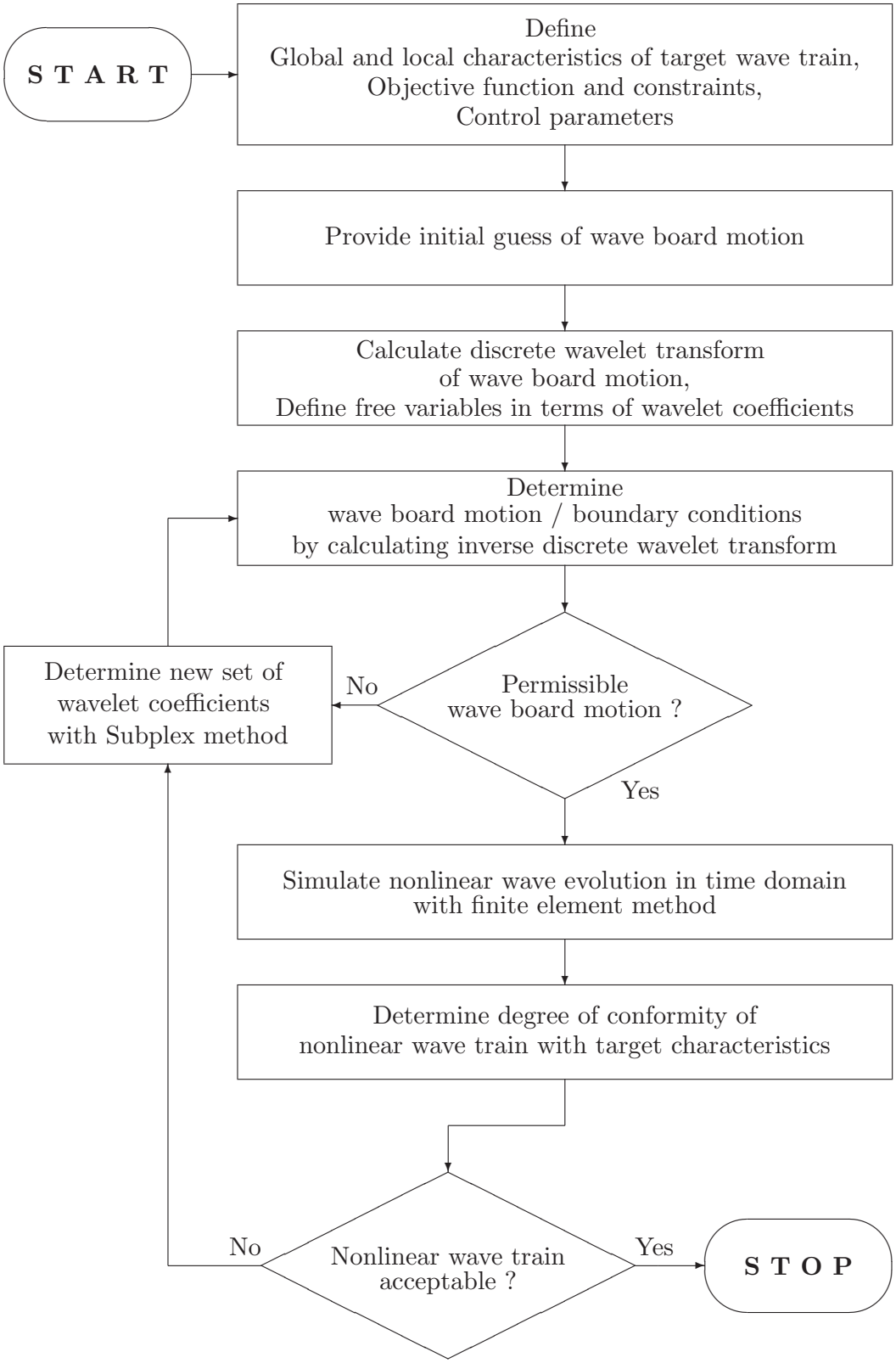

Figure 5.2: General procedure for fitting nonlinear wave trains to target characteristics using Subplex method and discrete wavelet transform.

5.2 Sequential Quadratic Programming

Sequential quadratic programming (SQP) is a popular and successful technique for solving optimization problems with nonlinear constraints. The main idea is to transform the problem into an easier subproblem with a quadratic objective function and linear constraints that can be solved and used as the basis of an iterative process. This approach is a generalization of the Newton method for unconstrained minimization. The SQP method concept based on the Lagrangian function was first used by Wilson (1963). Quasi-Newton approximations to the Hessian matrix of the Lagrangian function have been suggested by Han (1976) and Powell (1978) and are widely used in nonlinear optimization methods. An overview of SQP is found in Fletcher (1980), Bazaraa et al. (1993), and Nash and Sofer (1996).

A general optimization problem with equality and inequality constraints is stated as:

$$\underset{\boldsymbol{x}\in\mathbb{R}^n}{\text{minimize}} \;\; f(\boldsymbol{x}) \tag{5.5}$$

$$\begin{aligned} \text{subject to} \quad & g_i(\boldsymbol{x}) \;=\; 0, \quad i = 1,\ldots,m_e \\ & g_i(\boldsymbol{x}) \;\le\; 0, \quad i = m_e+1,\ldots,m \\ & \boldsymbol{x}_l \;\le\; \boldsymbol{x} \;\le\; \boldsymbol{x}_u \end{aligned}$$

where $\boldsymbol{x}$ is the vector of the design parameters, $f(\boldsymbol{x})$ is the objective function to be minimized and $\boldsymbol{g}(\boldsymbol{x})$ is the vector of the equality and inequality constraints. The lower and upper parameter bounds are $\boldsymbol{x}_l$ and $\boldsymbol{x}_u$. The objective and constraint functions are assumed to be twice differentiable. Many modern optimization methods including SQP introduce the *Lagrangian function*:

$$\mathcal{L}(\boldsymbol{x},\boldsymbol{\lambda}) \;=\; f(\boldsymbol{x}) \;+\; \sum_{i=1}^{m} \lambda_i \, g_i(\boldsymbol{x}) \tag{5.6}$$

where λ_i are the Lagrangian multipliers that indicate the sensitivity of the optimal objective value to variations in the constraint functions. Here the bound constraints are expressed as inequality constraints. The Lagrangian function can be approximated by the second order Taylor series expansion near the point $(\boldsymbol{x}_k, \boldsymbol{\lambda}_k)$:

$$\mathcal{L}(\boldsymbol{x},\boldsymbol{\lambda}) \;=\; \mathcal{L}(\boldsymbol{x}_k,\boldsymbol{\lambda}_k) + \begin{pmatrix}\boldsymbol{p}_k\\ \boldsymbol{\nu}_k\end{pmatrix}^T \nabla\mathcal{L}(\boldsymbol{x}_k,\boldsymbol{\lambda}_k) + \frac{1}{2}\begin{pmatrix}\boldsymbol{p}_k\\ \boldsymbol{\nu}_k\end{pmatrix}^T \nabla^2\mathcal{L}(\boldsymbol{x}_k,\boldsymbol{\lambda}_k)\begin{pmatrix}\boldsymbol{p}_k\\ \boldsymbol{\nu}_k\end{pmatrix}$$

where $\nabla^2\mathcal{L}(\boldsymbol{x}_k,\boldsymbol{\lambda}_k)$ is the Hessian matrix of the Lagrangian function and

$$\begin{pmatrix}\boldsymbol{p}_k\\ \boldsymbol{\nu}_k\end{pmatrix} \;=\; \begin{pmatrix}\boldsymbol{x}\\ \boldsymbol{\lambda}\end{pmatrix} \;-\; \begin{pmatrix}\boldsymbol{x}_k\\ \boldsymbol{\lambda}_k\end{pmatrix}.$$

Applying Newton's method to the first order necessary condition for a local minimizer $(\boldsymbol{x}^*, \boldsymbol{\lambda}^*)$ of the Lagrangian function:

$$\nabla \mathcal{L}(\boldsymbol{x}^*, \boldsymbol{\lambda}^*) \;=\; \nabla \mathcal{L}(\boldsymbol{x}_k, \boldsymbol{\lambda}_k) + \nabla^2 \mathcal{L}(\boldsymbol{x}_k, \boldsymbol{\lambda}_k) \begin{pmatrix} \boldsymbol{p}_k \\ \boldsymbol{\nu}_k \end{pmatrix} \;=\; 0$$

which corresponds to solving the Karush-Kuhn-Tucker equations for the general problem with nonlinear constraints:

$$\begin{aligned} \nabla_x \mathcal{L}(\boldsymbol{x}^*, \boldsymbol{\lambda}^*) \;&=\; \nabla f(\boldsymbol{x}^*) + \sum_{i=1}^{m} \lambda_i^* \nabla g_i(\boldsymbol{x}^*) \;=\; 0 \\ \lambda_i^* \, g_i(\boldsymbol{x}^*) \;&=\; 0, \quad i = m_e + 1, \ldots, m \\ \lambda_i^* \;&\geq\; 0, \quad i = m_e + 1, \ldots, m \end{aligned} \tag{5.7}$$

yields a linear system for the descent search directions $(\boldsymbol{p}_k, \boldsymbol{\nu}_k)$:

$$\begin{pmatrix} \nabla^2_{xx} \mathcal{L}(\boldsymbol{x}_k, \boldsymbol{\lambda}_k) & \nabla \boldsymbol{g}(\boldsymbol{x}_k) \\ \nabla \boldsymbol{g}(\boldsymbol{x}_k)^T & 0 \end{pmatrix} \begin{pmatrix} \boldsymbol{p}_k \\ \boldsymbol{\nu}_k \end{pmatrix} \;=\; - \begin{pmatrix} \nabla_x \mathcal{L}(\boldsymbol{x}_k, \boldsymbol{\lambda}_k) \\ \boldsymbol{g}(\boldsymbol{x}_k) \end{pmatrix}. \tag{5.8}$$

In a quasi-Newton approach the Hessian $\nabla^2_{xx} \mathcal{L}(\boldsymbol{x}_k, \boldsymbol{\lambda}_k)$ is approximated by another matrix $\boldsymbol{H}_k$ that can be found using first derivative information only. Hence the search direction can be computed by fewer operations leading to efficient numerical algorithms. The system of equations stated in Eq. (5.8) represents the first order optimality conditions for the quadratic subproblem with linear constraints:

$$\underset{\boldsymbol{p} \in \Re^n}{\text{minimize}} \;\; \frac{1}{2} \boldsymbol{p}^T \boldsymbol{H}_k \, \boldsymbol{p} \;+\; \boldsymbol{p}^T \nabla_x \mathcal{L}(\boldsymbol{x}_k, \boldsymbol{\lambda}_k) \tag{5.9}$$

$$\begin{aligned} \text{subject to} \quad & \nabla g_i(\boldsymbol{x_k})^T \boldsymbol{p} \;+\; g_i(\boldsymbol{x_k}) \;=\; 0, \quad i = 1, \ldots, m_e \\ & \nabla g_i(\boldsymbol{x_k})^T \boldsymbol{p} \;+\; g_i(\boldsymbol{x_k}) \;\leq\; 0, \quad i = m_e + 1, \ldots, m. \end{aligned}$$

The solution is used to form a new iterate:

$$\begin{pmatrix} \boldsymbol{x}_{k+1} \\ \boldsymbol{\lambda}_{k+1} \end{pmatrix} \;=\; \begin{pmatrix} \boldsymbol{x}_k \\ \boldsymbol{\lambda}_k \end{pmatrix} \;+\; \alpha_k \begin{pmatrix} \boldsymbol{p}_k \\ \boldsymbol{\nu}_k \end{pmatrix}.$$

The step length parameter α_k is determined by a line search procedure so that a sufficient decrease in a *merit function* is achieved, which provides a measure of the optimization progress. This auxiliary function is a sum of terms that include the objective function and the amount of infeasibility of the constraints. The value of the merit function will decrease if the new

solution point reduces the objective function and the infeasibility. In this work the merit function defined by Han (1975) and Powell (1978) is used:

$$\mathcal{M}(\boldsymbol{x}) \;=\; f(\boldsymbol{x}) \;+\; \sum_{i=1}^{m_e} r_i\, g_i(\boldsymbol{x}) \;+\; \sum_{i=m_e+1}^{m} r_i \max\Big\{0, g_i(\boldsymbol{x})\Big\}. \tag{5.10}$$

Powell recommends setting the penalty parameter r_i to be:

$$r_i \;=\; (r_{k+1})_i \;=\; \max_i\left\{\lambda_i,\; \frac{1}{2}\Big((r_k)_i \;+\; \lambda_i\Big)\right\}, \quad i = 1, \ldots, m \tag{5.11}$$

which allows us to take positive contributions from constraints into account that are inactive at the solution but were recently active. Initially the penalty parameter is set to:

$$(r_i)_{start} \;=\; \frac{\| \nabla f(\boldsymbol{x}) \|}{\| \nabla g_i(\boldsymbol{x}) \|}$$

where $\| \cdot \|$ represents the Euclidean norm. The Hessian matrix is updated for the next iteration by applying the Broyden-Fletcher-Goldfarb-Shanno (BFGS) formula, which is considered to be most effective:

$$\begin{aligned} \boldsymbol{H}_{k+1} &= \boldsymbol{H}_k \;-\; \frac{(\boldsymbol{H}_k \boldsymbol{s}_k)(\boldsymbol{H}_k \boldsymbol{s}_k)^T}{\boldsymbol{s}_k^T \boldsymbol{H}_k \boldsymbol{s}_k} \;+\; \frac{\boldsymbol{q}_k \boldsymbol{q}_k^T}{\boldsymbol{q}_k^T \boldsymbol{s}_k} \\ \boldsymbol{s}_k &= \boldsymbol{x}_{k+1} \;-\; \boldsymbol{x}_k \\ \boldsymbol{q}_k &= \nabla f(\boldsymbol{x}_{k+1}) + \boldsymbol{\lambda}_{k+1}^T \boldsymbol{\nabla g}(\boldsymbol{x}_{k+1}) \;-\; \Big(\nabla f(\boldsymbol{x}_k) + \boldsymbol{\lambda}_k^T \boldsymbol{\nabla g}(\boldsymbol{x}_k)\Big). \end{aligned} \tag{5.12}$$

It can be shown that the approximation of the Hessian matrix $\boldsymbol{H}_k$ is maintained positive definite by providing $\boldsymbol{q}_k^T \boldsymbol{s}_k > 0$.

5.3 Subplex Method

The subplex method was developed by Rowan (1990) and is a generalization of the popular Nelder-Mead simplex (NMS) method (1965) for unconstrained minimization, which requires only function evaluations, not derivatives. A high dimensional problem is decomposed into low dimensional subspaces which are easily handled by NMS. The subplex method retains the advantages of NMS on noisy functions and is able to handle constraints by rejection of infeasible points, since a permanent collapse into a subspace is avoided by automatic restarts. This feature is especially important for optimizing steep nonlinear waves which might become unstable. In the case of breaking, the numerical simulation based on potential flow theory will stop,

and no function value can be determined. Hence, the associated parameter set is infeasible and a high value is assigned to the objective function.

The downhill *simplex method* due to Nelder and Mead (1965)is a function comparison method for unconstrained optimization. A simplex is a convex hull of $n+1$ vertices and moves through the n-dimensional domain space of the objective function. During the minimization the simplex changes shape and size, and shrinks automatically when enveloping a minimum.

The initial simplex is defined by a starting point $\boldsymbol{x}_0$ and by setting the remaining vertices to:

$$\boldsymbol{x}_i \;=\; \boldsymbol{x}_0 \;+\; \mu_i\, \boldsymbol{e}_i, \qquad i = 1, 2, \ldots, n \tag{5.13}$$

where μ_i are the characteristic length scales of the problem. $\boldsymbol{e}_i$ are the unit vectors of the domain space. Fig. 5.3 illustrates the basic steps taken by the NMS method for the case $n = 2$. Reflection corresponds to moving the point $\boldsymbol{x}_h$ of the simplex where the objective function is largest through the center of the remaining points. If this point $\boldsymbol{x}_r$ is the best in the new simplex then an expansion of this vertex in the same direction is tried, yielding $\boldsymbol{x}_e$. The reflected point $\boldsymbol{x}_r$ replaces $\boldsymbol{x}_h$ if $\boldsymbol{x}_r$ is neither the best nor the worst point of the new simplex. If the reflected point $\boldsymbol{x}_r$ is the worst point then $\boldsymbol{x}_r$ or $\boldsymbol{x}_h$ will be discarded depending on the function value. The simplex is then contracted to look for an intermediate lower point denoted by $\boldsymbol{x}_c$ or $\boldsymbol{x}_c^*$. If this operation still generates the worst point of the new simplex then both $\boldsymbol{x}_h$ and $\boldsymbol{x}_s$ are contracted simultaneously; this is called massive contraction or shrinkage. The choice of the four NMS parameters define the solution strategy and are usually set to $\alpha_s = 1$, $\beta_s = 0.5$, $\gamma_s = 2$ and $\delta_s = 0.5$.

The NMS method is well suited for minimizing noisy functions with low dimensional domain space, e.g. $n \leq 5$. The performance of the method decreases rapidly when n becomes much larger (Box, 1966). Another shortcoming is that NMS cannot handle constraints by rejecting infeasible points, since a simplex may collapse into a subspace (Rowan, 1990).

The *subplex method* retains the positive features of the simplex method regarding noisy functions. The inefficiency of NMS at high dimensional problems is removed by decomposing the problem into low dimensional subspaces that can easily be handled by NMS. The subplex method generalizes methods that determine, at each iteration, an improved set of search directions and perform line searches along those directions.

The n-dimensional domain space of the objective function is decomposed in n_s mutually orthogonal subspaces n_{si}:

$$\sum_{i=1}^{n_s} n_{si} \;=\; n, \qquad n_{smin} \leq n_{si} \leq n_{smax} \tag{5.14}$$

with the direction of progress lying approximately in the first subspace. The minimum and maximum subspace dimensions are defined by n_{smin} and n_{smax} with:

$$1 \le n_{smin} \le n_{smax} \le n \quad \text{and} \quad n_{smin}\lceil n/n_{smax}\rceil \le n. \tag{5.15}$$

The number of subspaces and the subspace dimensions control which, and how many, components of the design parameters $\boldsymbol{x}$ are selected for the inner minimization by the simplex method. To determine the subspaces the vector of progress $\Delta\boldsymbol{x} = (\Delta x_1, \ldots, \Delta x_n)^T$, which measures the difference of successive iterates, is sorted by decreasing magnitude. This new vector is denoted by $\widetilde{\Delta\boldsymbol{x}} = (\widetilde{\Delta x}_1, \ldots, \widetilde{\Delta x}_n)^T$ with $|\widetilde{\Delta x}_i| \ge |\widetilde{\Delta x}_{i+1}|$ for $i = 1, \ldots, n-1$. The first subspace dimension n_{s1} is the value m that maximizes the function:

$$\mathcal{F}(m) \;=\; \begin{cases} \dfrac{\|\widetilde{\Delta\boldsymbol{x}}\|_1}{m} \;-\; \dfrac{\|\widetilde{\Delta\boldsymbol{x}}\|_1}{n-m}, & \text{for} \quad m < n \\[2ex] \dfrac{\|\widetilde{\Delta\boldsymbol{x}}\|_1}{n}, & \text{for} \quad m = n \end{cases} \tag{5.16}$$

subject to:

$$n_{smin} \le m \le n_{smax} \quad \text{and} \quad n_{smin}\lceil (n-m)/n_{smax}\rceil \le n-m \tag{5.17}$$

where $\|\cdot\|_1$ represents the 1-norm:

$$\|\boldsymbol{x}\|_1 \;=\; \sum_{i=1}^{n} |x_i|.$$

The inequalities (5.17) guarantee that the remaining vector $(\widetilde{\Delta x}_{m+1}, \ldots, \widetilde{\Delta x}_n)^T$ can be partitioned again to obtain the other subspaces n_{s2}, n_{s3}, ... in an iterative process.

At each iteration of the outer loop, the new vertices of the initial simplices for the inner NMS minimizations are determined by:

$$\boldsymbol{x}_i \;=\; \boldsymbol{x}_l \;+\; \mu_i\, \boldsymbol{e}_i, \qquad i = 1, 2, \ldots, n \tag{5.18}$$

where $\boldsymbol{x}_l$ is current best point and $\boldsymbol{\mu} = (\mu_1, \ldots, \mu_n)^T$ are the rescaled stepsizes of the previous iteration:

$$\boldsymbol{\mu} \;\longleftarrow\; \begin{cases} \min\Big\{\max\Big(\dfrac{\|\Delta\boldsymbol{x}\|_1}{\|\boldsymbol{\mu}\|_1},\, \omega_s\Big),\, \dfrac{1}{\omega_s}\Big\} \cdot \boldsymbol{\mu}, & \text{for} \quad n_s > 1 \\[2ex] \psi_s \cdot \boldsymbol{\mu}, & \text{for} \quad n_s = 1. \end{cases} \tag{5.19}$$

If more than one subspace exists, the degree of modifying the stepsize is controlled by the coefficient ω_s. Small values of ω_s force the subplex method to converge rapidly to a local minimum, whereas high values lead to a more thorough search, which may find another minimum with a lower function value. The coefficient ψ_s controls the accuracy of the subspace searches within the simplex method. The inner minimization terminates when the size of the simplex has been sufficiently reduced:

$$\mathrm{dist}(\boldsymbol{x}_l, \boldsymbol{x}_h)_{stop} \;\leq\; \psi_s \cdot \mathrm{dist}(\boldsymbol{x}_l, \boldsymbol{x}_h)_{start} \tag{5.20}$$

If only one subspace exists, the stepsize is set appropriately to resume minimization where it stopped in the previous iteration. The orientation of the initial simplices is determined from favorable directions in the vector of progress $\Delta\boldsymbol{x}$:

$$\mu_i \;\longleftarrow\; \begin{cases} \mathrm{sign}(\Delta x_i) \cdot |\mu_i|, & \text{for} \quad \Delta x_i \neq 0 \\ -\,\mu_i, & \text{for} \quad \Delta x_i = 0. \end{cases} \tag{5.21}$$

The subplex strategy is defined by the coefficients given in Table 5.1 where the first four parameters α_s, β_s, γ_s and δ_s are the same as those used in the NMS method. The termination test for the outer loop of the subplex method

Reflection	α_s	=	1	$(\alpha_s > 0)$
Contraction	β_s	=	0.5	$(0 < \beta_s < 1)$
Expansion	γ_s	=	2	$(\gamma_s > 1)$
Shrinkage	δ_s	=	0.5	$(0 < \delta_s < 1)$
Simplex reduction	ψ_s	=	0.25	$(0 < \psi_s < 1)$
Step reduction	ω_s	=	0.1	$(0 < \omega_s < 1)$
Minimum subspace dimension	n_{smin}	=	$\min(2, n)$	
Maximum subspace dimension	n_{smax}	=	$\min(5, n)$	

Table 5.1: Coefficients of the subplex strategy.

includes information on both $\Delta\boldsymbol{x}$ and $\boldsymbol{\mu}$:

$$\frac{\max\Big(\|\Delta\boldsymbol{x}\|_\infty,\; \psi_s \cdot \|\boldsymbol{\mu}\|_\infty\Big)}{\max\Big(\|\boldsymbol{x}\|_\infty, 1\Big)} \;\leq\; tol \tag{5.22}$$

since a small value of $\|\Delta\boldsymbol{x}\|_\infty$ may indicate that the stepsizes $\boldsymbol{\mu}$ are too large to achieve further progress. $\|\cdot\|_\infty$ represents the ∞-norm:

$$\|\boldsymbol{x}\|_\infty \;=\; \max_i\Big\{|x_i|\Big\}, \qquad i = 1, 2, \ldots, n.$$

Initial simplex

$$f(\boldsymbol{x}_h) > f(\boldsymbol{x}_s) > f(\boldsymbol{x}_l)$$

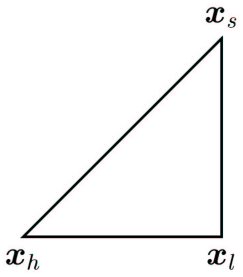

Reflection

$$\boldsymbol{x}_r = \boldsymbol{c} + \alpha_s (\boldsymbol{c} - \boldsymbol{x}_h)$$

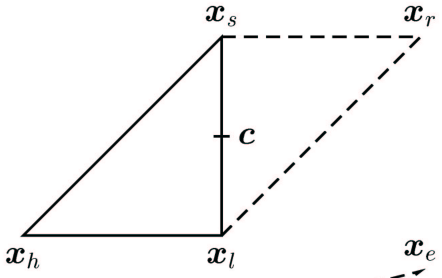

Expansion

$$\boldsymbol{x}_e = \boldsymbol{c} + \gamma_s (\boldsymbol{x}_r - \boldsymbol{c})$$

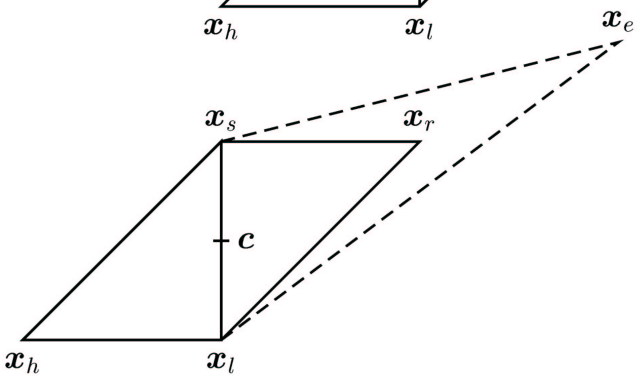

Contraction

$$f(\boldsymbol{x}_r) > f(\boldsymbol{x}_h): \ \boldsymbol{x}_c = \boldsymbol{c} + \beta_s (\boldsymbol{x}_h - \boldsymbol{c})$$

$$f(\boldsymbol{x}_r) \leq f(\boldsymbol{x}_h): \ \boldsymbol{x}_c^* = \boldsymbol{c} + \beta_s (\boldsymbol{x}_r - \boldsymbol{c})$$

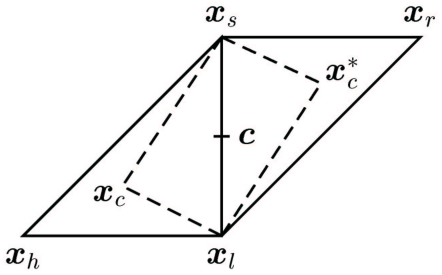

Shrinkage

$$\boldsymbol{x}_h^* = \boldsymbol{x}_l + \delta_s (\boldsymbol{x}_h - \boldsymbol{x}_l)$$

$$\boldsymbol{x}_s^* = \boldsymbol{x}_l + \delta_s (\boldsymbol{x}_s - \boldsymbol{x}_l)$$

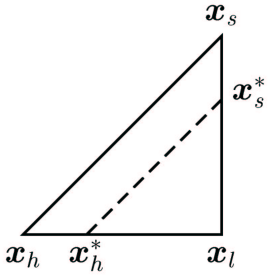

Figure 5.3: Basic steps of the Nelder and Mead simplex method (adapted from Rowan, 1990).

Chapter 6

Examples and Discussion

6.1 Introduction

The synthesis of nonlinear transient gravity waves in random seas is illustrated by two examples. The first one addresses a single design wave and the second one a tailored group of three successive waves embedded in a random seaway. The general procedure to generate the desired wave regimes is described in Section 5.1.

In this investigation, the selected design variance spectrum is the finite depth TMA spectrum. The water depth and sea state parameters are equal in both examples and are defined in Table 6.1. The discretization and wave absorption parameters used in the numerical simulation of the nonlinear wave evolution are derived from the sea state parameters and are summarized in Table 6.2. The maximum stroke, velocity and acceleration of the wave board motion are taken into account in the optimization procedure to enable experimental investigations in a physical wave tank. The values of these constraints are shown in Table 6.3.

The discrete wavelet transform of the wave board motion plays a central role in the time consuming subplex fitting. The decomposition scale is always $M = 3$ in this study.

The SQP optimization of the linear wave train terminates if the magnitude of the directional derivative in search direction is less than $1.0 \cdot 10^{-3}$ and the constraint violation is less than $1.0 \cdot 10^{-2}$. The subplex fitting of the nonlinear wave train terminates if the value of the objective function is less than $1.0 \cdot 10^{-4}$ in the first example and $5.0 \cdot 10^{-3}$ in the second one.

The next two sections describe target wave characteristics, objective functions, constraints and associated results for the single transient wave and the wave group synthesized in a random sea.

Water depth	h	=	$5.00\,m$
Variance of TMA spectrum	m_0	=	$0.011\,m^2$
Significant wave height	H_s	=	$0.425\,m$
Peak period	T_p	=	$3.13\,s$
Mean period	$\bar{T}$	=	$2.54\,s$
Mean frequency	$\bar{\omega}$	=	$2.48\,rad/s$
Mean wave length	$\bar{L}$	=	$10.00\,m$

Table 6.1: Parameters of the model sea state.

Tank length	l	=	$250.00\,m$
Spatial resolution	$\Delta x = \bar{L}/30$	=	$0.33\,m$
Temporal resolution	$\Delta t = \bar{T}/30$	=	$0.085\,s$
Number of horizontal grid nodes	$NX + 1 \approx l/\Delta x + 1$	=	751
Number of vertical grid nodes	$NZ + 1 \approx h/\Delta x + 3$	=	18
Length of numerical beach	$l_{beach} = 2\,\bar{L}$	=	$20.00\,m$
Strength of numerical beach	$\omega_{beach} = \bar{\omega}/2$	=	$1.24\,rad/s$

Table 6.2: Parameters of the nonlinear numerical simulation.

Maximum stroke	x_{max}	=	$2.00\,m$
Maximum velocity	u_{max}	=	$1.70\,m/s$
Maximum acceleration	a_{max}	=	$2.20\,m/s^2$

Table 6.3: Constraints on the wave board motion.

6.2 Synthesized Wave in Random Sea

A single transient wave is synthesized in a random sea which is defined in Table 6.1. The global parameters are the significant wave height H_s, the peak period T_p and the water depth h. The target characteristics of the transient wave define an extreme wave event at a particular time and location in the wave tank. The desired wave height is twice the significant wave height and the associated crest elevation is set to 60 % of the wave height. The wave period is selected to be the peak period. All local parameters are determined by the zero-downcrossing method and are summarized in Table 6.4.

Firstly, a linear approximation of the desired wave train is computed by optimizing the wavelet representation of the wave board motion for equality and inequality constraints which correspond to the desired wave char-

acteristics. The free variables are the values of an initially random phase spectrum, leaving the energy distribution, in terms of the variance spectrum, unchanged during the optimization. This linear initial guess is further improved by fitting the nonlinear wave evolution simulated in a numerical wave tank to the target characteristics. The free variables are now particular wavelet coefficients which correspond to a certain resolution scale and time range responsible for the evolution of the target wave.

Space domain					
Target location	x_{target}	=	$20\,h$	=	$100.00\,m$
Time domain					
Target wave height	H_{target}	=	$2\,H_s$	=	$0.85\,m$
Target wave period	T_{target}	=	T_p	=	$3.13\,s$
Target crest height	$\zeta_{c,\,target}$	=	$0.6\,H_{target}$	=	$0.51\,m$
Target crest location	$t_{\zeta_c,\,target}$	=	$26\,T_p$	=	$81.39\,s$

Table 6.4: Target parameters of the synthesized wave.

6.2.1 Generation of Linear Target Wave Train

As long as linear wave theory is applied, the sea state can be regarded as the superposition of independent harmonic waves, each having a particular direction, amplitude, frequency and phase. For a given design variance spectrum of an unidirectional wave train, the phase spectrum is responsible for the local characteristics, e.g. the wave height and period distribution as well as the location of the highest wave crest in space and time. For this reason, an initially random phase spectrum $arg\,F(\omega)$ is systematically modified by the SQP method to generate the desired target wave train with specified local properties. The phase values $\boldsymbol{\beta} = (\beta_1, \beta_2, \ldots \beta_n)^T$ are bounded by $-\pi \leq \beta_j \leq \pi$ and are initially determined from $\beta_j = 2\pi(R_j - 0.5)$ where R_j are random numbers in the interval 0 to 1.

The motion of the wave board $x_B(t)$ is determined by transforming the linear wave train at $x = x_{target}$ in terms of the complex Fourier transform $F_{target}(\omega)$ to the location of the wave generator at $x = 0$ and applying the complex hydrodynamic transfer function $F_{hydro}(\omega)$, which relates wave board motion to surface elevation close to the wave generator:

$$x_B(t) = IFFT\left[F_{target}(\omega) \cdot F_{trans}(\omega) \cdot F_{hydro}(\omega)\right] \tag{6.1}$$

where $F_{trans}(\omega_j) = \exp(i\, k_j\, x_{target})$, and ω_j and k_j are related by the dispersion equation (2.21).

The objective function of the SQP optimization problem is formulated such that the energy of the wave board motion is reduced in the higher frequency range which correlates with the detail wavelet coefficients d_k^m at scales $m = 1, 2$ and 3; compare Eq. (4.22). Hence, the best part of the relevant signal information is focused to the 3-level approximation coefficients c^3. The target zero-downcrossing wave characteristics define equality constraints. The maximum stroke x_{max}, velocity u_{max} and acceleration a_{max} of the wave board motion $x_B(t)$ define inequality constraints to be taken into account. The complete SQP optimization problem is stated as:

$$\underset{\boldsymbol{\beta} \in \Re^n}{\text{minimize}} \;\; f(\boldsymbol{\beta}) \;=\; \sum_{k=1}^{K/2} \big(d_k^1\big)^2 + \sum_{k=1}^{K/4} \big(d_k^2\big)^2 + \sum_{k=1}^{K/8} \big(d_k^3\big)^2 \;=$$

$$\sum_{k=1}^{K/2} \langle x_B(t), \psi(t)_{1,k} \rangle^2 + \sum_{k=1}^{K/4} \langle x_B(t), \psi(t)_{2,k} \rangle^2 + \sum_{k=1}^{K/8} \langle x_B(t), \psi(t)_{3,k} \rangle^2 \qquad (6.2)$$

$$\begin{aligned}
\text{subject to} \quad g_1 &= H_i - H_{target} \;=\; 0, \\
g_2 &= T_i - T_{target} \;=\; 0, \\
g_3 &= \zeta_{c,\,i} - \zeta_{c,\,target} \;=\; 0, \\
g_4 &= t_{\zeta_c,\,i} - t_{\zeta_c,\,target} \;=\; 0, \\
g_5 &= \max\Big\{ |x_B(t)| \Big\} - x_{max} \;\leq\; 0, \\
g_6 &= \max\Big\{ |\dot{x}_B(t)| \Big\} - u_{max} \;\leq\; 0, \\
g_7 &= \max\Big\{ |\ddot{x}_B(t)| \Big\} - a_{max} \;\leq\; 0, \\
g_{7+j} &= -\pi - \beta_j \;\leq\; 0, \quad j = 1, \ldots, n \\
g_{7+n+j} &= -\pi + \beta_j \;\leq\; 0, \quad j = 1, \ldots, n
\end{aligned} \qquad (6.3)$$

where $f(\boldsymbol{\beta})$ is the objective function to be minimized. Both the wave board motion and the linear surface elevation are described by $K = N = 1024$ data points with a time step of $\Delta t = 0.1\,s$ resulting in a time window of $102.3\,s$. The design variance spectrum remains unchanged and $n = 99$ components in the frequency range of $\omega/\omega_p = 0.5$ to $\omega/\omega_p = 3.5$ are considered.

Fig. 6.1 shows ten different solutions to the optimization problem defined in Eqs. (6.2) and (6.3) for different initial phase distributions. The target parameters are always met, since they are part of the constraints. Fig. 6.1 further indicates that only local minima may be found by the SQP optimization and that the resulting wave train is still random.

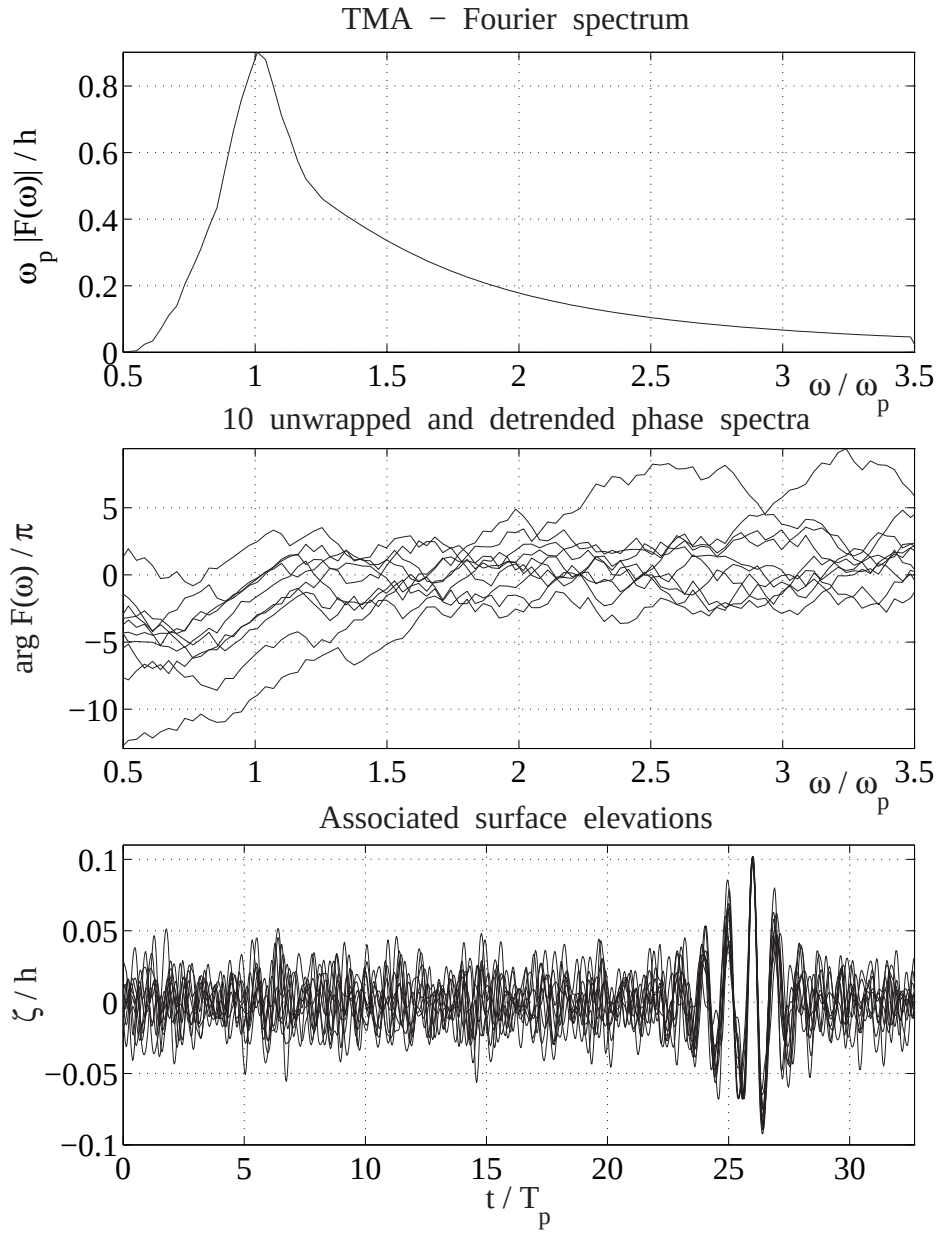

Figure 6.1: Ten solutions to the optimization problem stated in Eqs. (6.2) and (6.3) resulting from ten different initially random phase distributions.

One of the above wave regimes is analyzed in more detail. Fig. 6.2 shows the minimization of the objective function $f(\boldsymbol{\beta})$ stated in Eq. (6.2). The optimization terminates successfully at $f(\boldsymbol{\beta}) = 0.16$ after 2223 function evaluations. The magnitude of the directional derivative in search direction is $3.1 \cdot 10^{-4}$ and the maximum constraint violation is $2.3 \cdot 10^{-5}$.

The wave board motions derived from the initially random and optimized phase spectrum are compared in Fig. 6.3. Using a linear wave model implies that the high target wave can only be generated at a particular location by disperse focusing of several wave components. The wave group evolving to the target wave can be easily identified in the optimized wave board motion. The detail wavelet coefficients are especially reduced in the third decomposition level d^3, which correlates in Fig. 6.3 to the coefficients in the range of 128 to 255. This improved compression is an advantage for the subsequent fitting procedure, since the interesting part of the wave board motion can be modified very efficiently by only a few approximation coefficients.

Fig. 6.4 shows the associated linear wave train at the target location, which is represented in frequency domain by Fourier and phase spectrum. The latter is one possible solution found by the SQP optimization. It can be observed that all global and local target wave characteristics defined in Table 6.4 are met. The zero-downcrossing method is applied to the wave train and 47 individual waves are identified. The associated height, crest and period structure are presented.

Linear wave theory is not appropriate for describing extreme waves, since nonlinear free surface effects significantly influence the wave evolution. However, the linear description of the wave train allows us to determine an initial guess of the wave board motion, i.e. time-dependent boundary conditions required for simulating the nonlinear wave train in the numerical wave tank. The parameters used in the numerical calculation are summarized in Table 6.2. Fig. 6.5 shows that the deviations between linear and nonlinear wave evolution increase with the distance from the wave generator. The details of the surface elevation at the target location of $x/h = 20$ reveal that the nonlinear wave is faster and higher than the linear one which corresponds to the target parameters. The Fourier and phase spectrum, as well as wave height, crest and period structure of the nonlinear wave train, are presented in Fig. 6.6. The asymmetry and period are significantly lower than desired. Note that the Fourier spectrum of the nonlinear wave train depends on the location in the wave tank, since wave energy might be shifted with frequency due to nonlinear modulation effects. The precise values of the deviations are summarized in Table 6.5. The largest one is the wave height with 17.8 %. These deviations are reduced considerably by applying another optimization method directly to the nonlinear wave evolution.

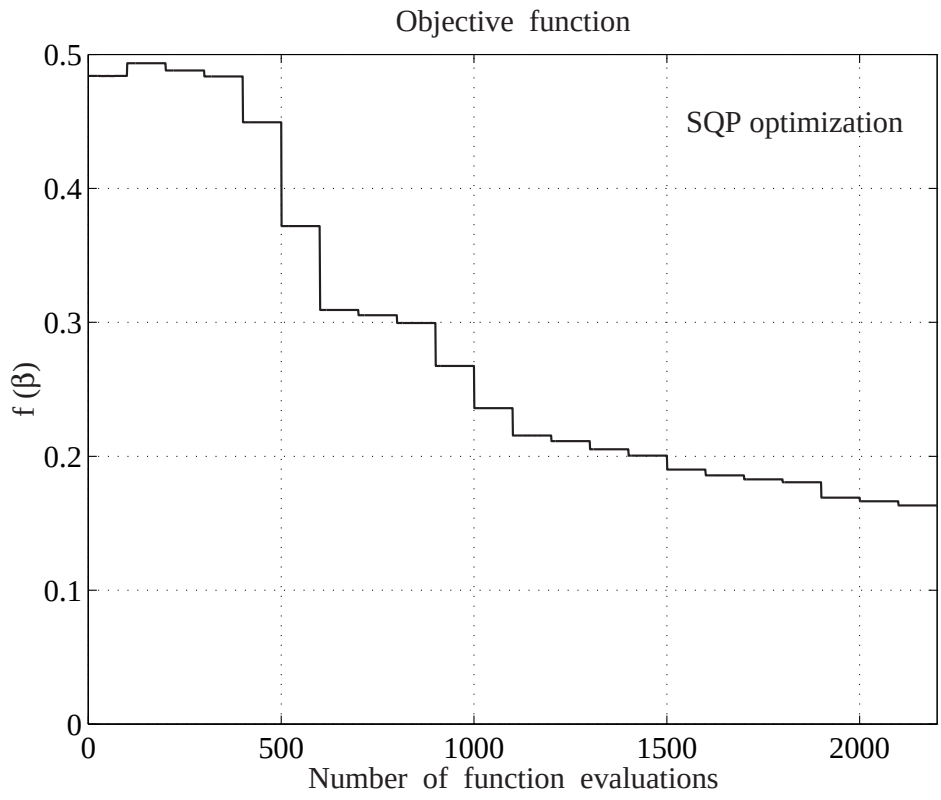

Figure 6.2: Example 1: Minimization of objective function defined in Eq. (6.2) with SQP method.

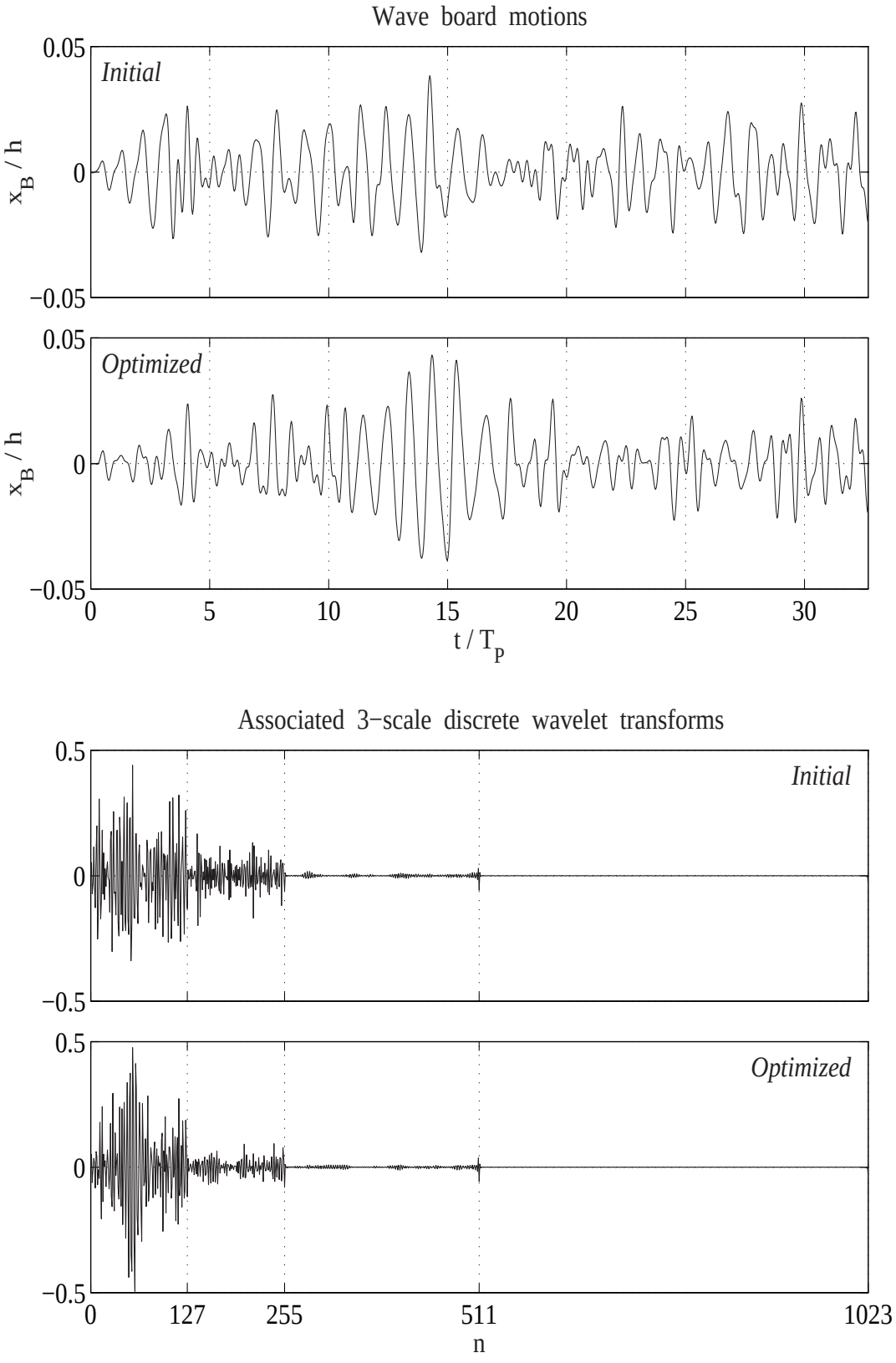

Figure 6.3: Example 1: Initial and SQP-optimized wave board motion with associated discrete wavelet transforms.

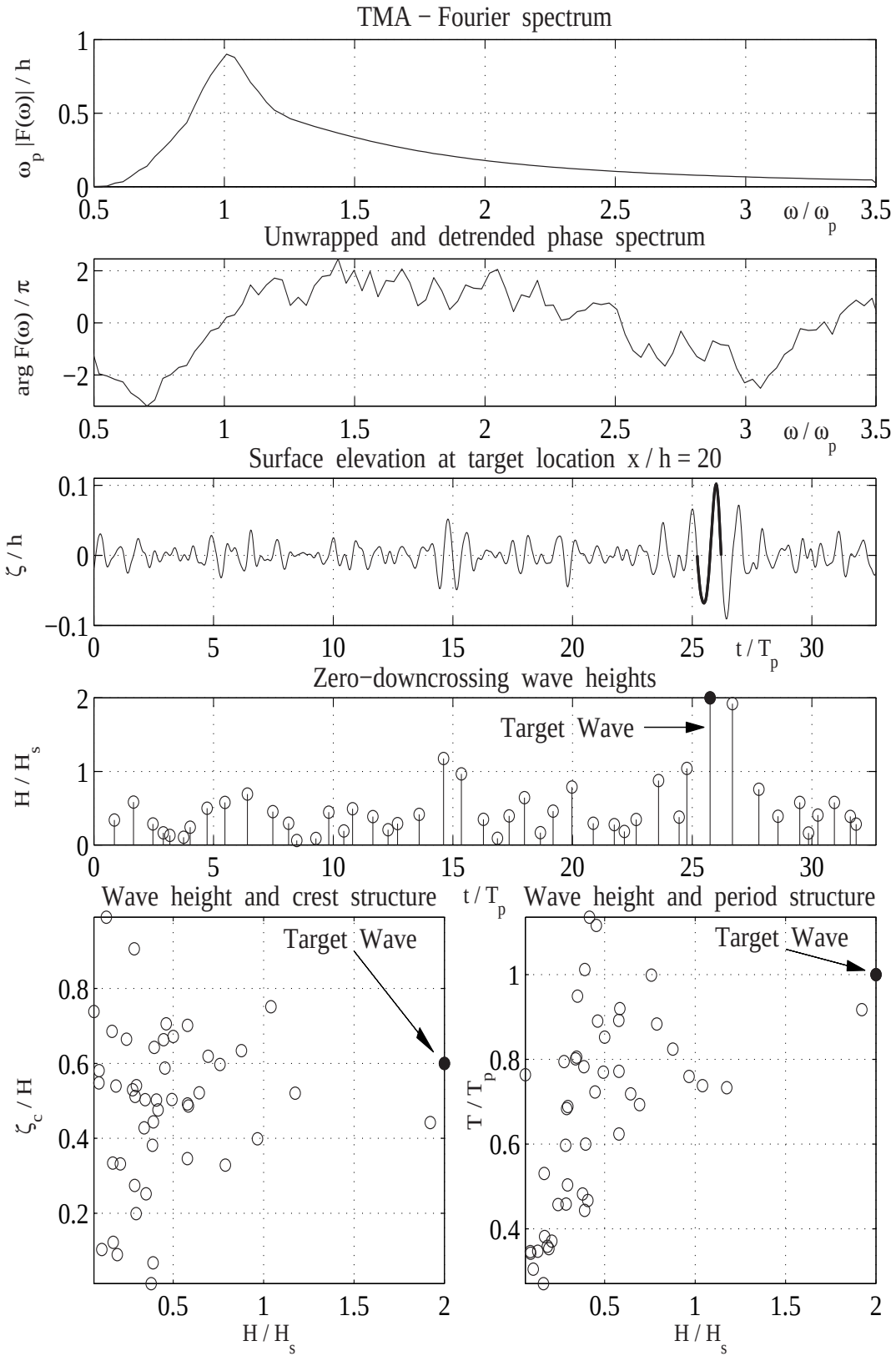

Figure 6.4: Example 1: Characteristics of linear wave train with synthesized wave.

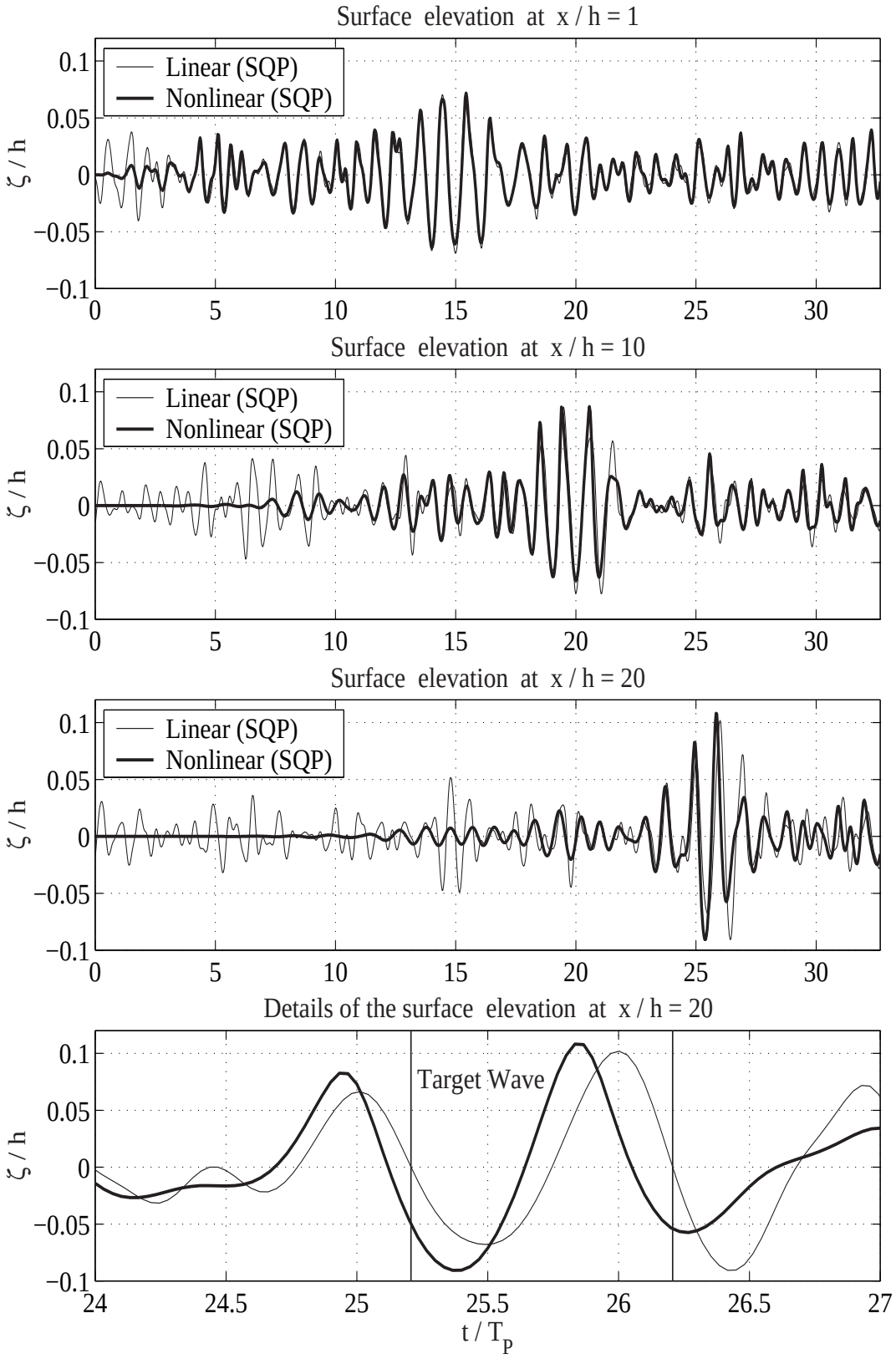

Figure 6.5: Example 1: Comparison of linear and nonlinear evolution of synthesized wave. Wave board motion used in nonlinear simulation generated with SQP method.

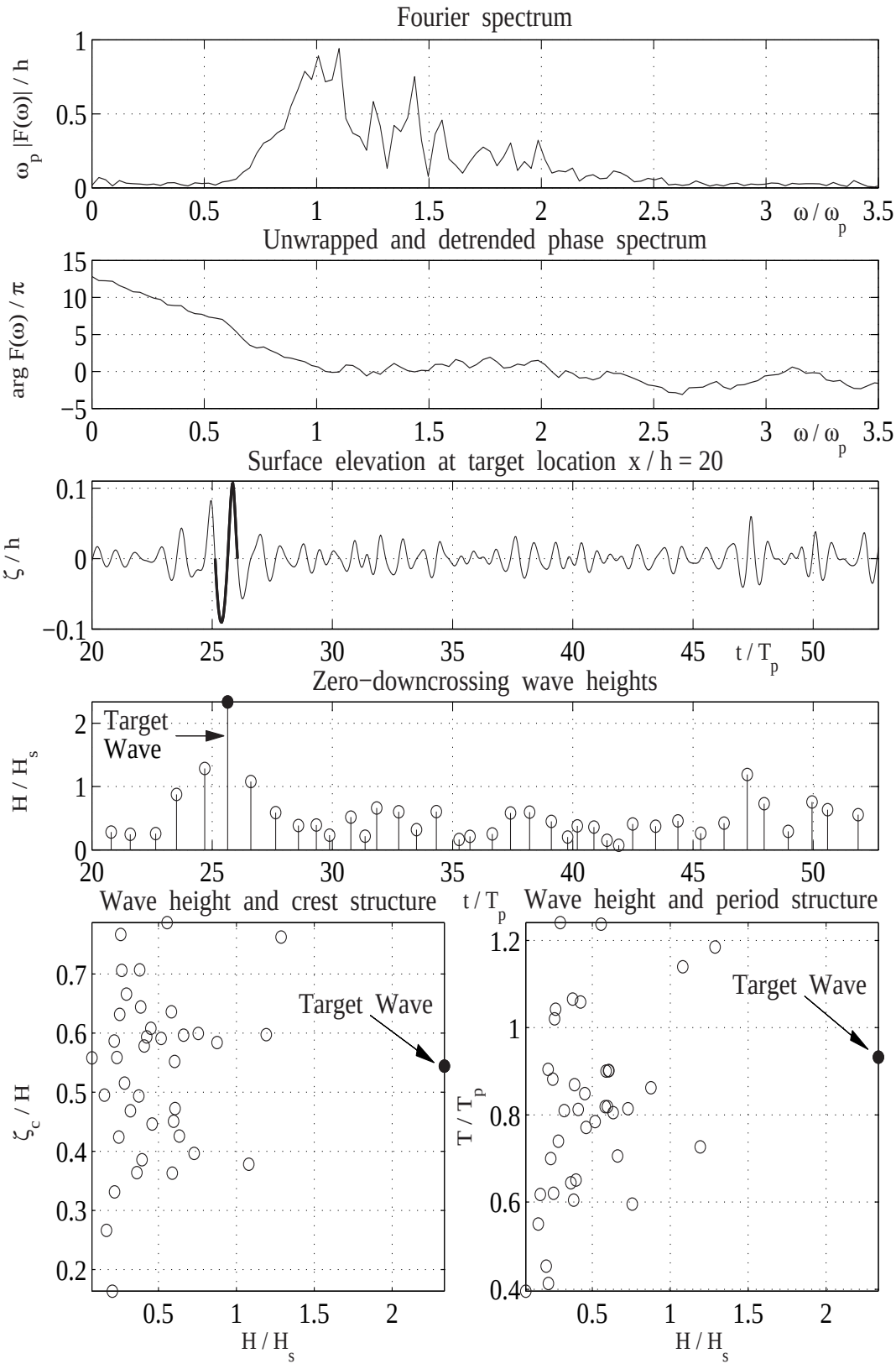

Figure 6.6: Example 1: Further characteristics of nonlinear wave train with synthesized wave. Wave board motion used in nonlinear simulation generated with SQP method.

6.2.2 Generation of Nonlinear Target Wave Train

The linear initial guess is further improved by fitting the nonlinear wave evolution simulated in a numerical wave tank to the target characteristics. The starting point is the discrete wavelet transform of the SQP-optimized wave board motion shown in Fig. 6.3. Most of the signal energy is focused to the 3-level approximation coefficients $c^3 = \{c_0, c_1, \ldots, c_{127}\}$. The free variables are selected to be the $n = 51$ coefficients $\boldsymbol{c} = (c_{38}, c_{39}, \ldots, c_{88})^T$, which correspond to the time window between $t/T_p = 9.6$ and $t/T_p = 22.4$. This part of the wave board motion is responsible for the evolution of the transient target wave. The fitting problem, to be solved with the subplex method, is formulated as:

$$\underset{\boldsymbol{c}\in\Re^n}{\text{minimize}} \;\; f(\boldsymbol{c}) \;=\; \left(\frac{H_i - H_{target}}{H_{target}}\right)^2 + \left(\frac{T_i - T_{target}}{T_{target}}\right)^2 + \tag{6.4}$$

$$\left(\frac{\zeta_{c,\,i} - \zeta_{c,\,target}}{\zeta_{c,\,target}}\right)^2 + \left(\frac{t_{\zeta_c,\,i} - t_{\zeta_c,\,target}}{t_{\zeta_c,\,target}}\right)^2 + \left(\frac{\sigma\big(x_B(t)\big) - \sigma\big(x_B(t)_{initial}\big)}{\sigma\big(x_B(t)_{initial}\big)}\right)^2$$

$$\begin{aligned} \text{subject to} \quad g_1 &= \max\Big\{|x_B(t)|\Big\} - x_{max} \;\le\; 0, \\ g_2 &= \max\Big\{|\dot{x}_B(t)|\Big\} - u_{max} \;\le\; 0, \\ g_3 &= \max\Big\{|\ddot{x}_B(t)|\Big\} - a_{max} \;\le\; 0, \end{aligned} \tag{6.5}$$

where $\sigma\big(x_B(t)\big)$ is the standard deviation of the wave board motion. The inclusion of $\sigma\big(x_B(t)\big)$ is necessary to control the total energy input which corresponds to the significant wave height H_s as a global target parameter.

Fig. 6.7 shows the minimization of the objective function $f(\boldsymbol{c})$ with the straight vertical lines indicating infeasible points due to wave breaking or constraint violation. The subplex fitting terminates successfully at $f(\boldsymbol{c}) = 9.9 \cdot 10^{-5}$ after 1350 function evaluations.

The improved wave board motion is compared in Fig. 6.8 to the linear initial guess. It can be observed that the highest elevations are reduced by the fitting procedure to decrease the height of the transient target wave. Further details of the nonlinear wave evolution are illustrated in Fig. 6.9. The asymmetry and the peak period of the target wave are increased compared to the nonlinear wave that originates from the first initial guess of the wave board motion. The zero-downcrossing characteristics of the improved wave train are presented in Fig. 6.10. The properties of the desired transient wave are very close to the target values with a maximum deviation of 0.6 %; compare Table 6.5.

	$H\,/\,H_s$	$T\,/\,T_p$	$\zeta_c\,/\,H$	$t_{\zeta_c}\,/\,T_p$
Target value	**2.000**	**1.000**	**0.600**	**26.000**
SQP value	2.356	0.931	0.544	25.849
Deviation in %	17.8	−6.9	−9.3	−0.6
Subplex value	1.998	0.994	0.597	25.862
Deviation in %	−0.1	−0.6	−0.5	−0.5

Table 6.5: Conformity of the nonlinear synthesized wave with target parameters.

The smoothed variance spectra at different locations in the wave tank are presented in Fig. 6.11. Ten adjacent points have been used for moving average filtering the raw FFT-spectra in frequency domain. At a 95% confidence level, the lower confidence limit is 0.6 and the upper limit is 2.0 of the spectral estimate. Note that a perfect correlation between the spectra can not be expected due to the several uncertainties related to the fast Fourier transform and the filtering process. At target location $x/h = 20$, the zeroth spectral moment $m_0 = 0.099$ and the peak period $T_p = 3.17\,s$ differ slightly from the target values, since they have not been considered explicitly in the fitting procedure.

Fig. 6.12 shows the energy flux at the same locations. As can be observed, the energy flux is strongly focused on the target time $t/T_p = 26$ where the crest of the transient design wave is located. The evolution of the subplex-fitted nonlinear transient wave in space and time is illustrated in Fig. 6.13. It shows that the energy is propagated at a distinctly slower speed than the wave crests and troughs; this is a typical feature of gravity waves in deep and intermediate water. At $t/T_p = 26$ the steepness of the target wave is $H/L = 0.043$. The associated distributions of the horizontal particle velocity, acceleration and dynamic pressure are shown in Fig. 6.14. The high transient wave has an effect on the flow field down to the bottom of the wave tank, but the magnitude of velocity, acceleration and dynamic pressure decreases exponentially with water depth. The maximum zero-upcrossing crest and wave height, as well as wave steepness, are presented in Fig. 6.15. The entire wave tank is analyzed to obtain these values. Hence they do not correlate to a particular wave which is traced in time. Occasionally steep waves are observed.

Much more information on the flow details is available from the numerical simulation, such as the complete energy fields or particle tracks as a function of time.

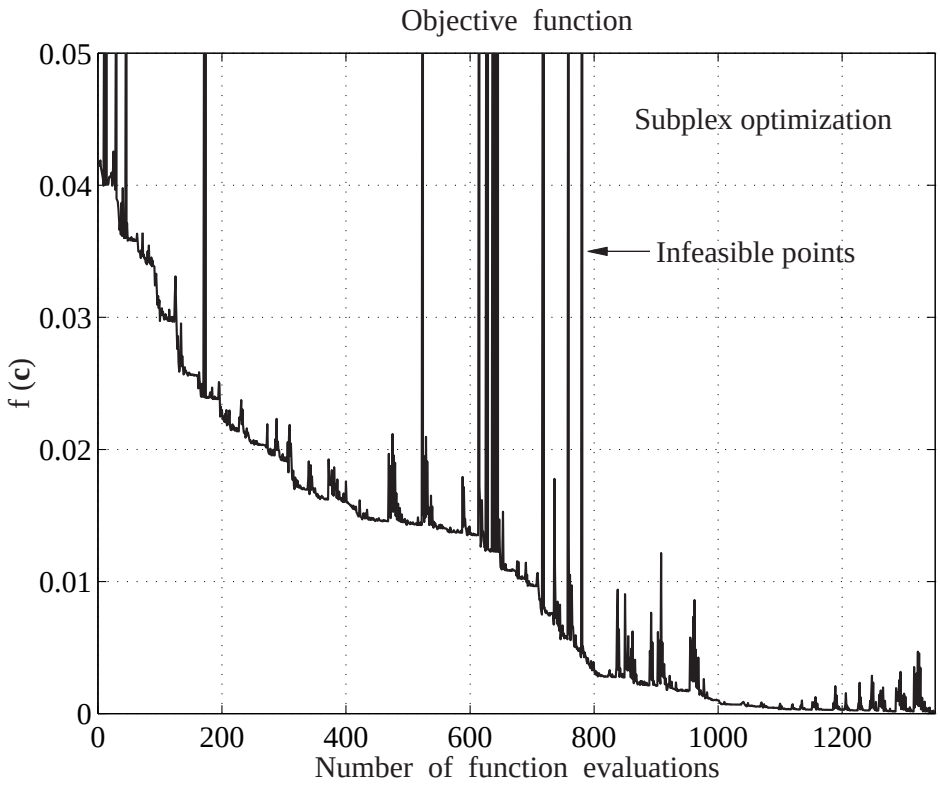

Figure 6.7: Example 1: Minimization of objective function defined in Eq. (6.4) with Subplex method.

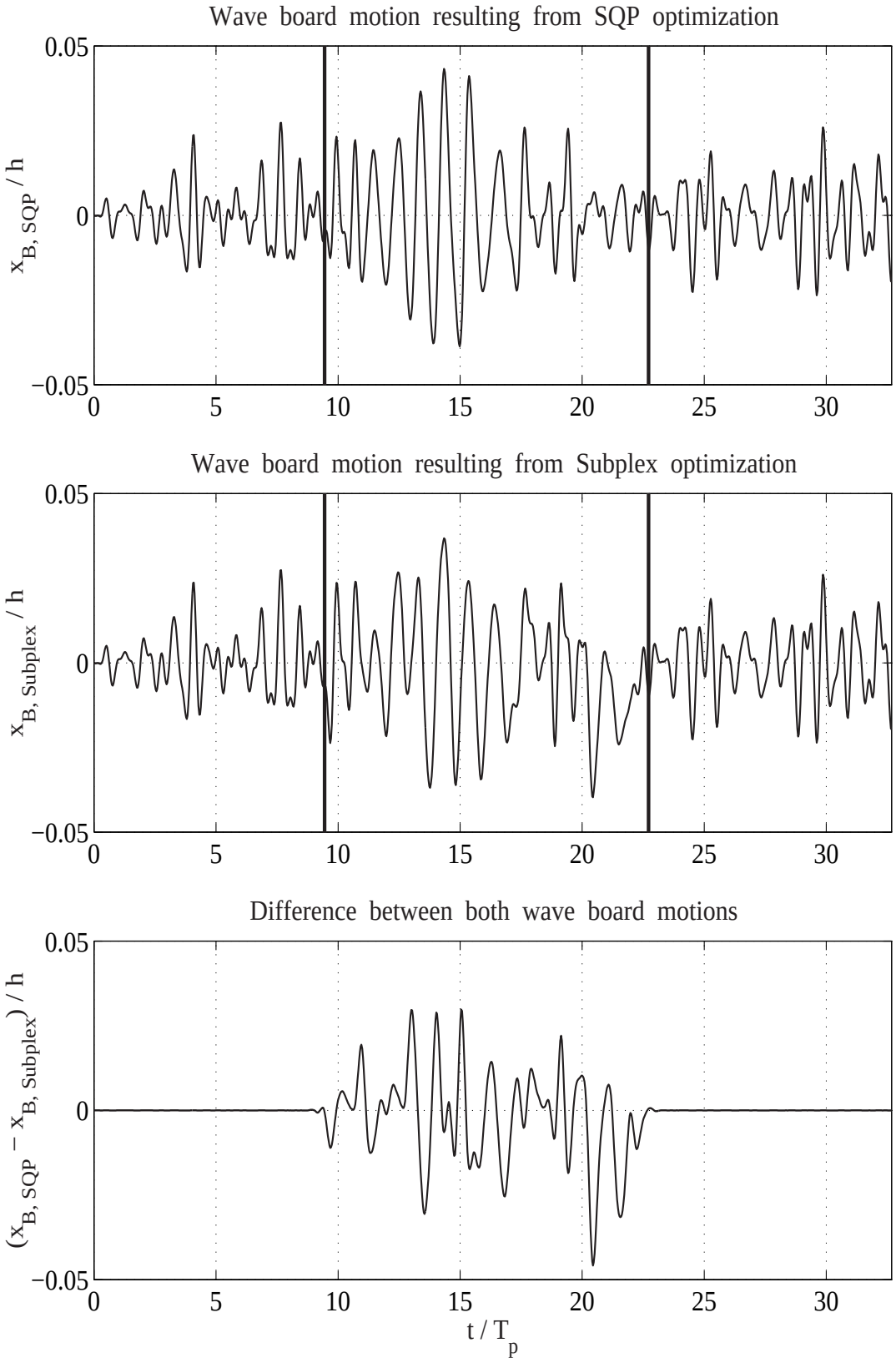

Figure 6.8: Example 1: Comparison of wave board motions generated with SQP and Subplex method.

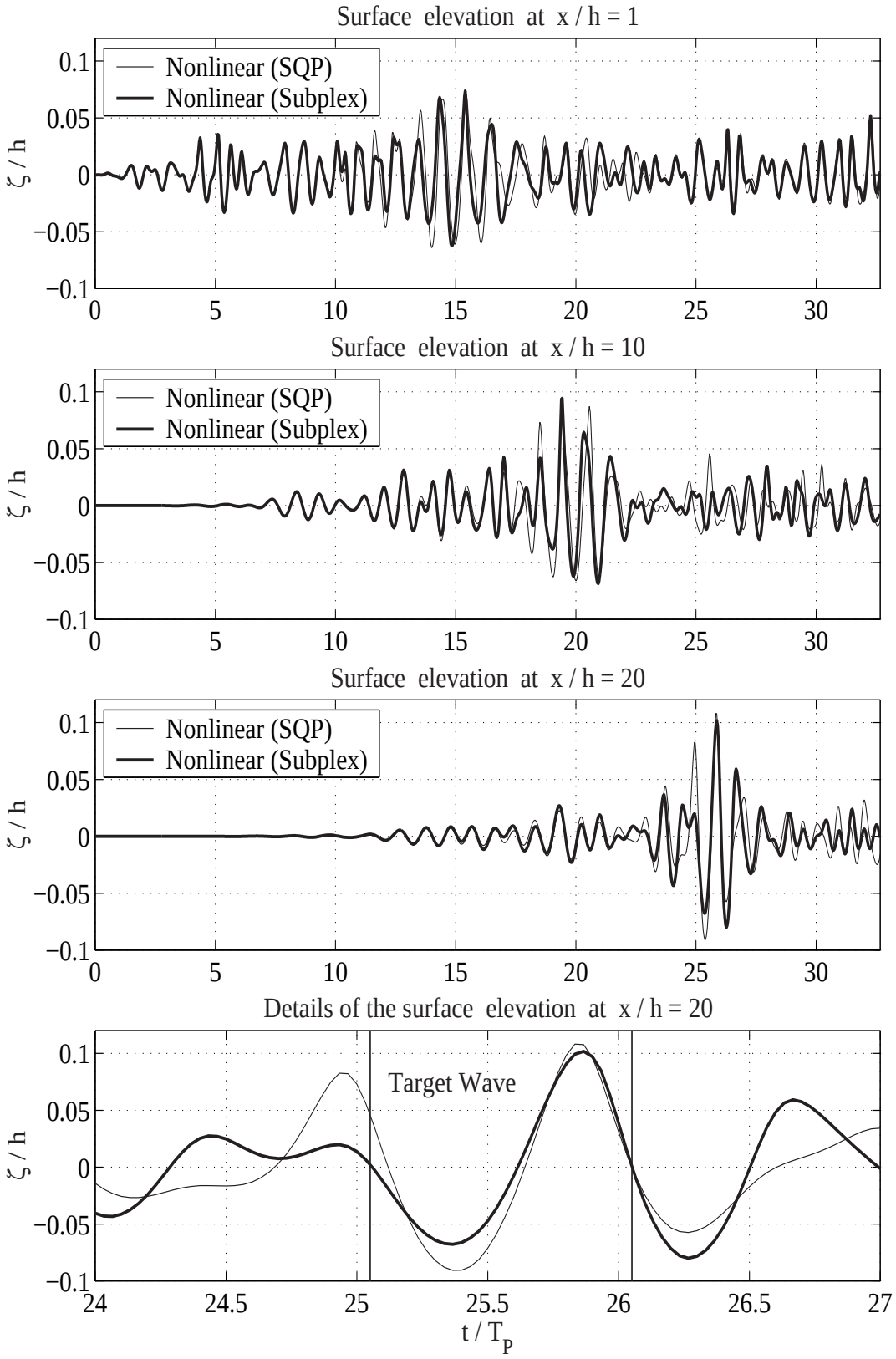

Figure 6.9: Example 1: Comparison of nonlinear evolution of synthesized waves. Wave board motion used in nonlinear simulations generated with SQP and Subplex method.

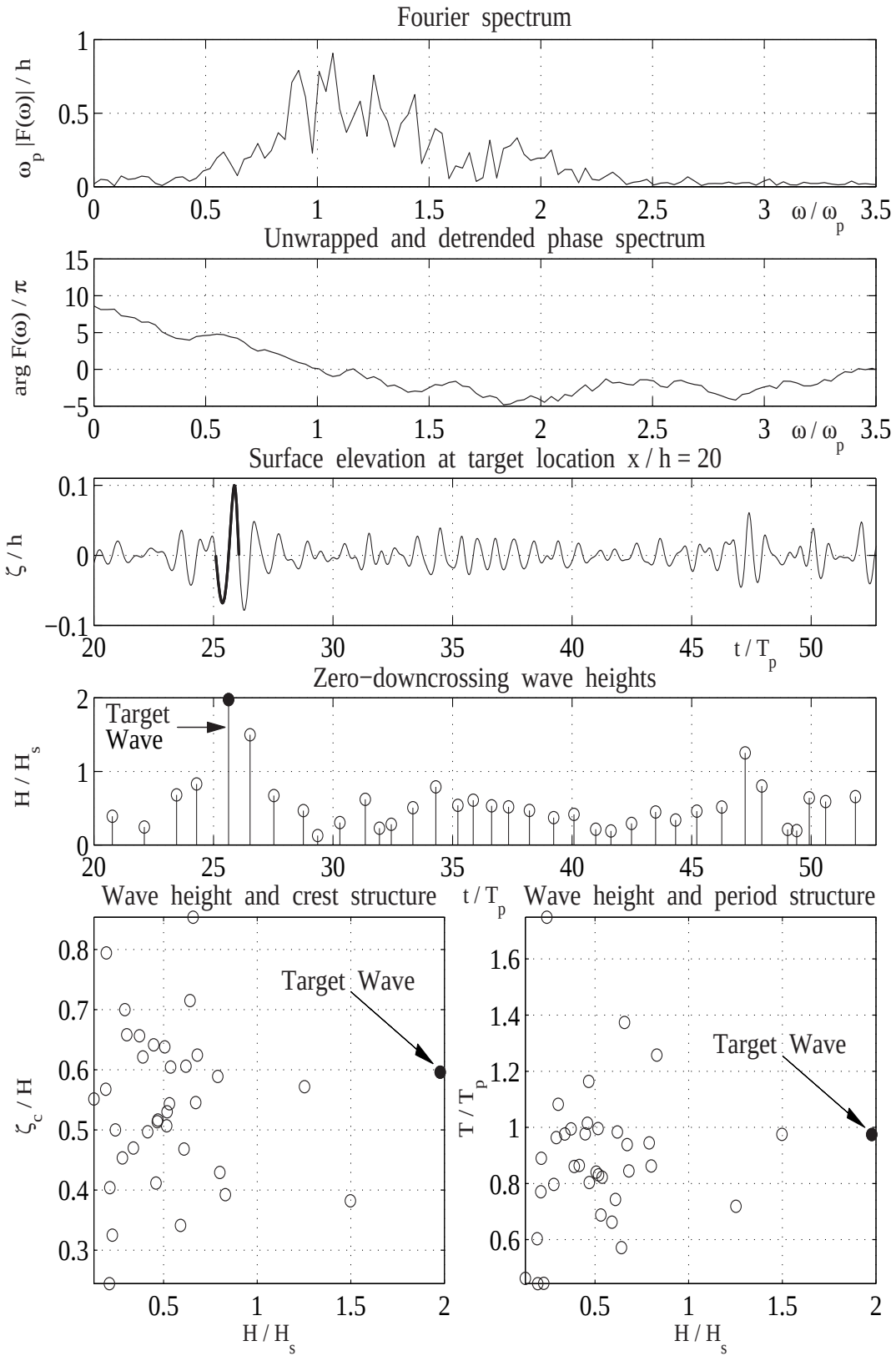

Figure 6.10: Example 1: Further characteristics of nonlinear wave train with synthesized wave. Wave board motion used in nonlinear simulation generated with Subplex method.

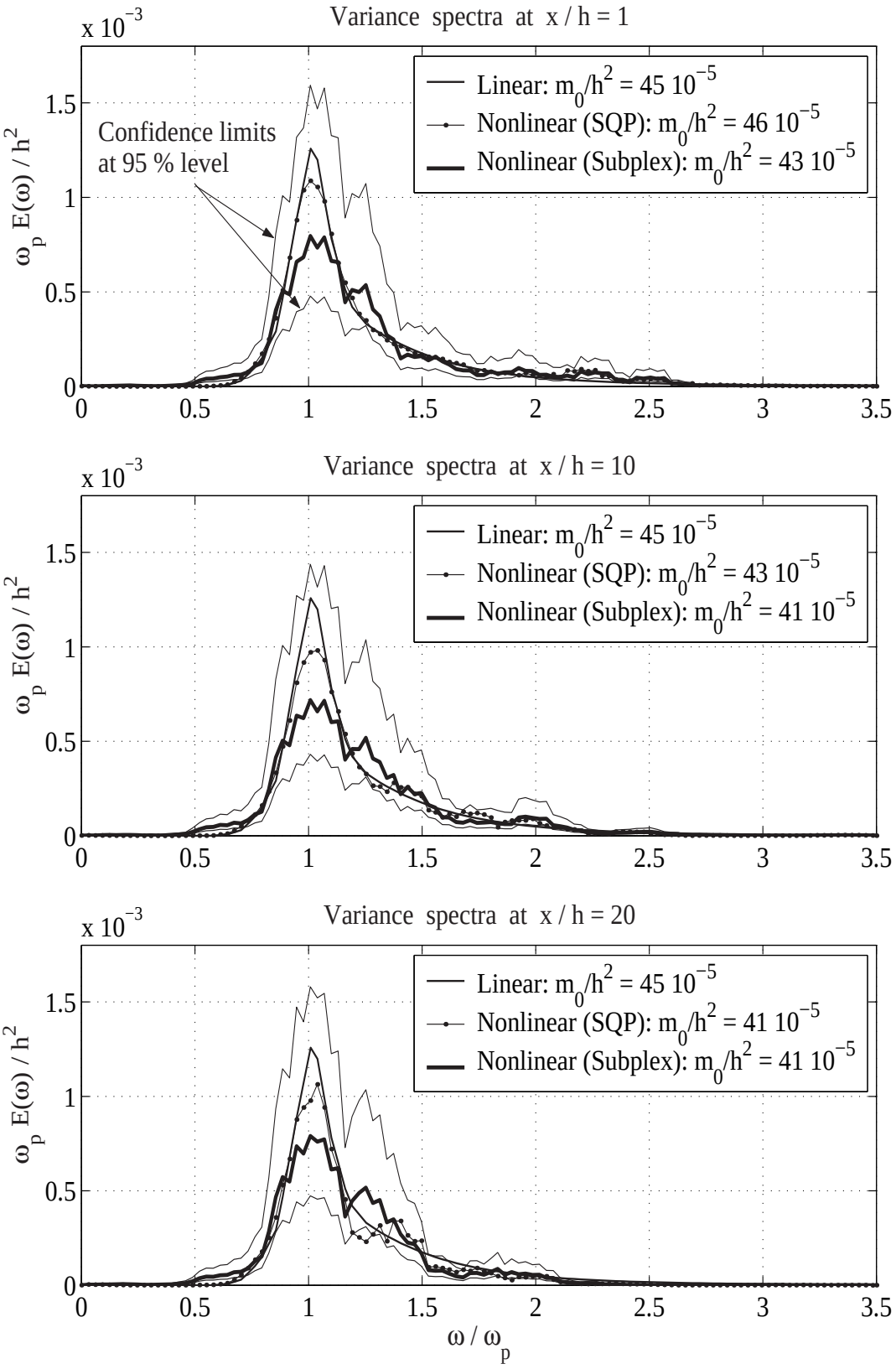

Figure 6.11: Example 1: Variance spectra of linear and nonlinear wave trains at different locations.

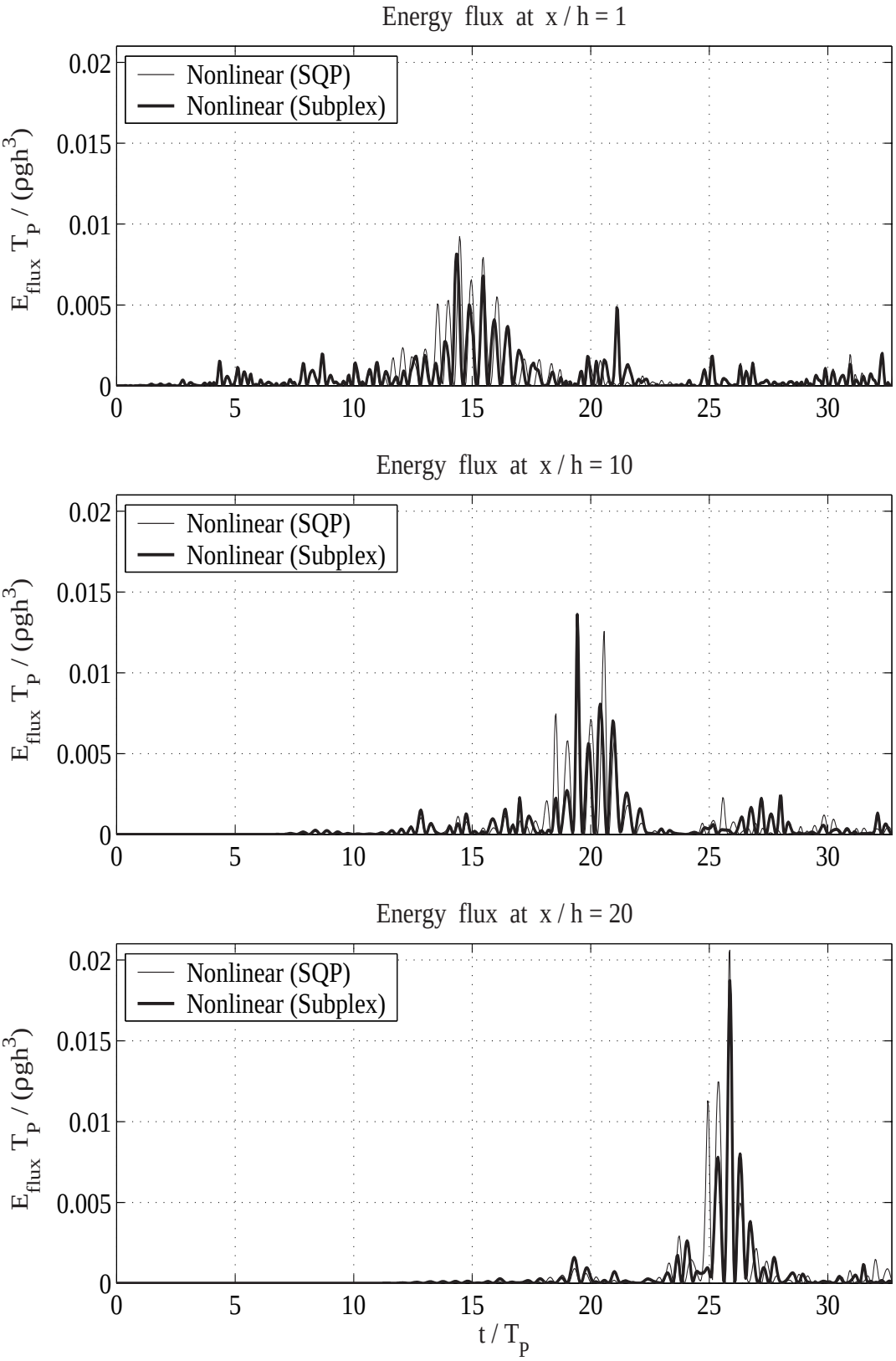

Figure 6.12: Example 1: Energy flux of linear and nonlinear wave trains at different locations.

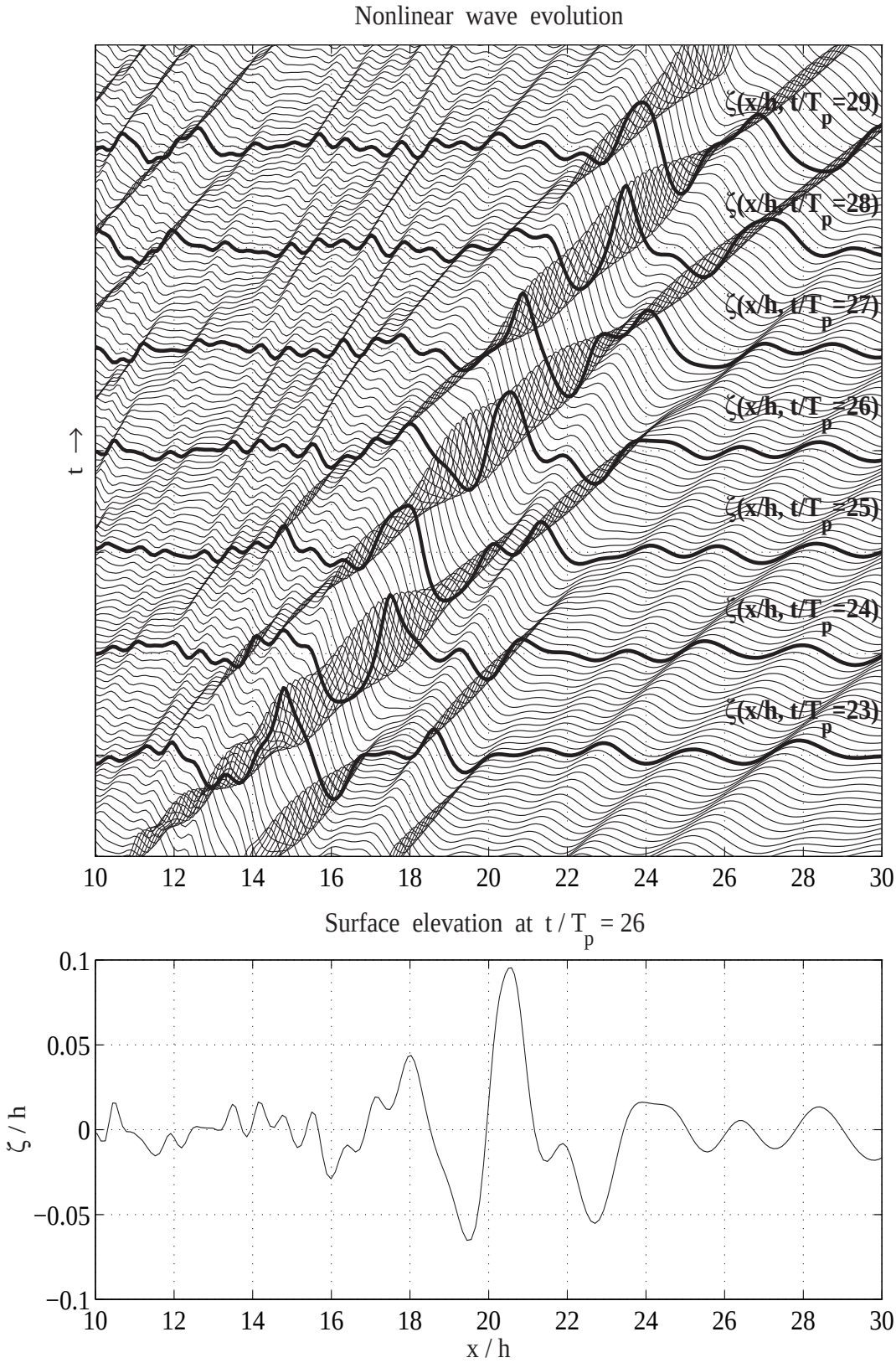

Figure 6.13: Example 1: Evolution of nonlinear synthesized wave in space and time domain. Wave board motion used in nonlinear simulation generated with Subplex method.

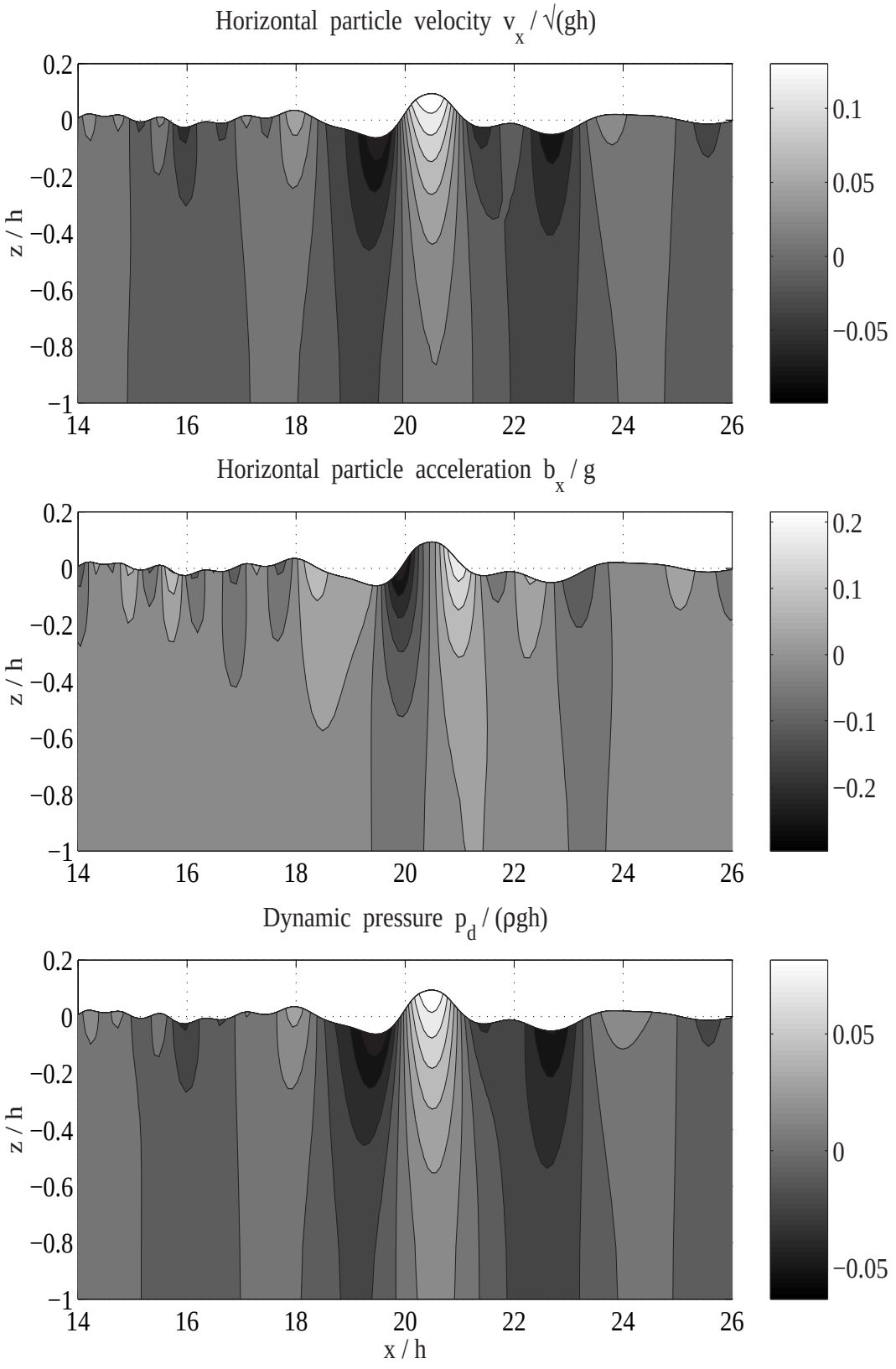

Figure 6.14: Example 1: Particle velocity, acceleration, and dynamic pressure field of nonlinear wave train with synthesized wave at $t/T_p = 26$. Wave board motion used in nonlinear simulation generated with Subplex method.

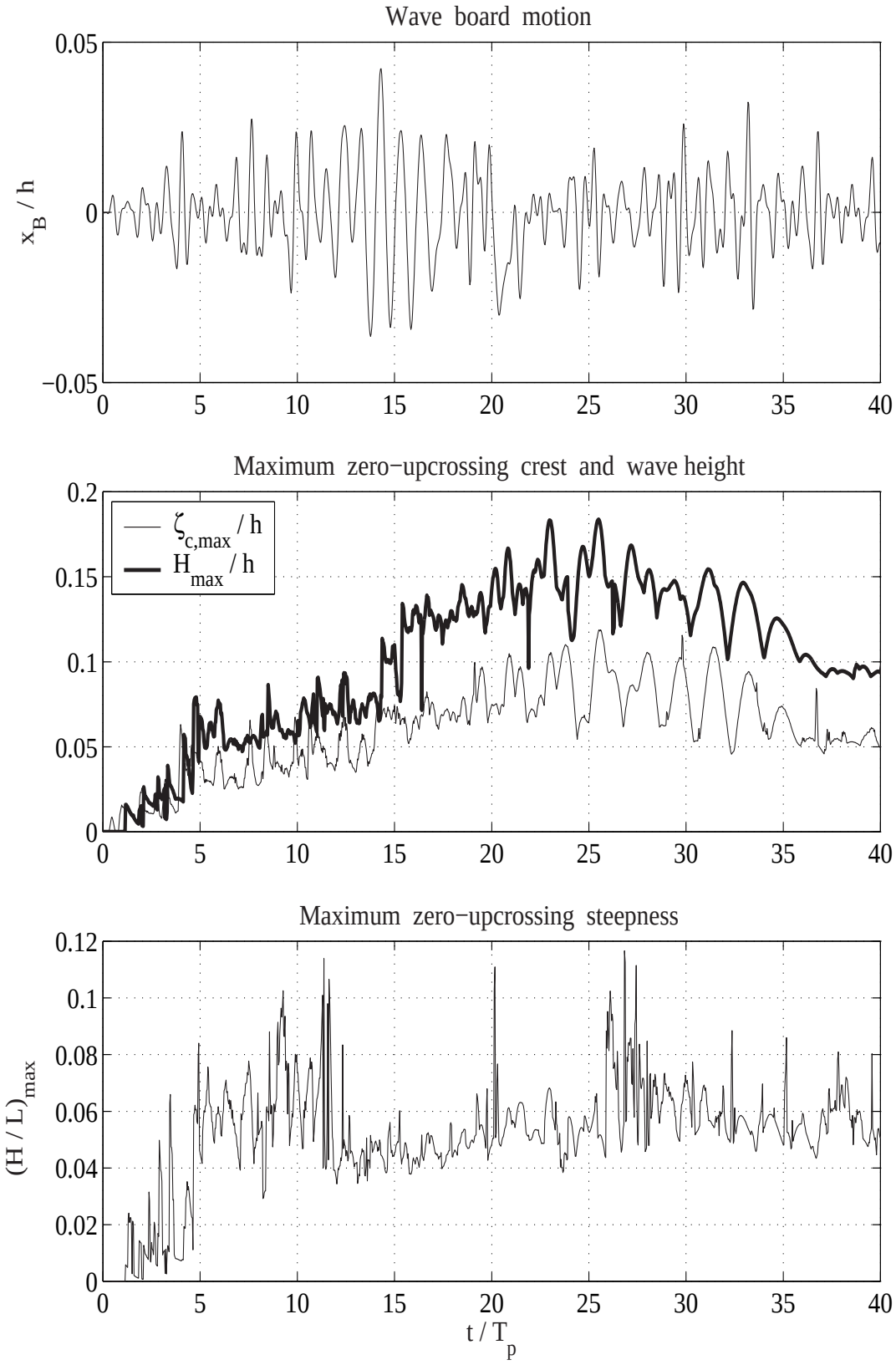

Figure 6.15: Example 1: Zero-upcrossing characteristics of nonlinear wave train with synthesized wave. Wave board motion used in nonlinear simulation generated with Subplex method.

6.3 Synthesized Wave Group in Random Sea

In the second example, a wave group of three successive waves is synthesized in a random sea. The global sea state parameters are the same as in the previous example and are defined in Table 6.1. The target wave height of the transient wave in the center of the group is twice the significant wave height H_s, which is twice the height of both adjacent waves. The target elevation of the center wave is set to 60 % of its height, and the target periods of all three waves are set to the peak period T_p. Further local parameters are the locations in space and time domain, which are defined in Table 6.6. The next sections describe the procedure to generate the linear and nonlinear target wave train in detail.

Space domain					
Target location	x_{target}	=	$20\,h$	=	$100.00\,m$
Time domain					
Wave 1:					
Target wave height	$H_{1,\,target}$	=	H_s	=	$0.425\,m$
Target wave period	$T_{1,\,target}$	=	T_p	=	$3.13\,s$
Wave 2:					
Target wave height	$H_{2,\,target}$	=	$2\,H_s$	=	$0.85\,m$
Target wave period	$T_{2,\,target}$	=	T_p	=	$3.13\,s$
Target crest height	$\zeta_{c,\,target}$	=	$0.6\,H_{2,\,target}$	=	$0.51\,m$
Target crest location	$t_{\zeta_c,\,target}$	=	$26\,T_p$	=	$81.39\,s$
Wave 3:					
Target wave height	$H_{3,\,target}$	=	H_s	=	$0.425\,m$
Target wave period	$T_{3,\,target}$	=	T_p	=	$3.13\,s$

Table 6.6: Target parameters of the synthesized wave group.

6.3.1 Generation of Linear Target Wave Train

The procedure for optimizing the linear wave train is exactly the same as the one described in Section 6.2.1. Only the equality constraints of the optimization problem, which define the target characteristics of the wave group, need to be adjusted. Hence the optimization problem is stated as:

$$\underset{\boldsymbol{\beta}\,\in\,\Re^n}{\text{minimize}}\;\; f(\boldsymbol{\beta}) \;=\; \sum_{k=1}^{K/2}\big(d_k^1\big)^2 + \sum_{k=1}^{K/4}\big(d_k^2\big)^2 + \sum_{k=1}^{K/8}\big(d_k^3\big)^2 \;=$$

$$\sum_{k=1}^{K/2}\langle x_B(t),\psi(t)_{1,k}\rangle^2 + \sum_{k=1}^{K/4}\langle x_B(t),\psi(t)_{2,k}\rangle^2 + \sum_{k=1}^{K/8}\langle x_B(t),\psi(t)_{3,k}\rangle^2 \tag{6.6}$$

$$\begin{aligned}
\text{subject to}\quad g_1 &= H_{i-1} - H_{1,\,target} \;=\; 0,\\
g_2 &= T_{i-1} - T_{1,\,target} \;=\; 0,\\
g_3 &= H_i - H_{2,\,target} \;=\; 0,\\
g_4 &= T_i - T_{2,\,target} \;=\; 0,\\
g_5 &= \zeta_{c,\,i} - \zeta_{c,\,target} \;=\; 0,\\
g_6 &= t_{\zeta_c,\,i} - t_{\zeta_c,\,target} \;=\; 0,\\
g_7 &= H_{i+1} - H_{3,\,target} \;=\; 0,\\
g_8 &= T_{i+1} - T_{3,\,target} \;=\; 0,\\
g_9 &= \max\Big\{|x_B(t)|\Big\} - x_{max} \;\le\; 0,\\
g_{10} &= \max\Big\{|\dot{x}_B(t)|\Big\} - u_{max} \;\le\; 0,\\
g_{11} &= \max\Big\{|\ddot{x}_B(t)|\Big\} - a_{max} \;\le\; 0,\\
g_{11+j} &= -\pi - \beta_j \;\le\; 0, \quad j = 1,\ldots,n\\
g_{11+n+j} &= -\pi + \beta_j \;\le\; 0, \quad j = 1,\ldots,n
\end{aligned} \tag{6.7}$$

where $f(\boldsymbol{\beta})$ is the objective function to be minimized. The superscripts of the detail wavelet coefficients d_k^1, d_k^2 and d_k^3 denote the approximation level of the discrete wavelet transform. The subscripts $i-1, i, i+1$ refer to the three successive waves of the target group determined by the zero-downcrossing method. The wave board motion and the linear surface elevation are described by $K = N = 1024$ data points with a time step of $\Delta t = 0.1\,s$ resulting in a time window of $102.3\,s$. The design variance spectrum remains unchanged and $n = 99$ components in the frequency range of $\omega/\omega_p = 0.5$ to $\omega/\omega_p = 3.5$ are considered.

Fig. 6.16 shows the optimization progress in terms of the objective function $f(\boldsymbol{\beta})$ defined in Eq. (6.6). The optimization terminates successfully at $f(\boldsymbol{\beta}) = 0.16$ after 4137 function evaluations. The magnitude of the directional derivative in search direction is $3.8 \cdot 10^{-4}$ and the maximum constraint violation is $1.1 \cdot 10^{-4}$. The detail wavelet coefficients of the third level d^3 are reduced as shown in Fig. 6.17. Identifying the target group in the optimized

wave board motion is difficult, though it is known from the previous example that the relevant time window is approximately $10 \leq t/T_p \leq 20$. Fig. 6.18 presents the linear wave train generated by the SQP method. All three waves of the target group show the desired zero-downcrossing characteristics summarized in Table 6.6. The wave height, crest and period structure of the 39 individual waves are shown as well.

The wave board motion derived from the linear wave train is used to simulate the nonlinear wave evolution in the numerical wave tank. Linear and nonlinear wave trains are compared in Fig. 6.19. The details of the surface elevation at the target location of $x/h = 20$ show that the characteristics of nonlinear wave group deviate significantly from the target parameters. In particular, the height of the third wave is only 42.6 % of the desired value; compare Table 6.7. Further details of the nonlinear wave train regarding the frequency representation as well as the height, crest and period structure are illustrated in Fig. 6.20. Note that the Fourier spectrum varies for nonlinear wave trains with the measurement location in the wave tank.

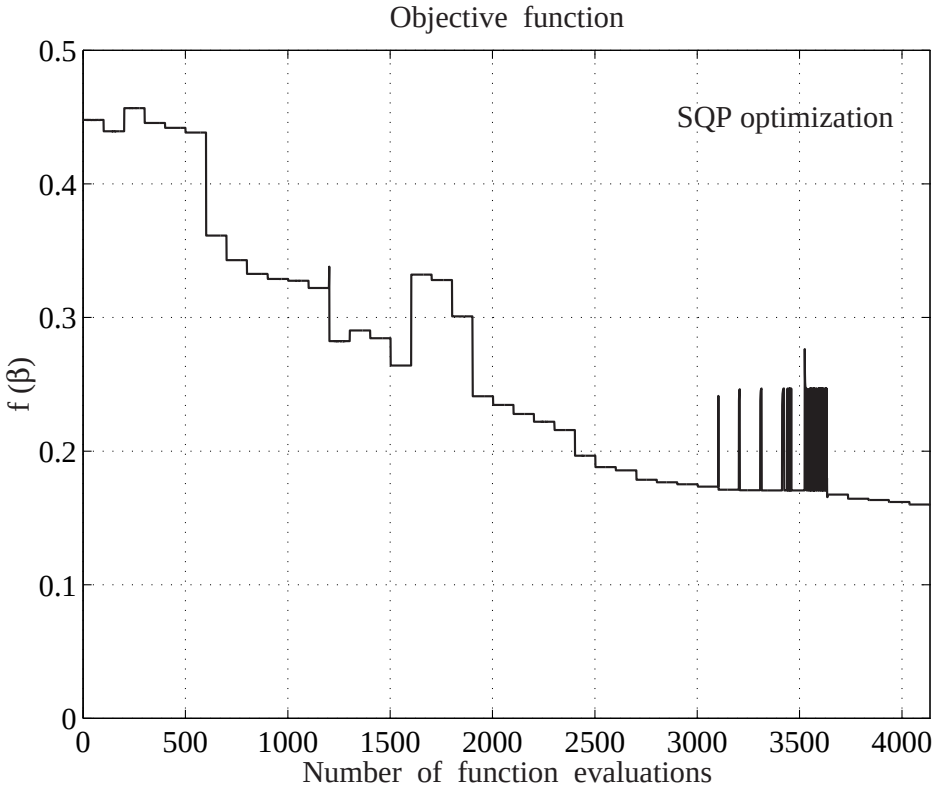

Figure 6.16: Example 2: Minimization of objective function defined in Eq. (6.6) with SQP method.

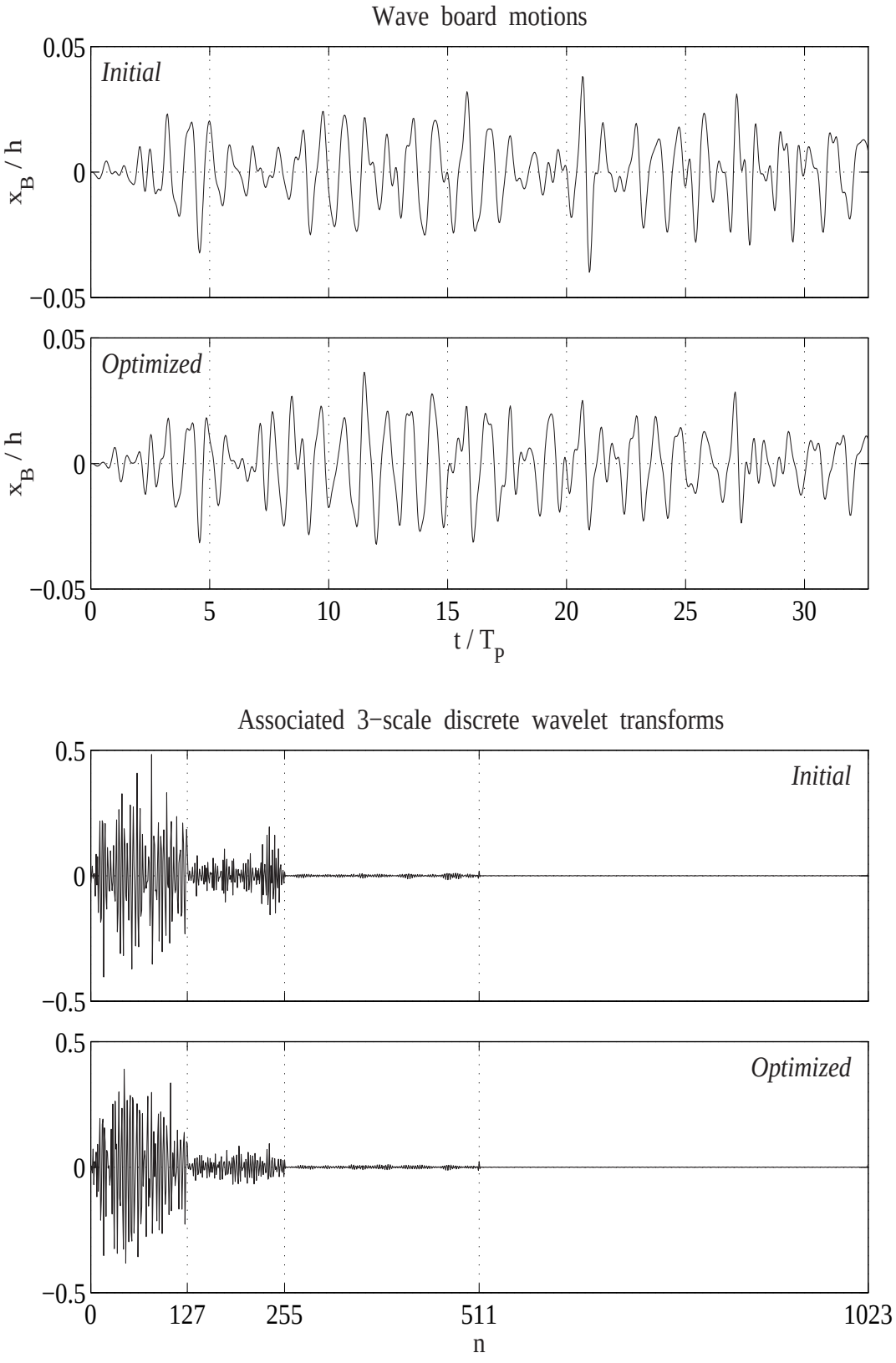

Figure 6.17: Example 2: Initial and SQP-optimized wave board motion with associated discrete wavelet transforms.

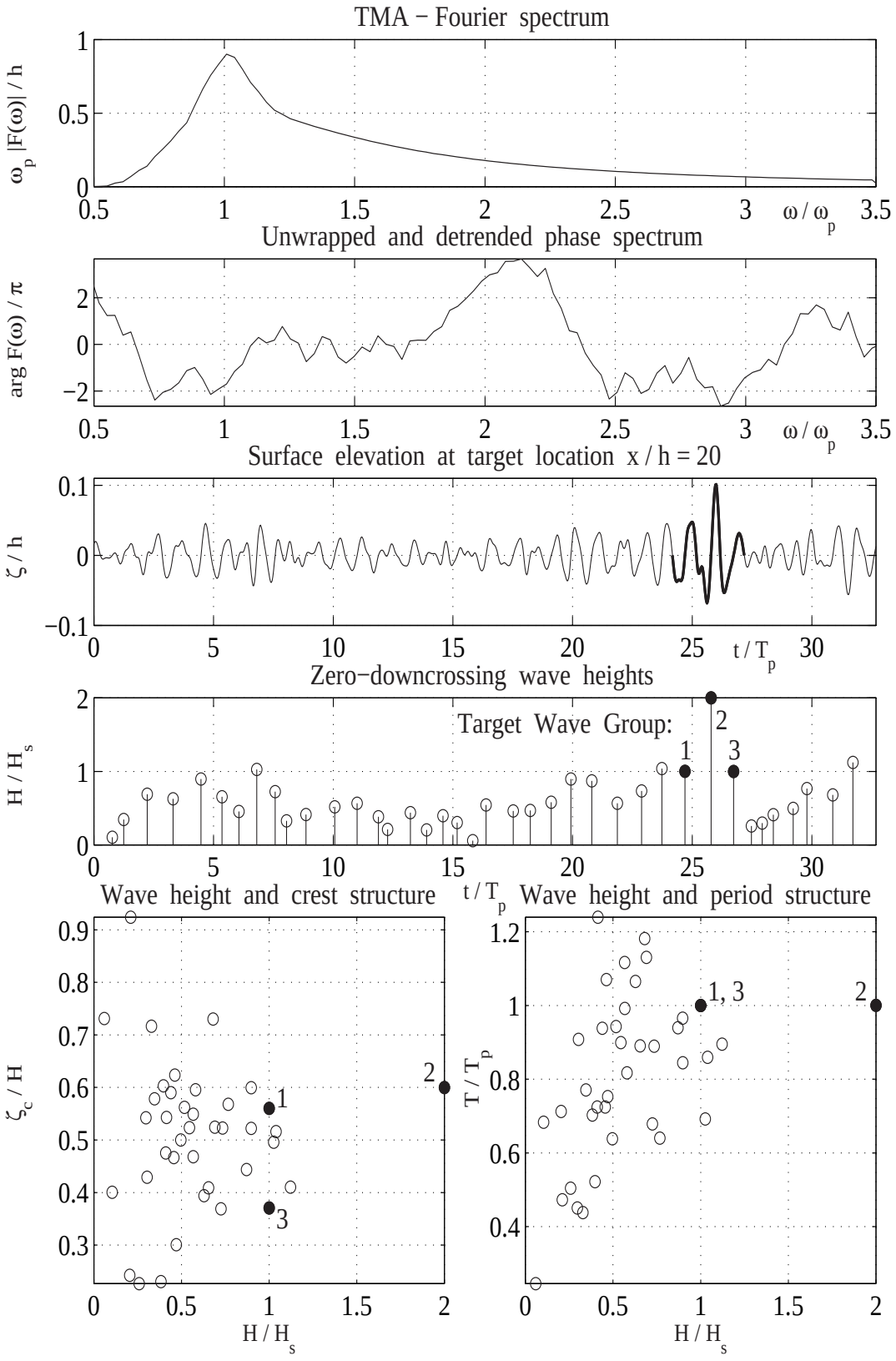

Figure 6.18: Example 2: Characteristics of linear wave train with synthesized wave group.

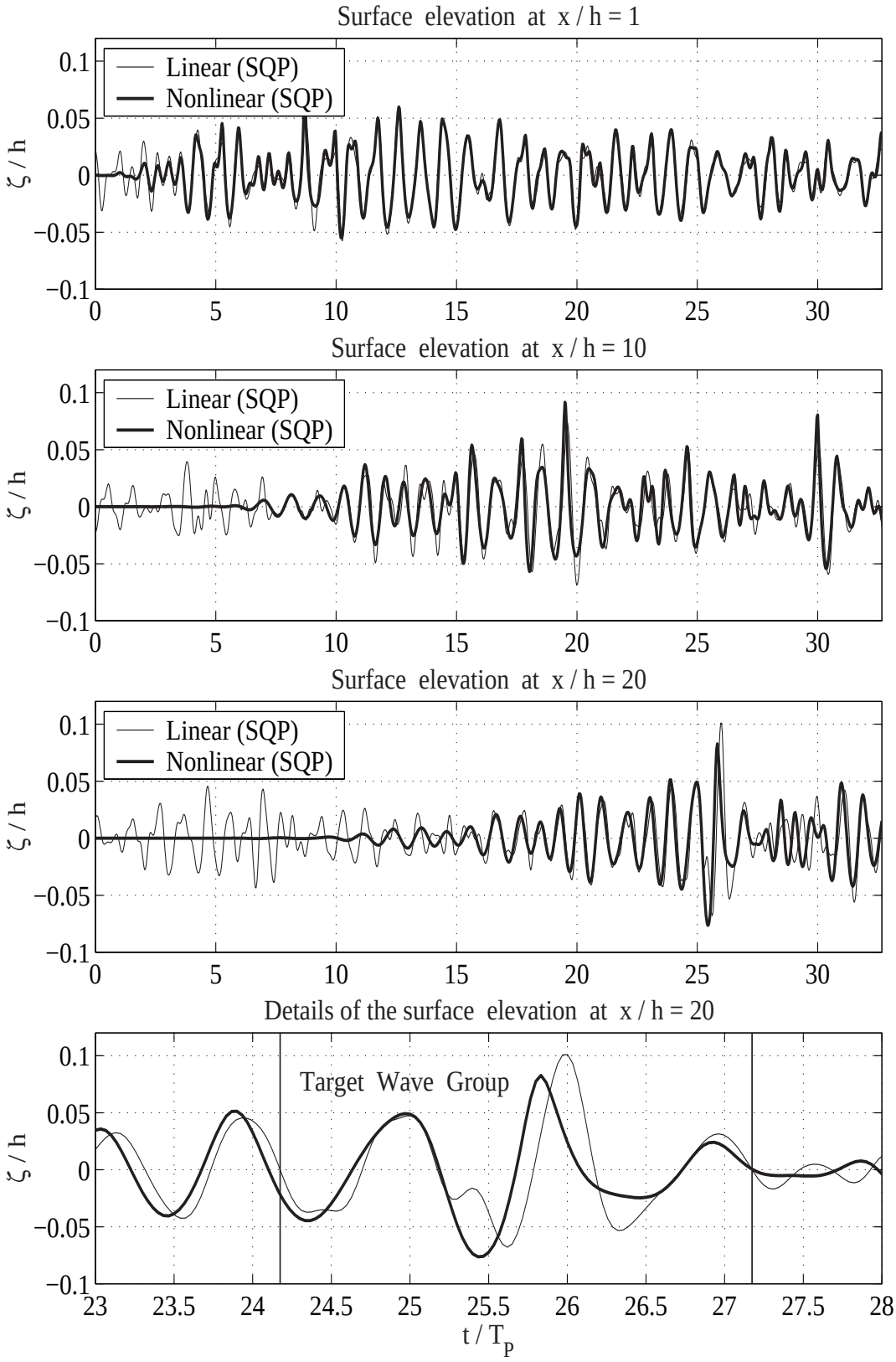

Figure 6.19: Example 2: Comparison of linear and nonlinear evolution of synthesized wave group. Wave board motion used in nonlinear simulation generated with SQP method.

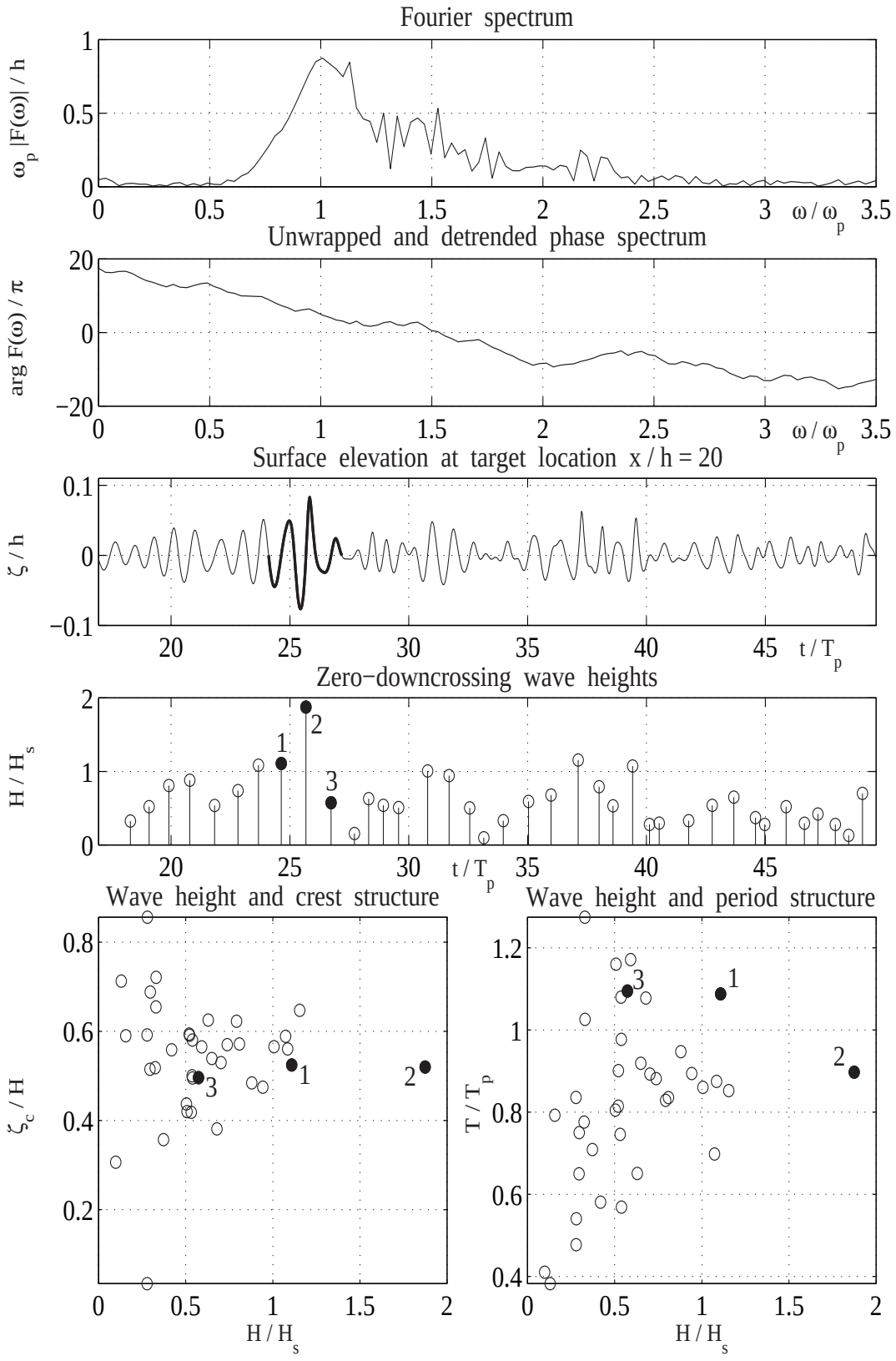

Figure 6.20: Example 2: Further characteristics of nonlinear wave train with synthesized wave group. Wave board motion used in nonlinear simulation generated with SQP method.

6.3.2 Generation of Nonlinear Target Wave Train

The characteristics of the nonlinear wave train are improved with the subplex method. As in the first example, the free variables in the optimization are selected to be the $n = 51$ wavelet coefficients $\boldsymbol{c} = (c_{38}, c_{39}, \ldots, c_{88})^T$, which correspond to the time window between $t/T_p = 9.6$ and $t/T_p = 22.4$ of the wave board motion. The fitting problem is defined for the wave group as:

$$\begin{aligned}\underset{\boldsymbol{c}\in\Re^n}{\text{minimize}}\ f(\boldsymbol{c}) \;=\; & \left(\frac{H_{i-1}-H_{1,\,target}}{H_{1,\,target}}\right)^2 + \left(\frac{T_{i-1}-T_{1,\,target}}{T_{1,\,target}}\right)^2 + \\ & \left(\frac{H_{i}-H_{2,\,target}}{H_{2,\,target}}\right)^2 + \left(\frac{T_{i}-T_{2,\,target}}{T_{2,\,target}}\right)^2 + \left(\frac{\zeta_{c,\,i}-\zeta_{c,\,target}}{\zeta_{c,\,target}}\right)^2 + \\ & \left(\frac{t_{\zeta_c,\,i}-t_{\zeta_c,\,target}}{t_{\zeta_c,\,target}}\right)^2 + \left(\frac{H_{i+1}-H_{3,\,target}}{H_{3,\,target}}\right)^2 + \left(\frac{T_{i+1}-T_{3,\,target}}{T_{3,\,target}}\right)^2 + \\ & \left(\frac{\sigma\big(x_B(t)\big)-\sigma\big(x_B(t)_{initial}\big)}{\sigma\big(x_B(t)_{initial}\big)}\right)^2 \end{aligned} \tag{6.8}$$

$$\begin{aligned}\text{subject to}\quad g_1 &= \max\Big\{|x_B(t)|\Big\} - x_{max} \;\le\; 0,\\ g_2 &= \max\Big\{|\dot{x}_B(t)|\Big\} - u_{max} \;\le\; 0,\\ g_3 &= \max\Big\{|\ddot{x}_B(t)|\Big\} - a_{max} \;\le\; 0.\end{aligned} \tag{6.9}$$

The minimization of the objective function $f(\boldsymbol{c})$ is shown in Fig. 6.21. The straight vertical lines indicate infeasible points due to wave breaking or constraint violation. The subplex fitting terminates successfully at $4.9 \cdot 10^{-3}$ after 2034 function evaluations.

The improved wave board motion and the associated nonlinear wave evolution are presented in Figs. 6.22 and 6.23. The final wave train now correlates much better to the target parameters; particularly the height of the third wave is considerably increased. As shown in Table 6.7, the maximum deviation is 3.7 % for the asymmetry ζ_c/H of the high transient wave in the center of the group. Fig. 6.24 presents the Fourier and phase spectrum as well as wave height, crest and period structure determined by a zero-downcrossing analysis.

The smoothed variance spectra are shown in Fig. 6.25 for different locations in the wave tank. The zeroth spectral moment $m_0 = 0.0109$ and the peak period $T_p = 3.01\,s$ differ slightly from the target values at the target location $x/h = 20$. Fig. 6.26 shows that the energy flux is mostly focused at the

Wave 1:	$H\,/\,H_s$	$T\,/\,T_p$		
Target value	**1.000**	**1.000**		
SQP value	1.107	1.087		
Deviation in %	10.7	8.7		
Subplex value	0.996	1.029		
Deviation in %	−0.4	2.9		
Wave 2:	$H\,/\,H_s$	$T\,/\,T_p$	$\zeta_c\,/\,H$	$t_{\zeta_c}\,/\,T_p$
Target value	**2.000**	**1.000**	**0.600**	**26.000**
SQP value	1.874	0.898	0.520	25.832
Deviation in %	−6.3	−10.2	−13.3	−0.7
Subplex value	2.048	0.983	0.578	25.810
Deviation in %	2.4	−1.7	−3.7	−0.7
Wave 3:	$H\,/\,H_s$	$T\,/\,T_p$		
Target value	**1.000**	**1.000**		
SQP value	0.574	1.096		
Deviation in %	−42.6	9.6		
Subplex value	0.997	1.008		
Deviation in %	−0.3	0.8		

Table 6.7: Conformity of the nonlinear synthesized wave group with target parameters.

target location in space and time. The evolution of the subplex-fitted nonlinear transient wave in space and time is presented in Fig. 6.27. At $t/T_p = 26$ the steepness of the three target waves is $H_1/L_1 = 0.026$, $H_2/L_2 = 0.050$ and $H_3/L_3 = 0.046$. Note that zero-downcrossing waves in time domain correspond to zero-upcrossing waves in space domain and vice versa. The associated distributions of the horizontal particle velocity, acceleration and dynamic pressure are shown in Fig. 6.28. The long waves dominate the flow field down to the bottom of the wave tank, but the magnitude of velocity, acceleration and dynamic pressure decreases exponentially with water depth. The maximum zero-upcrossing crest and wave height, as well as wave steepness, are presented in Fig. 6.29. The entire wave tank is analyzed to obtain these values. Hence they do not correlate to a particular wave which is traced

in time. Occasionally steep waves are observed.

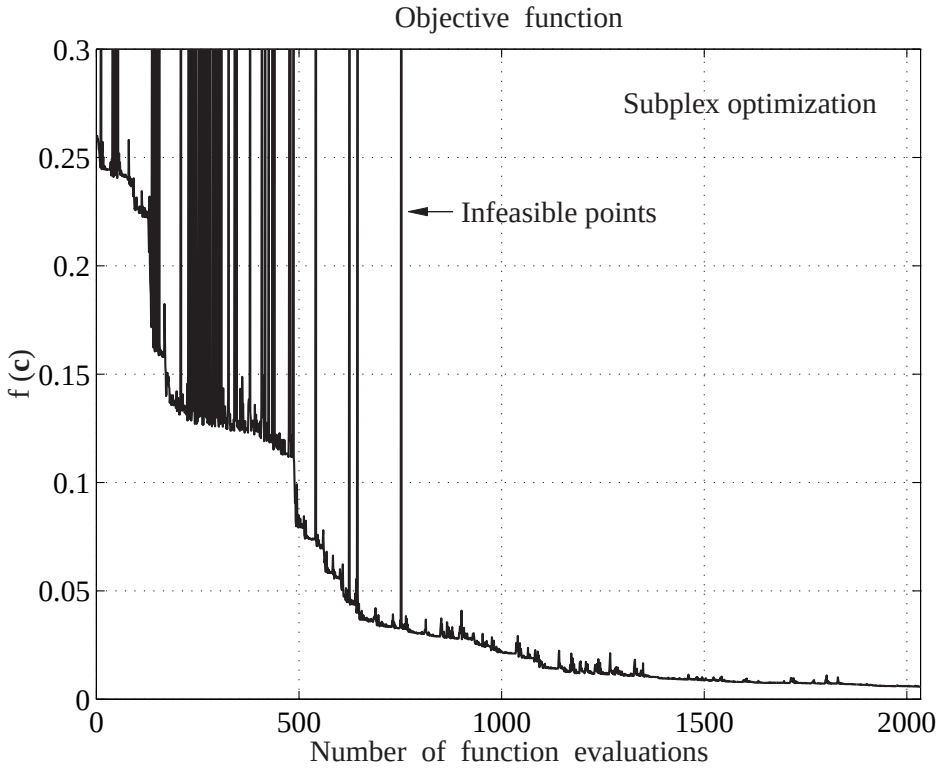

Figure 6.21: Example 2: Minimization of objective function defined in Eq. (6.8) with Subplex method.

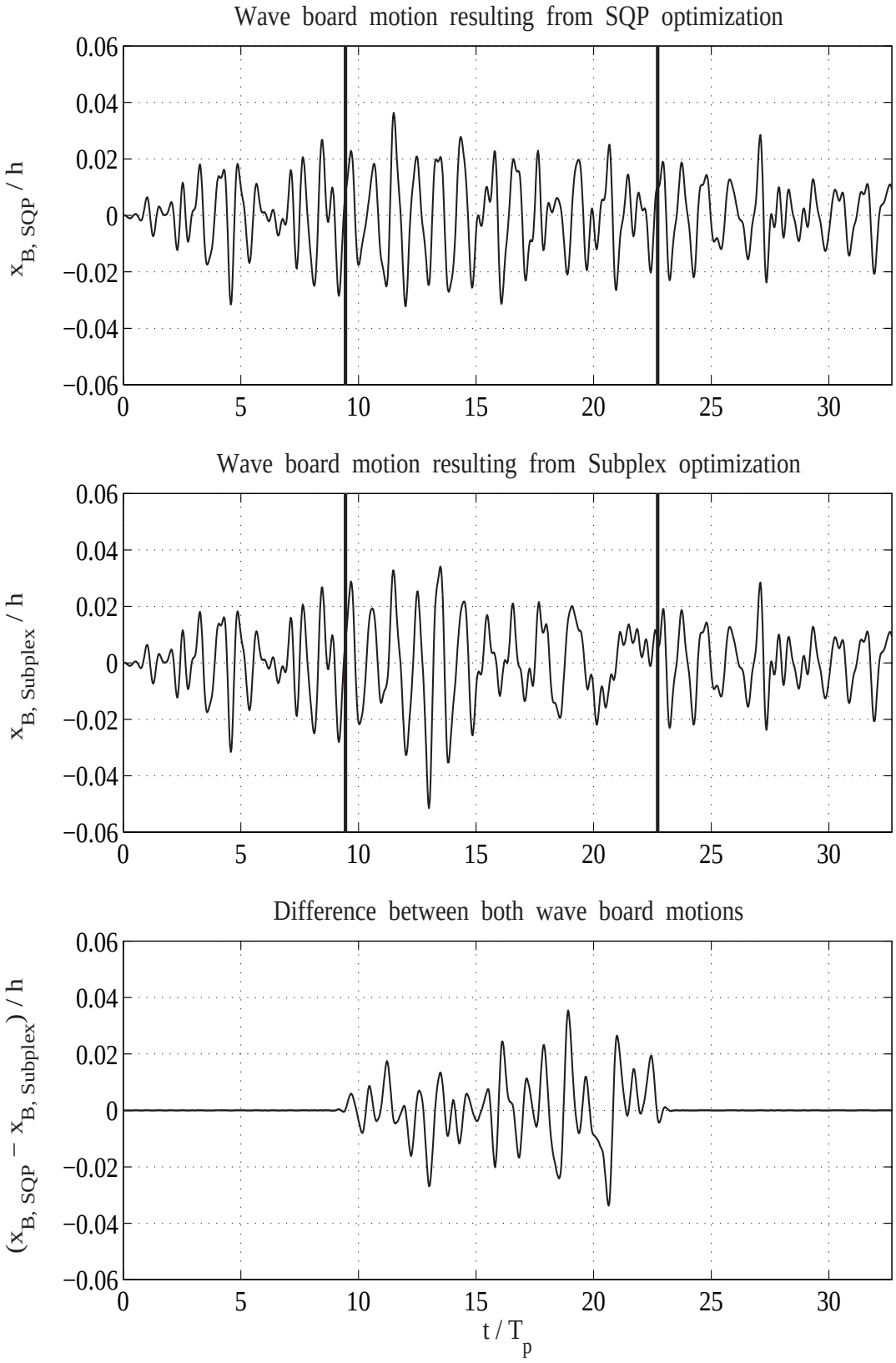

Figure 6.22: Example 2: Comparison of wave board motions generated with SQP and Subplex method.

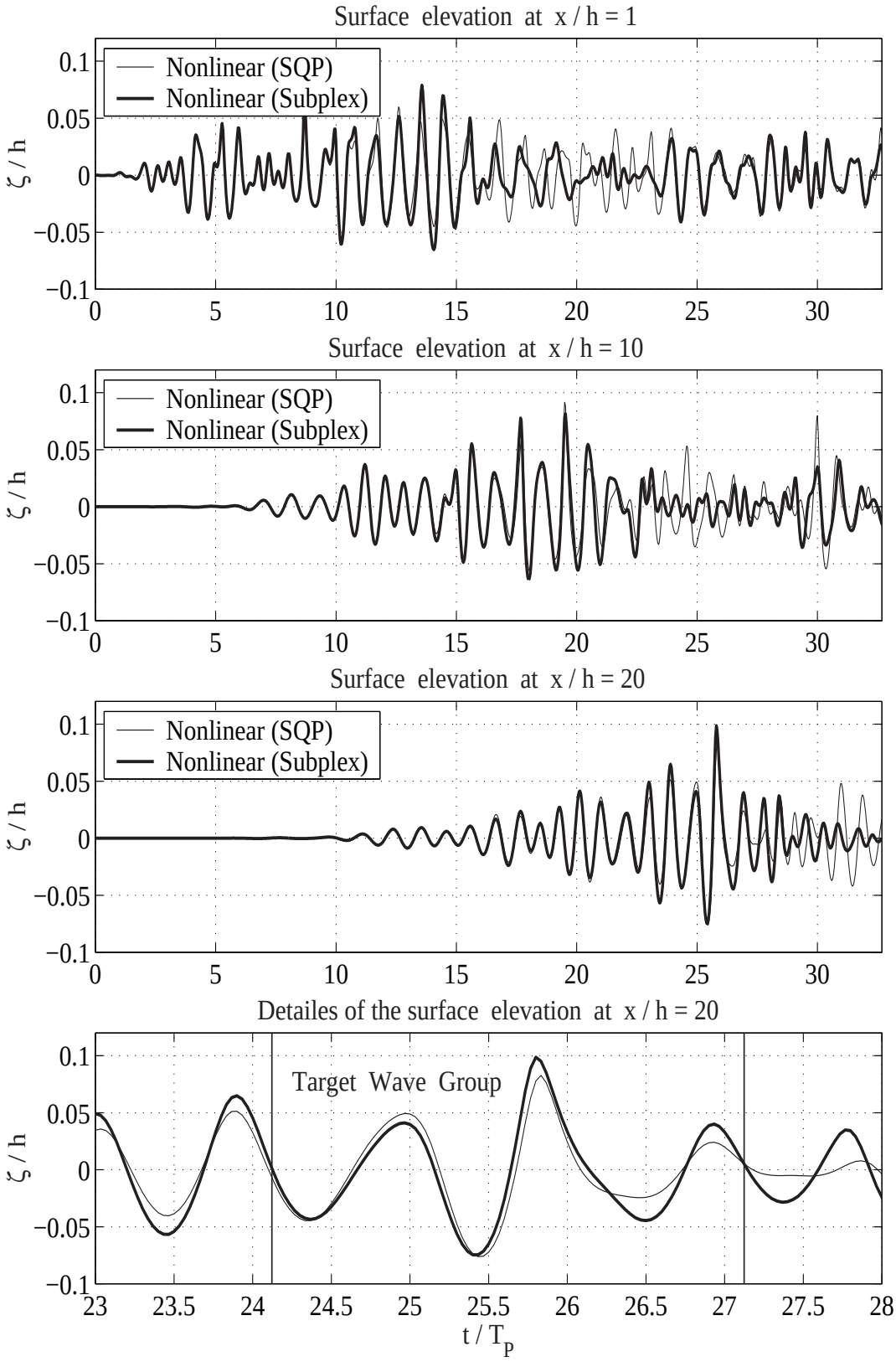

Figure 6.23: Example 2: Comparison of nonlinear evolution of synthesized wave groups. Wave board motion used in nonlinear simulations generated with SQP and Subplex method.

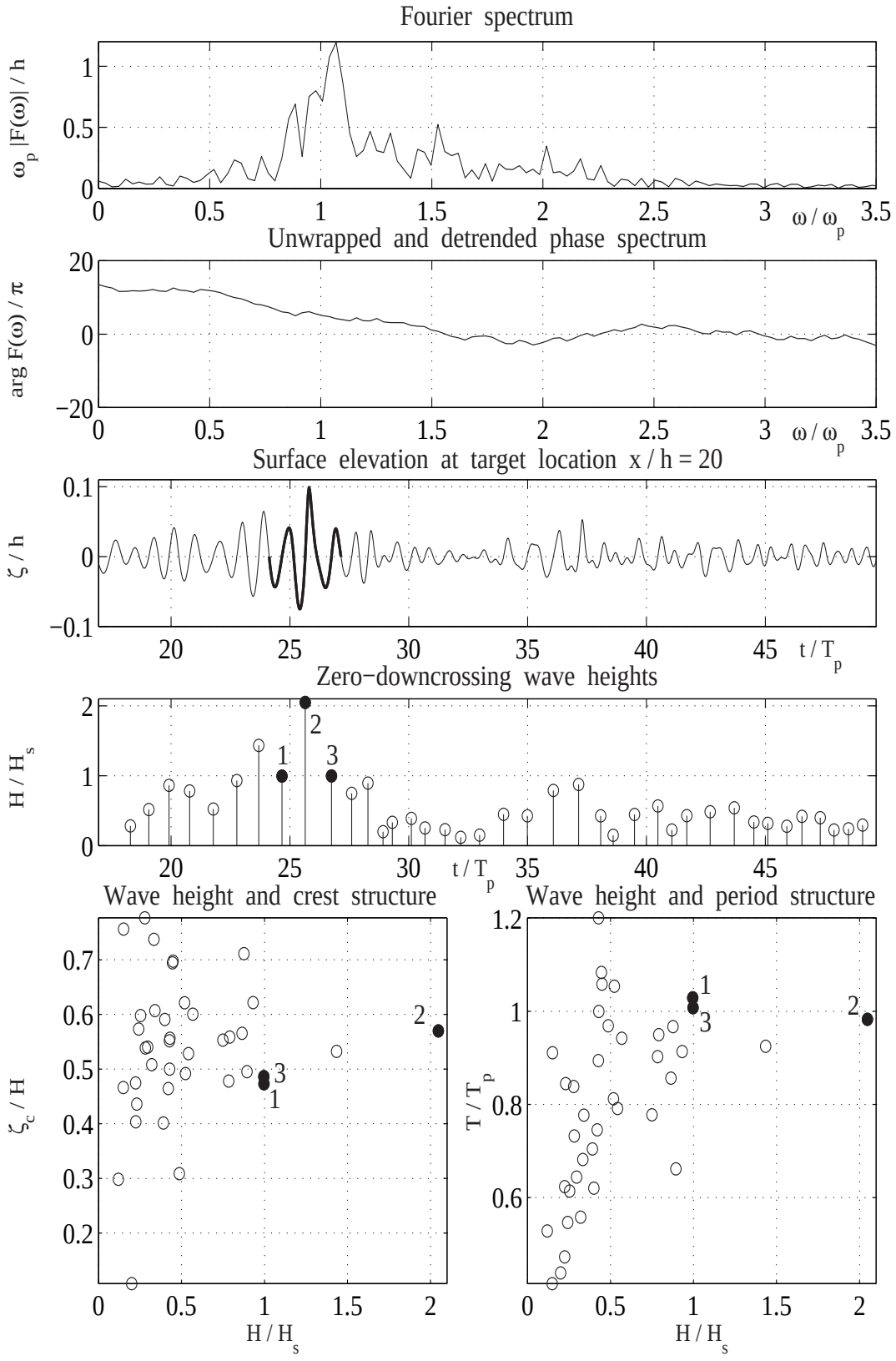

Figure 6.24: Example 2: Further characteristics of nonlinear wave train with synthesized wave group. Wave board motion used in nonlinear simulation generated with Subplex method.

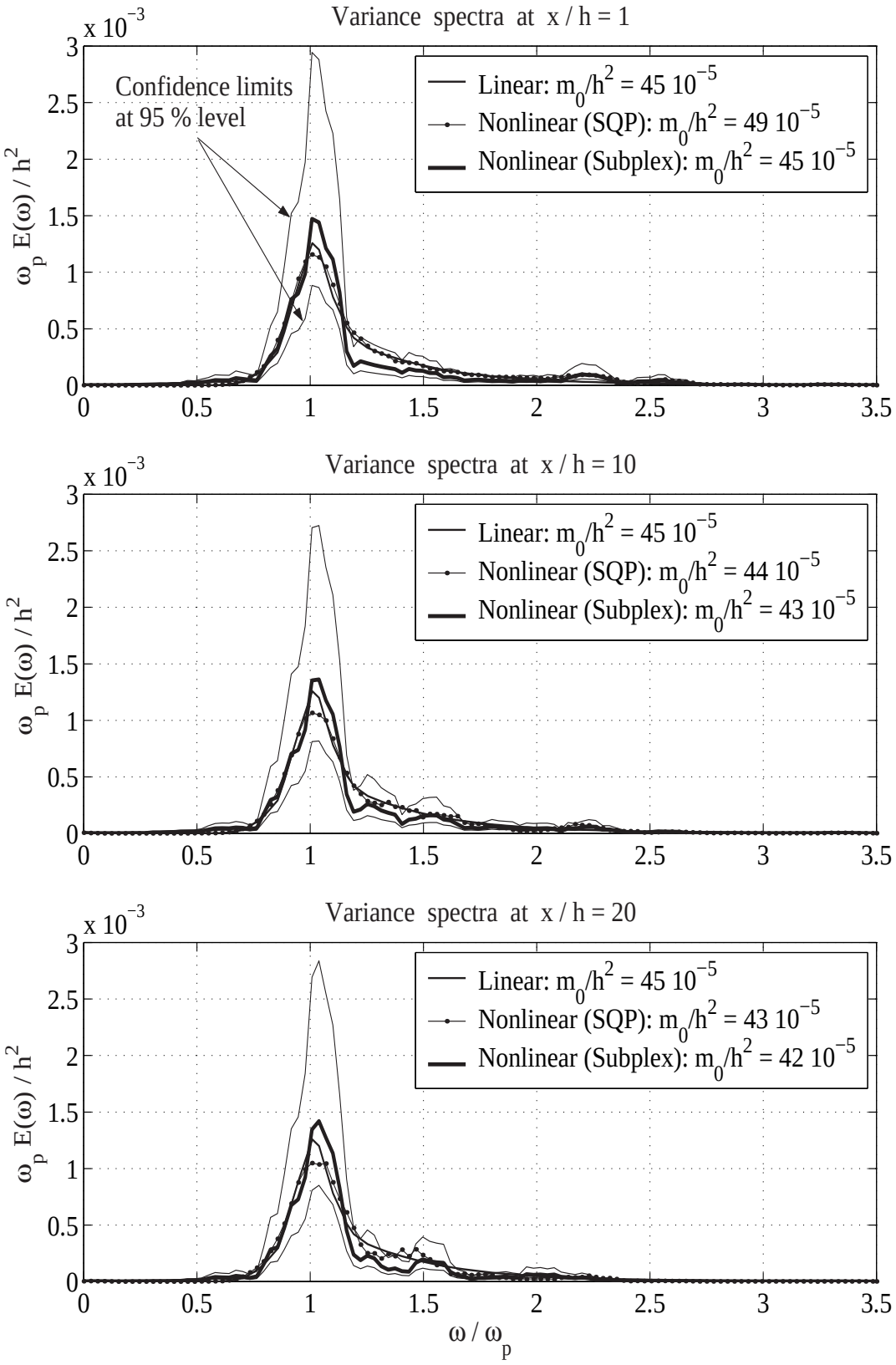

Figure 6.25: Example 2: Variance spectra of linear and nonlinear wave trains at different locations.

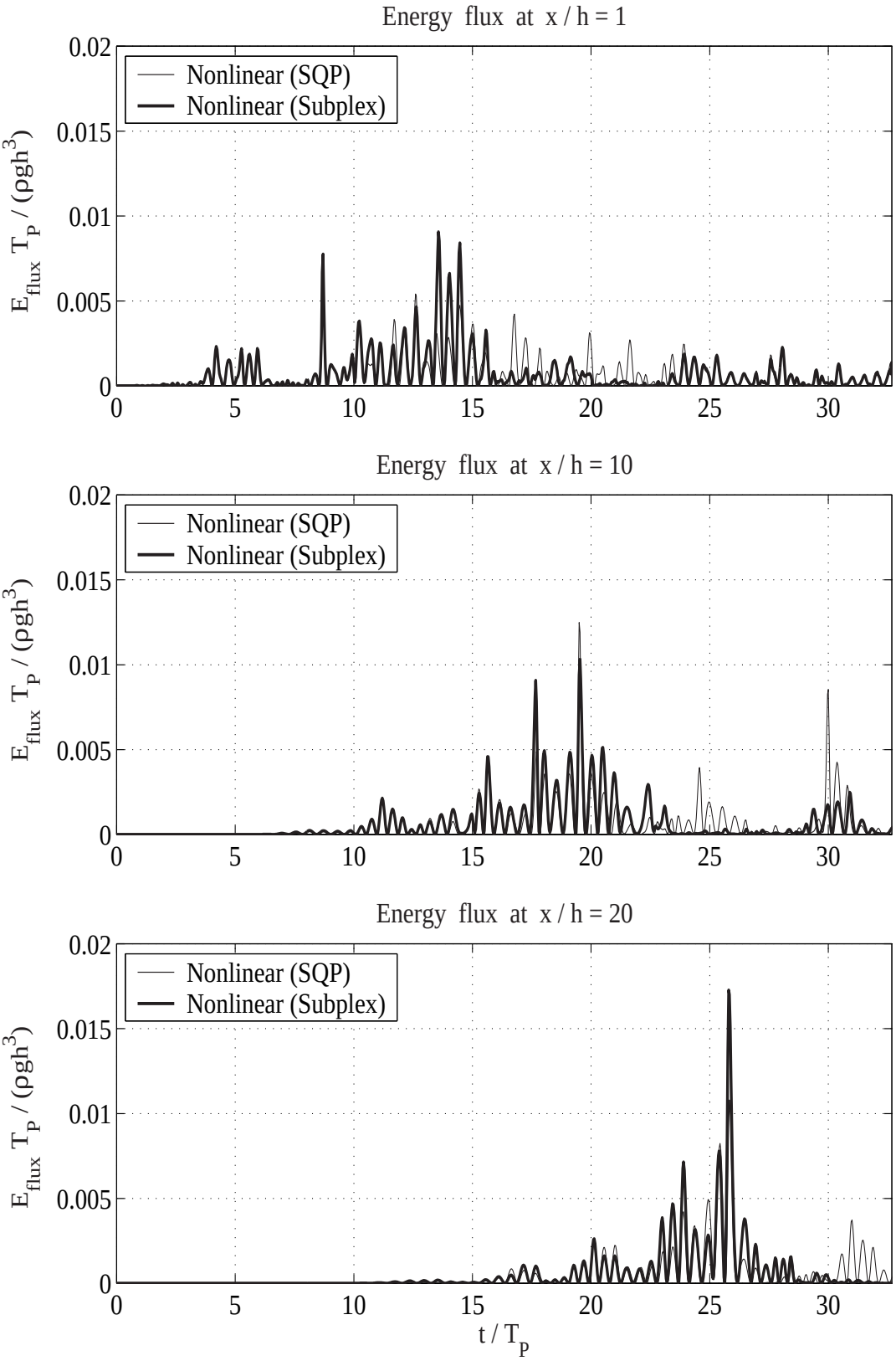

Figure 6.26: Example 2: Energy flux of linear and nonlinear wave trains at different locations.

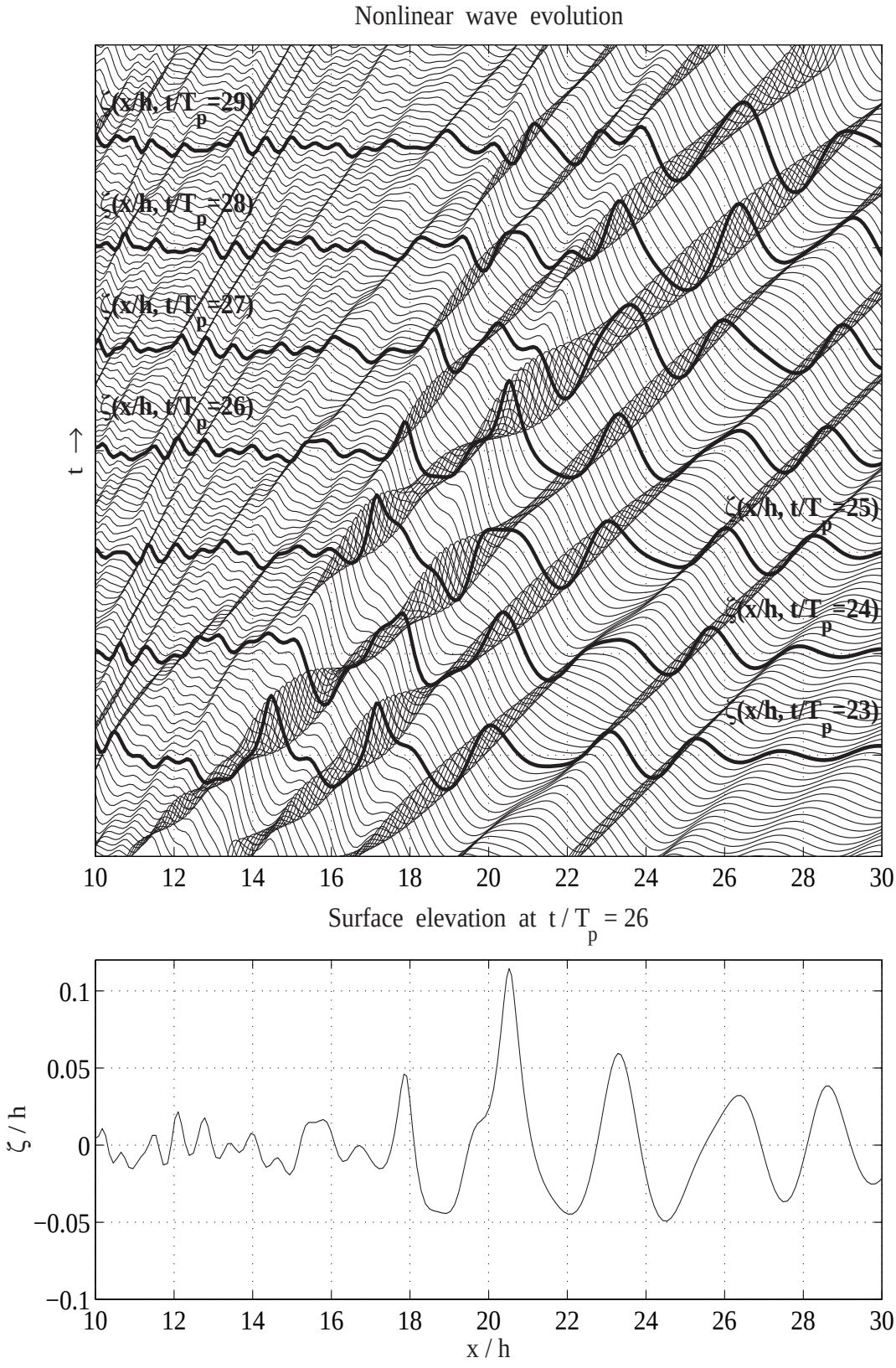

Figure 6.27: Example 2: Evolution of nonlinear synthesized wave group in space and time domain. Wave board motion used in nonlinear simulation generated with Subplex method.

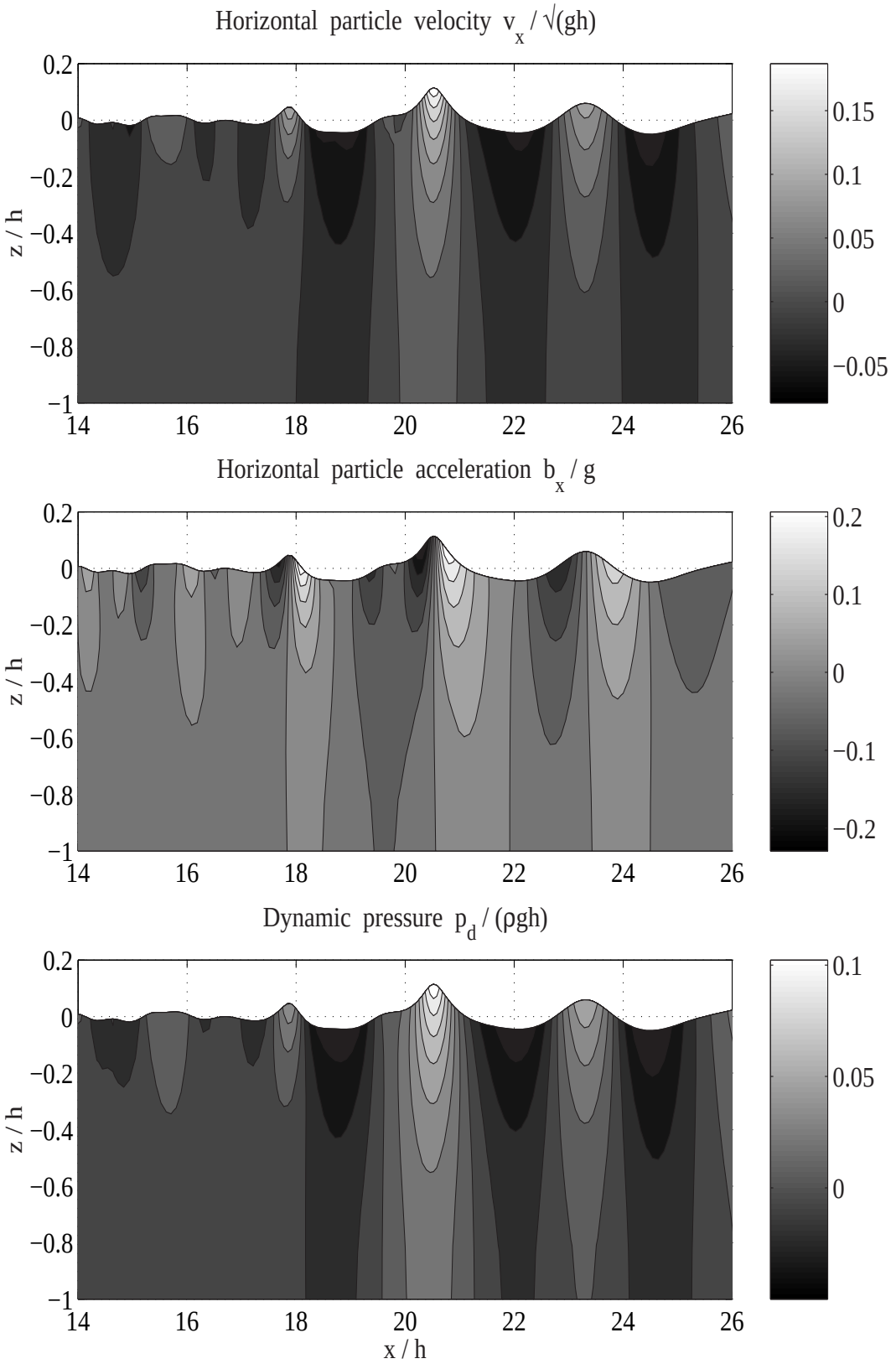

Figure 6.28: Example 2: Particle velocity, acceleration, and dynamic pressure field of nonlinear wave train with synthesized wave group at $t/T_p = 26$. Wave board motion used in nonlinear simulation generated with Subplex method.

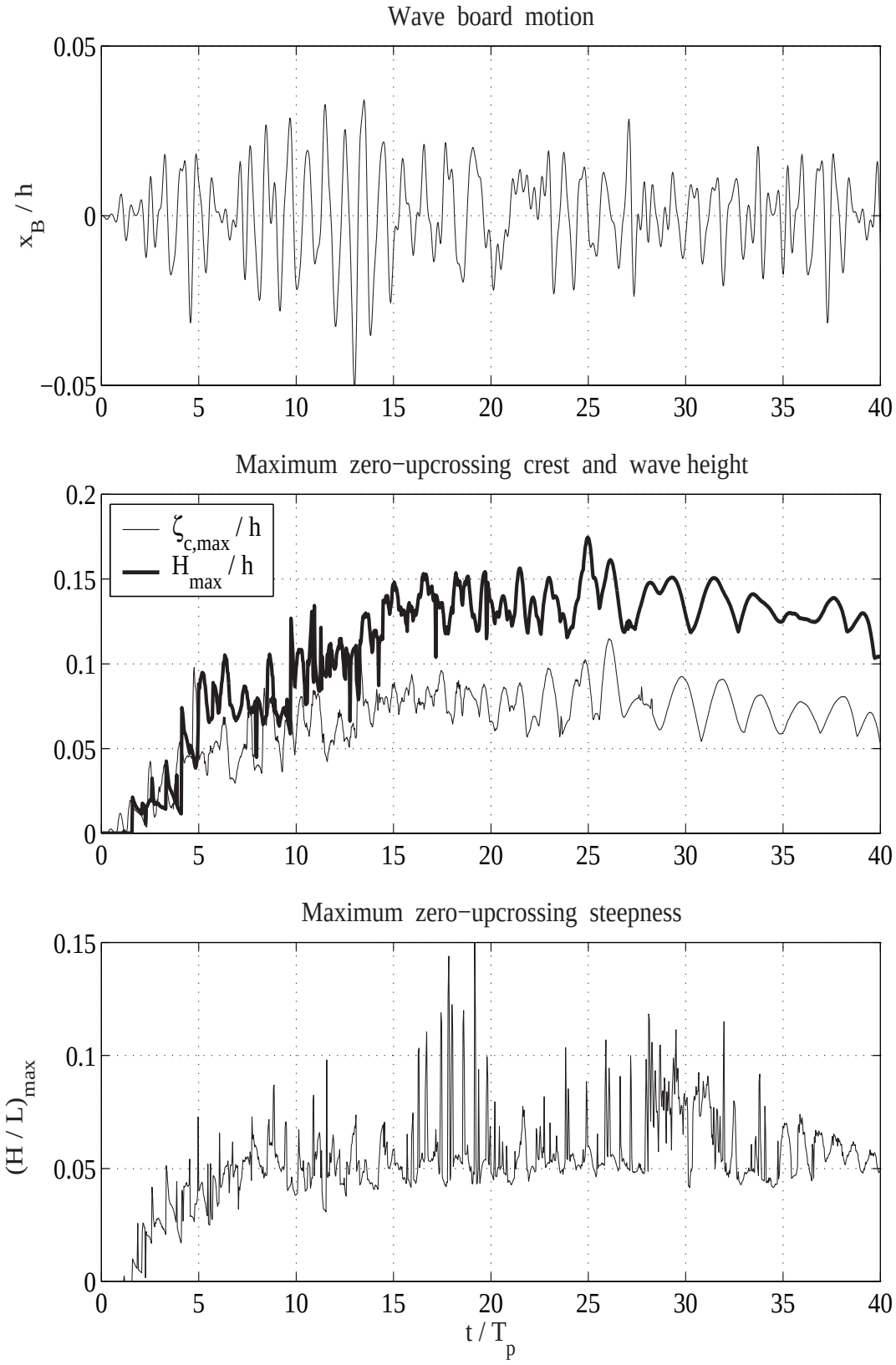

Figure 6.29: Example 2: Zero-upcrossing characteristics of nonlinear wave train with synthesized wave group. Wave board motion used in nonlinear simulation generated with Subplex method.

Chapter 7

Conclusions

This thesis presents a new procedure for the computer-aided synthesizing of nonlinear transient waves in random seas. Modern numerical techniques of computational fluid dynamics, nonlinear programming and digital signal processing are successfully combined to synthesize extreme single waves and wave groups with the stochastic wave field for global and local target characteristics. The examples presented demonstarte the high quality of the generated wave trains and hence the effectiveness of this new approach.

Basically, the procedure is based on two steps where first linear wave theory is applied to derive a qualified initial guess for the subsequent fitting of the nonlinear wave evolution. Due to the multi-modal nature of the associated constrained minimization problems, both optimization methods involved may only converge to local minima which depend on the initial conditions.

In some cases it may be sufficient to optimize only the linear wave train, determine the wave board motion and numerically simulate the nonlinear wave train, which deviates to some extent from the target characteristics. This approach is much faster, since the values of the objective function and the constraints are easy to calculate in the case of linear wave theory.

To decrease the high computer costs associated with the fitting of the nonlinear wave train, the number of free variables in the minimization problem is significantly reduced by introducing the discrete wavelet transform. Future extensions of this study may include research on other signal decomposition techniques to further decrease the domain space of the fitting problem.

The computer program for simulating the nonlinear wave evolution in the numerical wave tank is based on the mixed Euler-Lagrange formulation of the nonlinear initial boundary value problem, where the Laplace equation is solved for Neumann and Dirichlet boundary conditions by the finite element method. It can easily be substituted by other programs based on the

boundary element method or finite volume method. If wave breaking needs to be considered, it might be interesting to couple these methods with procedures for solving the Reynolds averaged Navier-Stokes equations (RANSE) to account for the viscosity of the fluid.

The time-consuming fitting procedure is well-suited for parallelization on multi-processor systems, since many numerical simulations can run independently at the same time. The parallelization would speed up the solution process considerably and is a necessary prerequisite for optimizing nonlinear wave trains with breaking waves, as well as three-dimensional nonlinear wave fields, to account for the influence of wave direction on the evolution of extreme waves.

The standard deviation of the wave board motion is part of the objective function in the fitting procedure. Hence, only the total energy input into the numerical wave tank is controlled but not the shape of the variance spectrum itself. It would be desirable, in the future, to consider all global target characteristics of the sea spectrum as well.

The new procedure is a very usable multi-purpose analysis and development tool for performing detailed experimental and numerical investigations of extreme wave events in random seas. The optimized wave trains can be utilized, for instance, to derive appropriate design wave conditions for many different marine structures.

Nomenclature

$\boldsymbol{A}$		Positive definite coefficient matrix
$\boldsymbol{B}$	m^2/s	Vector of the forcing terms
$B(t)$	m^2/s^2	Bernoulli constant
C	m/s	Wave celerity
Cn		Courant number $Cn = (\pi g \Delta t^2)/(8\Delta x)$
$E(\omega)$	$m^2\,s$	Variance spectrum $E(\omega) = E(f)/(2\pi) = E(q)/\omega_p$
$\dot{E}(x,t)$	N/s	Energy flux per unit length of crest
$E_{kin}(t)$	N	Kinetic energy per unit length of crest
$E_{pot}(t)$	N	Potential energy per unit length of crest
$E_{total}(t)$	N	Total energy per unit length of crest
$\boldsymbol{F}$	m/s, m^2/s^2	Time-derivative of the free surface state matrix
$F(\omega)$	$m\,s$	Fourier transform
$F_{hydro}(\omega)$	$m\,s$	Fourier transform of hydrodynamic transfer function
$F_{target}(\omega)$	$m\,s$	Fourier transform of linear target wave train
$F_{trans}(\omega)$	$m\,s$	Fourier transform of spatial translates
$\mathcal{G}$		Lowpass reduction operator
$\mathcal{G}^*$		Lowpass reconstruction operator
$\boldsymbol{H}$		Hessian matrix of the Lagrangian function
H	m	Wave height
H_s	m	Significant wave height $H_s = 4\sqrt{m_0}$
$\mathcal{H}$		Highpass reduction operator
$\mathcal{H}^*$		Highpass reconstruction operator
K		Number of discrete data points of the wave board motion
L	m	Wave length
$L_\psi(a,b)$	m	Wavelet transform
$\mathcal{L}(\boldsymbol{x},\boldsymbol{\lambda})$		Lagrangian function
M		Scale of discrete wavelet transform
$\mathcal{M}(\boldsymbol{x})$		Merit function

N		Number of discrete data points of the wave train
N_i		Shape function
$NX+1$		Number of horizontal grid nodes
$NZ+1$		Number of vertical grid nodes
$\mathbb{N}$		Set of natural numbers
$\mathbb{R}$		Set of real numbers
$\boldsymbol{S}$	m, m^2/s	Free surface state matrix
T	s	Wave period
$\bar{T}$	s	Mean period
T_p	s	Peak period
T_z	s	Zero-crossing period
V_n	m	nth subspace
a		Wavelet scaling coefficient
a_{max}	m/s^2	Maximum acceleration of the wave board
b	s	Wavelet translation coefficient
$\boldsymbol{c}$		Vector of scaling function expansion coefficients
c		Scaling function expansion coefficients
c_ψ	m^2s^2	Wavelet admission coefficient
d		Wavelet function expansion coefficients
$\boldsymbol{e}$		Unit vector of the domain space
$\boldsymbol{f}$	m/s^2	Vector of the body force per unit mass
f	$1/s$	Frequency
$\bar{f}$	$1/s$	Mean frequency
f_p	$1/s$	Peak frequency
f_z	$1/s$	Zero-crossing frequency
f_{NY}	$1/s$	Nyquist frequency $f_{NY} = 1/(2\Delta t)$
$f(\boldsymbol{x})$		Objective function
$\boldsymbol{g}(\boldsymbol{x})$		Vector of the constraints
g	m/s^2	Gravitational acceleration
g_*		Highpass filter coefficients
h	m	Water depth
h_*		Lowpass filter coefficients
k	$1/m$	Wave number
l	m	Tank length
l_{beach}	m	Length of numerical beach
$\dot{m}(x,t)$	kg/s	Mass flux

m_n	m^2/s^n	nth spectral moment about zero frequency
m_0	m^2	Variance $m_0 = \sigma^2$
n		Degree of freedom
n_s		Number of subspaces
n_{smin}		Minimum subspace dimension
n_{smax}		Maximum subspace dimension
$p(x, z, t)$	N/m^2	Absolute pressure
p_a	N/m^2	Atmospheric pressure
$p_d(x, z, t)$	N/m^2	Dynamic pressure
q		Normalized frequency $q = \omega/\omega_p = f/f_p$
$\boldsymbol{r}$		Vector of the penalty parameters
t	s	Time
u		Confidence level
Δt	s	Time step
u_{max}	m/s	Maximum velocity of the wave board
$u(x, z, t)$	m/s	Horizontal velocity
$\boldsymbol{v}(x, z, t)$	m/s	Velocity vector
$w(x, z, t)$	m/s	Vertical velocity
$\boldsymbol{x}$		Vector of the design parameters
$\boldsymbol{x}_l$		Vector of the lower parameter bounds
$\boldsymbol{x}_u$		Vector of the upper parameter bounds
x	m	Cartesian coordinate in the physical plane
$x_B(t)$	m	Horizontal wave board motion
$\dot{x}_B(t)$	m/s	Horizontal wave board velocity
x_{max}	m	Maximum stroke of the wave board
Δx	m	Horizontal grid spacing
$\widetilde{\Delta x}$		Vector of progress in subplex optimization
z	m	Cartesian coordinate in the physical plane
Δz	m	Vertical grid spacing
Ω		Fluid domain
Γ		Boundary of the fluid domain
Γ_B		Boundary defined by the wave board
Γ_S		Boundary defined by the free surface
Γ_W		Boundary defined by the fixed tank walls
α		Spectral Phillips coefficient

α_s		Reflection coefficient in simplex optimization
α_z		Exponential vertical narrowness of the gird nodes
$\boldsymbol{\beta}$		Vector of phase values to be optimized
β		Phase value
β_s		Contraction coefficient in simplex optimization
γ		Jonswap peak enhancement factor
γ_s		Expansion coefficient in simplex optimization
δ_s		Shrinkage coefficient in simplex optimization
$\zeta(x,t)$	m	Free surface elevation
ζ_a	m	Wave amplitude
ζ_c	m	Wave crest height
η	m	Cartesian coordinate in the computational plane
$\boldsymbol{\lambda}$		Vector of the Lagrangian multipliers
$\boldsymbol{\mu}$		Vector of the stepsizes in subplex optimization
$\mu(x)$	$1/s$	Damping coefficient
μ_n	m^2/s^n	nth spectral moment about mean frequency
ν	m^2/s	Kinematic viscosity
ξ	m	Cartesian coordinate in the computational plane
ρ	kg/m^3	Mass density
σ	m	Standard deviation
σ_*	m	Spectral width parameter
$\boldsymbol{\phi}$	m^2/s	Vector of the potential values at the grid nodes
$\phi(x,z,t)$	m^2/s	Velocity potential
ψ_s		Simplex reduction coefficient in subplex optimization
$\psi(t)$	m	Wavelet function
$\Psi(\omega)$	$m\,s$	Fourier spectrum of wavelet function
$\varphi(t)$	m	Scaling function
ω	rad/s	Frequency $\omega = 2\pi f$
$\bar{\omega}$	rad/s	Mean frequency $\bar{\omega} = m_1/m_0$
ω_p	rad/s	Peak frequency $\omega_p = (\int \omega\, E^P(\omega)\, d\omega)/(\int E^P(\omega)\, d\omega)$
ω_s		Step reduction coefficient in subplex optimization
ω_z	rad/s	Zero-crossing frequency $\omega_z = (m_2/m_0)^{1/2}$
ω_{beach}	rad/s	Strength of numerical beach
$\Delta\omega$	rad/s	Frequency resolution
∇		Gradient operator vector
$\|\cdot\|_n$		n-norm

Acknowledgements

The author thanks Rolf Habel and Gunner Koether profusely for experimentally investigating a transient wave synthesized in a random sea, which is used for the validation of numerical calculations. The measurements were performed in 1999 at the Large Wave Tank (GWK) Hannover in the frame of the research program *'Unterwasser-Filtersysteme zur Wellendämpfung'* sponsored by the German Federal Ministry of Education and Science, Research and Technology (BMBF). This project was a joint venture of TU Braunschweig, Leichtweiss-Institut für Wasserbau and TU Berlin, Institut für Schiffs- und Meerestechnik.

The discrete wavelet transform is determined in this study with a routine of the wavelet toolbox Uvi_Wave 3.0 (1996) developed at the University of Vigo by Santiago González Sánchez, Nuria González Prelcic and Sergio J. Garcia Galán. Uvi_Wave 3.0 is free software for use with MATLAB[1] and is distributed under the terms of the GNU General Public License as published by the Free Software Foundation.

A routine of the MATLAB optimization toolbox is applied to optimize the linear wave train with the sequential quadratic programming method. The subplex fitting of the nonlinear wave train is based on a software package developed in Fortran 77 by Thomas Harvey Rowan as part of his doctoral thesis at the University of Texas at Austin. In this work, the MATLAB version is applied, which was coded by Bruce Lowekamp, Mathematical Sciences Section at Oak Ridge National Laboratory.

[1]MATLAB® Numeric Computing Environment, Version 5, Registered Trademark of The Math Works, Inc., Natick, USA

Bibliography

Airy, G. (1849). Tides and waves. In Anon (Ed.), *Encyclopaedia Metropolitania*, pp. 241–396. J.J. Griffin, London. Re-issue, initially published in 1845.

Båth, M. (1974). *Spectral Analysis in Geophysics*. Elsevier, Amsterdam.

Baldock, T. and Swan, C. (1994). Numerical calculations of large transient water waves. *Applied Ocean Research*, 16(2):101–112.

Bazaraa, M., Sherali, H. and Shetty, C. (1993). *Nonlinear Programming: Theory and Algorithms*. John Wiley & Sons, New York.

Bouws, E., Günther, H., Rosenthal, W. and Vincent, C. (1985). Similarity of the wind wave spectrum in finite depth water – 1. Spectral form. *Journal of Geophysical Research*, 90(C1):975–986.

Box, M. (1966). A comparison of several current optimization methods, and the use of transformations in constrained problems. *Computer Journal*, 9:67–77.

Brigham, E. (1974). *The Fast Fourier Transform*. Prentice-Hall, Englewood Cliffs.

Burrus, C., Gopinath, R. and Guo, H. (1998). *Introduction to wavelets and wavelet transforms: A primer*. Prentice-Hall, New Jersey.

Chakrabarti, S. and Libby, A. (1988). Further verification of gaussian wave packets. *Applied Ocean Research*, 10(2):106–108.

Chui, C. (1992). *An Introduction to Wavelets*. Academic Press, San Diego.

Clauss, G. and Bergmann, J. (1986). Gaussian wave packets – A new approach to seakeeping tests of ocean structures. *Applied Ocean Research*, 10(2):190–206.

Clauss, G. and Kühnlein, W. (1995). A new approach to seakeeping tests of self-propelled models in oblique waves with transient wave packets. In *Proceedings of the 14th International Conference on Offshore Mechanics and Arctic Engineering*, Copenhagen, Denmark, Volume I - Part A, pp.

279–286. ASME, New York.

Clauss, G. and Kühnlein, W. (1997). Simulation of design storm wave conditions with tailored wave groups. In *Proceedings of the Seventh (1997) International Offshore and Polar Engineering Conference*, Honolulu, Hawaii, Volume III, pp. 228–237. ISOPE, Cupertino, California.

Clauss, G. and Steinhagen, U. (1999). Numerical simulation of nonlinear transient waves and its validation by laboratory data. In *Proceedings of the Ninth (1999) International Offshore and Polar Engineering Conference*, Brest, France, Volume III, pp. 368–375. ISOPE, Cupertino, California.

Clauss, G. and Steinhagen, U. (2000). Optimization of transient design waves in random sea. In *Proceedings of the Tenth (2000) International Offshore and Polar Engineering Conference*, Seattle, USA, Volume III, pp. 229–236. ISOPE, Cupertino, California.

Cointe, R., Geyer, P., King, B., Molin, B. and Tramoni, M. (1990). Nonlinear and linear motions of a rectangular barge in a perfect fluid. In *Proceedings of the 18th Symposium on Naval Hydrodynamics*, pp. 85–99.

Conte, S. and De Boor, C. (1980). *Elementary Numerical Analysis*. McGraw-Hill, New York, 3rd edition.

Daubechies, I. (1988). Orthonormal bases of compactly supported wavelets. *Communications on Pure and Applied Mathematics*, 41:909–996.

Daubechies, I. (1993). Orthonormal bases of compactly supported wavelets II, variations on a theme. *SIAM Journal of Mathematical Analysis*, 24(2):499–519.

Davis, M. and Zarnick, E. (1964). Testing ship models in transient waves. In Lunde, J. and Doroff, S. (Eds.), *Proceedings of the 5th Symposium on Naval Hydrodynamics*, Bergen, Norway, pp. 507–543. Office of Naval Research, Washington.

Dommermuth, D. and Yue, D. (1987). Numerical simulation of nonlinear axisymmetric flows with a free surface. *Journal of Fluid Mechanics*, 178:195–219.

Faulkner, D. and Buckley, W. (1997). Critical survival conditions for ship design. In *RINA International Conference: Design and Operation for Abnormal Conditions*, Glasgow, Scotland, pp. 1–41.

Fletcher, R. (1980). *Practical Methods of Optimization*. John Wiley & Sons, New York.

Funke, E. and Mansrad, E. (1982). The control of wave asymmetries in random waves. In *Proceedings of the 18th International Conference on*

Coastal Engineering, Cape Town, South Africa, pp. 725–744. ASCE, New York, 1983.

Goupillaud, P., Grossmann, A. and Morlet, J. (1984). Cycle-octave and related transforms in seismic signal analysis. *Geoexploration*, 23:85–102.

Han, S. (1975). Penalty Lagrangian methods in a quasi-newton approach. Report TR 75-252, Computer Science, Cornell University, Ithaca, New York.

Han, S. (1976). Superlinearly convergent variable metric algorithms for general nonlinear programming methods. *Mathematical Programming*, 11:263–282.

Hasselmann, K., Barnett, T., Bouws, E., Carlson, H., Cartwright, D., Enke, K., Ewing, J., Gienapp, H., Hasselmann, D., Kruseman, P., Meerburg, A., Müller, P., Olbers, D., Richter, K. and Sell, W. (1973). *Measurements of wind-wave growth and swell decay during the Joint North Sea Wave Project (JONSWAP).* Ergänzungsheft zur Deutschen Hydrographischen Zeitschrift A8(12), Deutsches Hydrographisches Institut, Hamburg.

Haver, S. and Andersen, O. (2000). Freak waves: Rare realizations of a typical population or typical realizations of a rare population? In *Proceedings of the Tenth (2000) International Offshore and Polar Engineering Conference*, Seattle, USA, Volume III, pp. 123–130. ISOPE, Cupertino, California.

Hua, J. and Ekman, P. (1999). A numerical study of high wave probability for some severe wave conditions. In *Proceedings of the Ninth (1999) International Offshore and Polar Engineering Conference*, Brest, France, Volume III, pp. 168–174. ISOPE, Cupertino, California.

Isaacson, M. and Foschi, R. (2000). On the selection of design wave conditions. *International Journal of Offshore and Polar Engineering*, 10(2):99–106.

Jenkins, G. and Watts, D. (1968). *Spectral Analysis and its Applications.* Holden-Day, San Francisco.

Kim, C., Clément, A. and Tanizawa, K. (1999). Recent research and development of numerical wave tanks – A review. *International Journal of Offshore and Polar Engineering*, 9(4):241–256.

Kriebel, D. and Alsina, M. (2000). Simulation of extreme waves in a background random sea. In *Proceedings of the Tenth (2000) International Offshore and Polar Engineering Conference*, Seattle, USA, Volume III, pp. 31–37. ISOPE, Cupertino, California.

Kühnlein, W. (1997). *Seegangsversuchstechnik mit transienter Systemanregung*. PhD thesis, Technische Universität Berlin, D 83.

Linfoot, B., Stansell, P. and Wolfram, J. (2000). On the characteristics of storm waves. In *Proceedings of the Tenth (2000) International Offshore and Polar Engineering Conference*, Seattle, USA, Volume III, pp. 74–83. ISOPE, Cupertino, California.

Longuet-Higgins, M. (1975). On the statistical distribution of the periods and amplitudes of sea waves. *Journal of Geophysical Research*, 80:2688–2694.

Longuet-Higgins, M. and Cokelet, E. (1976). The deformation of steep surface waves on water. I. A numerical method of computation. In *Royal Society of London*, Volume 350, pp. 1–25. Series A.

Louis, A., Maaß, P. and Rieder, A. (1998). *Wavelets: Theorie und Anwendungen*. B.G. Teubner, Stuttgart.

Mallat, S. (1989a). Multifrequency channel decomposition of images and wavelet models. *IEEE Transactions on Acoustics, Speech and Signal Processing*, 37:2091–2110.

Mallat, S. (1989b). Multiresolution approximation and wavelet orthonormal bases of l^2. *Transactions of the American Mathematical Society*, 315:69–87.

Mansard, E. and Funke, E. (1988). On the fitting of parametric models to measured wave spectra. In *Proceedings of the 2nd International Symposium on Wave Research and Coastal Engineering*, Hannover, pp. 363–385. Universität Hannover, SFB 205.

Meyer, Y. (1992). *Wavelets and Operators*. Cambridge University Press, Cambridge.

Nash, S. and Sofer, A. (1996). *Linear and Nonlinear Programming*. McGraw-Hill, New York.

Nelder, J. and Mead, R. (1965). A simplex method for function minimization. *Computer Journal*, 7:308–313.

Nickerson, J. (1993). Freak waves! *Mariners Weather Log*, 37:14–19.

Phillips, O. (1977). *Dynamics of the Upper Ocean*. Cambridge University Press, Cambridge.

Powell, M. (1978). A fast algorithm for nonlinearly constrained optimization calculations. In Watson, G. (Ed.), *Numerical Analysis*, Volume 630. Springer-Verlag, Berlin. Lecture Notes in Mathematics.

Read, W. and Sobey, R. (1987). Phase spectrum of surface gravity waves. *Journal of Waterway, Port, Coastal, and Ocean Engineering*, 113(5):507–

522.

Resnikoff, H. and Wells, R. (1998). *Wavelet analysis: The scalable structure of information*. Springer-Verlag, New York.

Rowan, T. (1990). *Functional Stability Analysis of Numerical Algorithms*. PhD thesis, University of Texas at Austin.

Schwarz, H. (1993). *Numerische Mathematik*. B.G. Teubner, Stuttgart.

Sheng, Y., Segur, H. and Lewellen, W. (1978). Application of a spatial smoothing scheme to control short-wave numerical oscillation. Technical report, A.R.A.P. Tech. Memo. No. 78-8, Aeronautical Research Associates of Princeton, New Jersey.

Sobey, R. (1999). "Real Sea States". Unpublished course notes, Advanced short course held at Leichtweiß-Institut für Wasserbau, TU Braunschweig.

Sobey, R. and Young, I. (1986). Hurricane wind waves – A discrete spectral model. *Journal of Waterway, Port, Coastal, and Ocean Engineering*, 112:370–389.

Stansberg, C. (1990). Extreme waves in laboratory generated irregular wave trains. In Tørum, A. and Gudmestad, O. (Eds.), *Proceedings of the NATO Advanced Research Workshop on Water Wave Kinematics*, Molde, Norway, pp. 573–589. Kluwer Academic Publishers, Dordrecht. NATO ASI Series, Series E - Volume 178.

Takezawa, S. and Hirayama, T. (1976). Advanced experimental techniques for testing ship models in transient water waves. Part II: The controlled transient water waves for using in ship motion tests. In Bishop, R., Parkinson, A. and Price, W. (Eds.), *Proceedings of the 11th Symposium on Naval Hydrodynamics: Unsteady Hydrodynamics of Marine Vehicles*, pp. 37–54. Department of Mechanical Engineering, University College London.

Takezawa, S. and Takekawa, M. (1976). Advanced experimental techniques for testing ship models in transient water waves. Part I: The transient test technique on ship motions in waves. In Bishop, R., Parkinson, A. and Price, W. (Eds.), *Proceedings of the 11th Symposium on Naval Hydrodynamics: Unsteady Hydrodynamics of Marine Vehicles*, pp. 23–35. Department of Mechanical Engineering, University College London.

Tanizawa, K. (1996). Long time fully nonlinear simulation of floating body motions with artificial damping zone. *Journal of the Society of Naval Architects of Japan*, 180:311–319.

Taylor, P. (1992). On the kinematics of large ocean waves. In *Proceedings of the Sixth International Conference on the Behaviour of Offshore Struc-*

tures, London, Volume 1, pp. 134–145. Elsevier Science, New York.

Taylor, P., Jonathan, P. and Harland, L. (1995). Time domain simulations of jack-up dynamics with the extremes of a gaussian process. In *Proceedings of the 14th International Conference on Offshore Mechanics and Arctic Engineering*, Copenhagen, Denmark, Volume I, pp. 313–319. ASME, New York.

Tromans, P., Anaturk, A. and Hagemeijer, P. (1991). A new model for the kinematics of large ocean waves – Application as a design wave. In *Proceedings of the First (1991) International Offshore and Polar Engineering Conference*, Edinburgh, U.K., Volume III, pp. 64–71. ISOPE, Cupertino, California.

Truckenbrodt, E. (1992). *Fluidmechanik*, Band 2: Elementare Strömungsvorgänge dichteveränderlicher Fluide sowie Potential- und Grenzschichtströmungen. Springer-Verlag, Berlin, Heidelberg, New York, 3rd edition.

Wilson, R. (1963). *A Simplicial Algorithm for Convex Programming*. PhD thesis, Harvard University, Graduate School of Business Administration.

Wolfram, J., Feld, G. and Allen, J. (1994). A new approach to estimating extreme environmental loading using joint probabilities. In *Proceedings of the Seventh International Conference on the Behaviour of Offshore Structures*, Cambridge (MA), USA, Volume 2, pp. 701–714. Elsevier Science, New York.

Wu, G.-X. and Eatock Taylor, R. (1994). Finite element analysis of two-dimensional non-linear transient water waves. *Applied Ocean Research*, 16(6):363–372.

Wu, G.-X. and Eatock Taylor, R. (1995). Time stepping solutions of two-dimensional non-linear wave radiation problem. *Ocean Engineering*, 22(8):785–798.

Zou, J. and Kim, C. (2000). Generation of strongly asymmetric wave in random sea. In *Proceedings of the Tenth (2000) International Offshore and Polar Engineering Conference*, Seattle, USA, Volume III, pp. 95–102. ISOPE, Cupertino, California.